Applied Research Laboratory
The Pennsylvania State University

AD-A187 671

A HYDRODYNAMIC ANALYSIS OF FLUID
FLOW BETWEEN MESHING SPUR GEAR TEETH

by

M. J. Wittbrodt and M. J. Pechersky

Contract N00024-85-C-6041

DTIC
ELECTE
NOV 1 9 1987
S D
H

TECHNICAL REPORT

The Pennsylvania State University
APPLIED RESEARCH LABORATORY
P.O. Box 30
State College, PA 16804

A HYDRODYNAMIC ANALYSIS OF FLUID FLOW BETWEEN MESHING SPUR GEAR TEETH

by

M. J. Wittbrodt and M. J. Pechersky

Contract N00024-85-C-6041

Technical Report No. TR 87-006
October 1987

Supported by:
Naval Sea Systems Command

L. R. Hettche, Director
Applied Research Laboratory

Approved for public release; distribution unlimited

DTIC
COPY
INSPECTED
6

Accession For
NTIS GRA&I ☑
DTIC TAB ☐
Unannounced ☐
Justification

By
Distribution/
Availability Codes
Dist | Avail and/or Special
A-1

Unclassified
SECURITY CLASSIFICATION OF THIS PAGE

AD-A182 621

REPORT DOCUMENTATION PAGE

REPORT SECURITY CLASSIFICATION Unclassified	1b. RESTRICTIVE MARKINGS
SECURITY CLASSIFICATION AUTHORITY	3. DISTRIBUTION / AVAILABILITY OF REPORT Unlimited
DECLASSIFICATION / DOWNGRADING SCHEDULE	
PERFORMING ORGANIZATION REPORT NUMBER(S) TR-87-006	5. MONITORING ORGANIZATION REPORT NUMBER(S)
NAME OF PERFORMING ORGANIZATION plied Research Laboratory e Pennsylvania State University ARL — 6b. OFFICE SYMBOL (If applicable)	7a. NAME OF MONITORING ORGANIZATION Naval Sea Systems Command Department of the Navy
ADDRESS (City, State, and ZIP Code) O. Box 30 ate College, PA 16804	7b. ADDRESS (City, State, and ZIP Code) Washington, DC 20362
NAME OF FUNDING / SPONSORING ORGANIZATION ıval Sea Systems Command — 8b. OFFICE SYMBOL (If applicable) NAVSEA	9. PROCUREMENT INSTRUMENT IDENTIFICATION NUMBER N00024-85-C-6041
ADDRESS (City, State, and ZIP Code) epartment of the Navy ıshington, DC 20362	10. SOURCE OF FUNDING NUMBERS PROGRAM ELEMENT NO. / PROJECT NO. / TASK NO. / WORK UNIT ACCESSION NO.

TITLE (Include Security Classification)
HYDRODYNAMIC ANALYSIS OF FLUID FLOW BETWEEN MESHING SPUR GEAR TEETH (Unclassified)

PERSONAL AUTHOR(S)
. J. Wittbrodt and M. J. Pechersky

TYPE OF REPORT	13b TIME COVERED	14. DATE OF REPORT (Year, Month, Day)	15. PAGE COUNT
MS thesis	FROM ____ TO ____	October 1987	114

SUPPLEMENTARY NOTATION

COSATI CODES			18. SUBJECT TERMS (Continue on reverse if necessary and identify by block number)
FIELD	GROUP	SUB-GROUP	Hydrodynamics, compressible flow, incompressible flow

ABSTRACT (Continue on reverse if necessary and identify by block number)

A one-dimensional analysis of the fluid pumping action resulting from the meshing of spur gears was performed by writing a computer algorithm. Two separate analyses were conducted; one using incompressible and the other using compressible flow theory. The incompressible flow calculations correspond to heavily lubricated gears whereas the compressible flow calculations are representative of lightly lubricated gears. The analysis demonstrated that the

0 DISTRIBUTION / AVAILABILITY OF ABSTRACT ☐ UNCLASSIFIED/UNLIMITED ☐ SAME AS RPT ☐ DTIC USERS	21. ABSTRACT SECURITY CLASSIFICATION Unclassified
2a NAME OF RESPONSIBLE INDIVIDUAL	22b. TELEPHONE (Include Area Code) 814/865-6344 — 22c. OFFICE SYMBOL

D FORM 1473, 84 MAR — 83 APR edition may be used until exhausted. All other editions are obsolete.

SECURITY CLASSIFICATION OF THIS PAGE
Unclassified

velocity of the discharged fluid reached high velocities for both cases. The high meshing rate of the teeth along with the small discharge area is the cause for the high fluid velocities. Certain geometric design variables of the gears were seen to affect the peak velocities for each case. The variables most significantly affecting the peak velocity appear to be the drive ratio and the face width. The high velocities may contribute to the noise generated during meshing of gear teeth due to the jet noise as a result of the high velocity jets impinging on the enclosures surrounding the gears and the formation of shock waves at the exit plane of the teeth.

ABSTRACT

A one-dimensional analysis of the fluid pumping action resulting from the meshing of spur gears was performed by writing a computer algorithm. Two separate analyses were conducted; one using incompressible and the other using compressible flow theory. The incompressible flow calculations correspond to heavily lubricated gears whereas the compressible flow calculations are representative of lightly lubricated gears. The analysis demonstrated that the velocity of the discharged fluid reached high velocities for both cases. The high meshing rate of the teeth along with the small discharge area is the cause for the high fluid velocities. Certain geometric design variables of the gears were seen to affect the peak velocities for each case. The variables most significantly affecting the peak velocity appear to be the drive ratio and the face width. The high velocities may contribute to the noise generated during meshing of gear teeth due to the jet noise as a result of the high velocity jets impinging on the enclosures surrounding the gears and the formation of shock waves at the exit plane of the teeth.

TABLE OF CONTENTS

	Page
ABSTRACT	iii
LIST OF TABLES	vi
LIST OF FIGURES	vii
NOMENCLATURE	x
ACKNOWLEDGEMENTS	xii

Chapter

1	INTRODUCTION	1
2	INCOMPRESSIBLE FLOW THEORY	10
	2.1. Introduction	10
	2.2. Velocity Equation	10
	2.2.1. Control Volume	10
	2.2.2. Continuity	11
	2.3. Geometric Parameters	13
	2.3.1. Discharge Area	13
	2.3.2. Volume	18
3	COMPRESSIBLE FLOW THEORY	48
	3.1. Introduction	48
	3.2. Velocity Equation	48
	3.2.1. Energy Equation	49
	3.2.2. Pressure Equation	50
4	RESULTS AND DISCUSSION	53
	4.1. Introduction	53
	4.2. Incompressible Flow	58
	4.3. Compressible Flow	68

TABLE OF CONTENTS (continued)

Page

4 RESULTS AND DISCUSSION (continued)

4.4. Comparison of Incompressible and Compressible Flow .. 83

4.5. Conclusions 89

BIBLIOGRAPHY 93

APPENDIX: COMPUTER ALGORITHM GUIDE AND A FLOW CHART 95

LIST OF TABLES

Table		Page
1.	Incompressible Parameter Variations to Assess the Effects on Velocity	54
2.	Compressible Parameter Variations to Assess the Effects on Velocity	55
3.	Geometry Variations for Comparison of Incompressible and Compressible Flow Velocity	57

LIST OF FIGURES

Figure		Page
1.1	Air and Lubricant Flow.	2
1.2	Generation of an Involute.	5
1.3	Spur Gear Teeth Terminology.	6
1.4	Arc of Approach and Recession.	8
2.1	Control Volume.	12
2.2	Driving Gear Tooth Geometry.	14
2.3	Flow Paths for Discharged Fluid.	15
2.4	Chord Between the Teeth.	17
2.5	2-D Plane Area.	19
2.6	Area of a Pinion Tooth.	20
2.7	Determining Integral Sets.	22
2.8	Involute Profiles.	23
2.9	Comparison of the actual radius profile to the approximate profile.	25
2.10	Addendum of the Pinion.	26
2.11	Local and Global Angles.	28
2.12	Integral Set 1.	29
2.13	Integral Set 2.	31
2.14	Integral Set 3.	34
2.15	Integral Set 4.	38
2.16	Integral Set 5.	41
2.17	Integral Set 6.	43
2.18	Excluded Area.	46

LIST OF FIGURES (continued)

Figure		Page
3.1	Converging Nozzle.	52
4.1	Dimensionless velocity for the three flow areas.	59
4.2	Dimensionless velocity as a function of backlash changes.	61
4.3	Incompressible velocity vs. pitch line velocity.	62
4.4	The effect of diametral pitch changes on velocity.	63
4.5	The effect of drive ratio changes on the velocity.	65
4.6	Velocity changes due to pressure angle variation.	66
4.7	Velocity as a function of flow distribution factor, f.	67
4.8	Dimensionless velocity for the three areas.	69
4.9	Peak velocity for backlash variation.	70
4.10	Position Mach 1 is reached for backlash changes.	71
4.11	Subsonic velocity due to backlash changes.	72
4.12	Subsonic velocity for pitch line changes.	74
4.13	Sonic velocity for pitch line changes.	75
4.14	Mesh position at which Mach 1 is reached for pitch line changes.	76
4.15	Dimensionless pressure for pitch line changes.	77
4.16	Peak velocity due to drive ratio changes.	78
4.17	Position at which Mach 1 is reached for drive ratio changes.	79
4.18	The effect diametral pitch has on peak velocity.	80
4.19	The position at which Mach 1 is reached for diametral pitch changes.	81
4.20	Subsonic velocity for diametral pitch changes.	82
4.21	Velocity for pressure angle variation.	84

LIST OF FIGURES (continued)

Figure Page

4.22 Dimensionless pressure in the mesh region for the three flow areas. 85

4.23 The effect of flow distribution variation on peak velocity. 86

4.24 Temperature in Fahrenheit in the mesh region for the three flow areas. 87

4.25 Comparison of incompressible and compressible end flow. 88

4.26 Comparison of incompressible and compressible teeth flow. 91

4.27 Comparison of incompressible and compressible combined flow. . 92

NOMENCLATURE

A	=Discharge Area in^2
$chord2$	= chord length for discharge area in inches
c_p	= specific heat at constant pressure $ft\ lb_f/lb_m R$
c_v	= specific heat at constant volume $ft\ ib_f/lb_m R$
E_p	= angle from start of involute to addendum in radians
g_c	= dimensional constant 386 $lb_m\ in/lb_f\ sec^2$
h	= enthalpy $ft\ lb_f/lb_m$
k	= ratio of specific heats, c_p/c_v
P_e	= Pressure at exit plane in lb_f/in^2
P_i	= Pressure inside of control volume in lb_f/in^2
P_∞	= Pressure of the ambient in lb_f/in^2
r_{ag}	= radius at addendum circle of gear in inches
r_{ap}	= radius at addendum circle of pinion in inches
r_{bg}	= radius at base circle of gear in inches
r_{bp}	= radius at base circle of pinion in inches
r_{dg}	= radius at dedendum circle of gear in inches
r_{dp}	= radius at dedendum circle of pinion in inches
r_{inv1}	= involute profile leading edge in inches
r_{inv2}	= involute profile trailing edge in inches
r_{pg}	= radius at pitch circle of gear in inches
r_{pin}	= radius to addendum of pinion in inches
r_{pp}	= radius at pitch circle of pinion in inches
t_{ag}	= thickness of tooth at addendum of gear in inches
t_{ap}	= thickness of tooth at addendum of pinion in inches

NOMENCLATURE (continued)

T_e	= Temperature at exit plane in R
T_i	= Temperature inside of control volume in R
T_∞	= Temperature of the ambient in R
tr_{bg}	= thickness of gear at base in radians
tr_{pg}	= thickness of pinion at base in radians
V	= volume in^3
v_{comp}	= velocity from compressible flow theory
$\tilde{v}_{comp}$	= dimensionless compressible velocity
v_{inc}	= velocity determined from incompressible theory
$\tilde{v}_{inc}$	= dimensionless incompressible velocity
X	= angle to leading edge of involute in radians
ω	= angular velocity in radians/sec
ρ_i	= density of air inside control volume lb_m/in^3
ρ_e	= density at exit plane lb_m/in^3
ρ_∞	= density at infinity lb_m/in^3

ACKNOWLEDGEMENTS

I wish to express my sincere gratitude to my advisor, Professor Martin J. Pechersky. His guidance and support during this investigation and career advice have been very helpful. Thanks to Mr. John H. Ostar and Dr. Shirish N. Kher for developing the plotting routine for the results. A special thanks is given to Professor Richard A. Queeney for providing work space in his office. I also wish to express appreciation to my parents for the support and encouragement they gave me throughout my studies.

Appreciation is given to the Naval Sea Systems Command and the Applied Research Laboratory Exploratory and Foundational Research Program for the financial support of this project.

Chapter 1

INTRODUCTION

Smooth, quiet running gears are desirable in many applications. Much has been done to identify possible sources of noise in gears. It is recognized that the gear meshing action is one of the most important sources of noise in high speed machinery. Meshing noise is generated by the nonuniform transfer of torque between gears due to geometric defects in tooth profiles, gear shaft vibrations, and bending of the teeth under load [1]. A considerable amount of work has been done and is currently in progress to predict and lower the effects of these sources. Ishida and Matsuda [2] studied the effect of friction noise on gears by examining pitch circle impulse noise simulated by two disks. The same authors also studied gear noise due to surface roughness [3]. Fukama et al.[4] analyzed noise mechanisms of axial and radial vibration in spur gears. Badgley [5] computed the flow of vibration energy within a gear drive train as a method to understand the noise problem and the technology needed to alleviate it. Laskin [6] showed a procedure to predict gear noise by computing the mechanical energy from the sinusoidal displacement and dynamic tooth force and then determined the fraction of energy radiated in the form of acoustic energy. These studies have focused primarily on the physical contact between the meshing gears as a source of noise. One possible source of noise, which has not been thoroughly analyzed, is the flow of air and lubricant from between meshing gear teeth. During a high speed mesh, the time duration of the arc of approach and recession can take on the order of 100 microseconds. During this cycle, the air and lubricant is compressed and pumped out at high speeds between the teeth and the ends. See Figure 1.1. The result of the pumping action is noise and possibly thermal failures. If the

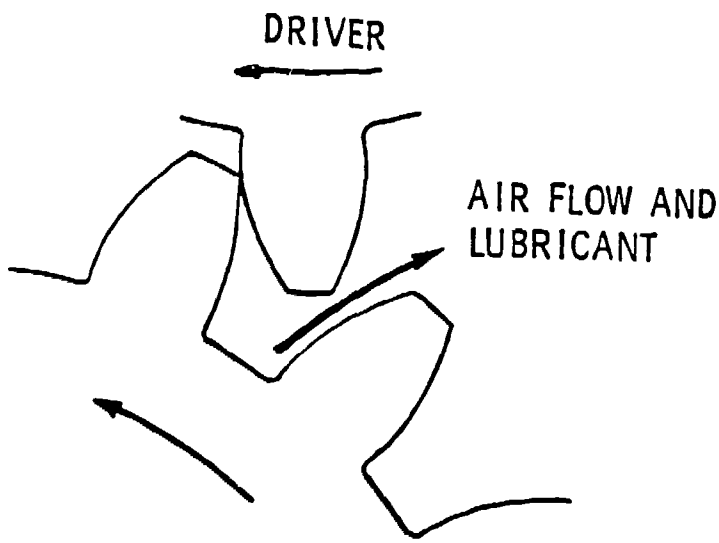

Figure 1.1 Air and Lubricant Flow. Air and lubricant are compressed and pumped out from between the teeth

air velocity between the teeth should reach sonic levels, a shock wave can form which emanates noise. Drago [1] mentions this problem for high speed gears with very wide face-widths. Rosen [7] presented air flow noise as part of an overall examination of gear noise sources. In his report, he computed the velocity of air flow in spur gears using incompressible flow theory. By drawing curves of the meshing volume and discharge area with respect to mesh position, he generated a graphical representation of the velocity, $v = \frac{dV/dt}{A}$, where A is the discharge area and dV/dt is the time rate of volume change. His analytical results indicate the air velocity approaches sonic levels for a particular gear operating at 20,000 RPM and this corresponded to the experimental result of a sudden rise in noise. Dudley recognized the thermal complications associated with fluid being expelled between meshing teeth. He attributes overheating failures of gear box and gear teeth to high-speed air flow between teeth. For high-speed gears, the gear teeth act like blades on a centrifugal compressor which heat up due to the friction with the surrounding air. Further heating is caused by the pumping air each time a gear meshes. Typical thermal failures are softening of teeth, scoring or pitting due to oil-film breakdown on overheated teeth, local overloading of teeth due to thermal distortion of tooth-contact pattern, misalignment of gears and bearings from distortion of the casing, and failure of bearings due to overheating. To prevent problems of this nature, Dudley recommends not using spur and straight bevel teeth when the pitch line velocity exceeds 10,000 fpm, because they do the poorest job of expelling air efficiently. As a guide to designers, he also lists typical axial meshing velocities for helical gears and the corresponding severity of thermal problems resulting from air flow [8]. Buckingham [9] notes that excessive oil at the tooth mesh creates heating problems from the high discharge rate of oil at the mesh. Smith mentions that noise can occur if oil is trapped in the roots of meshing spur gear teeth of high face width. If oil cannot escape through

the ends of the teeth, high pressure develops and it forces the gears apart. The pressurized oil shoots outward against the gear casing resulting in vibrations [10].

The purpose of this thesis was to assess the magnitude of the fluid velocity that results from meshing spur gear teeth and to determine whether it reaches levels capable of causing noise. The fluid velocity was analyzed by assuming one-dimensional flow and applying incompressible and compressible flow theories. It is expected that this work will form the basis for future experimental and theoretical analysis of the fluid pumping problem. Eventually, this work should lead to a better understanding of the hydrodynamics associated with the meshing action and permit the prediction of conditions causing noise and tooth failures. Predictive knowledge can aid designers in making more quantified decisions on choice of geometry and pitch line velocity.

A brief description of the tooth geometry, the meshing action, air flow induced noise, and formation of a shock wave is given. For gears to run smoothly and transmit power effectively, the ratio of the angular velocity of the driving gear compared to the driven must remain constant. The law of gearing states that the lines of action at every point of contact must pass through the pitch point. The involute profile is used as a tooth profile because its shape satisfies these requirements [11]. The involute profile is generated by unwinding a string from the circumference of a circle. See Figure 1.2. Definitions for the parts of a gear tooth are shown in Figure 1.3. The diametral pitch is the number of teeth on a gear per inch of pitch diameter. The pitch circle diameter is defined by the number of teeth divided by the diametral pitch. The addendum is the radial distance from the pitch circle to the top of the gears. The dedendum is the radial distance from the pitch circle to the bottom land. The base circle is the point where the involute profile begins.

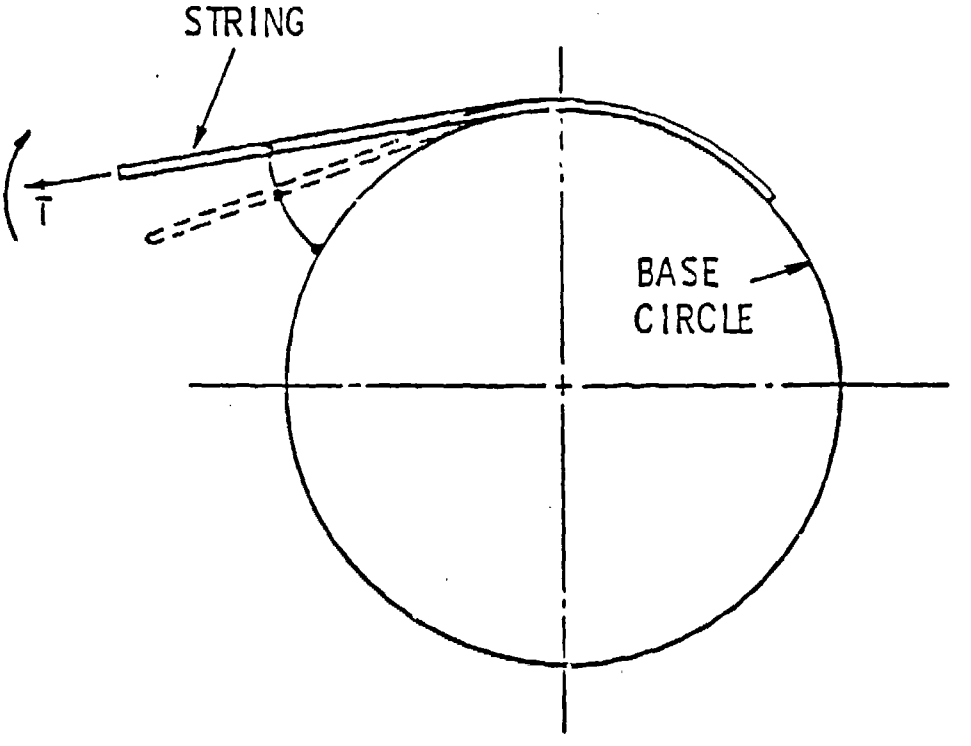

Figure 1.2 Generation of an Involute. The involute profile is generated by unwinding a taut string from the circumference of a circle.

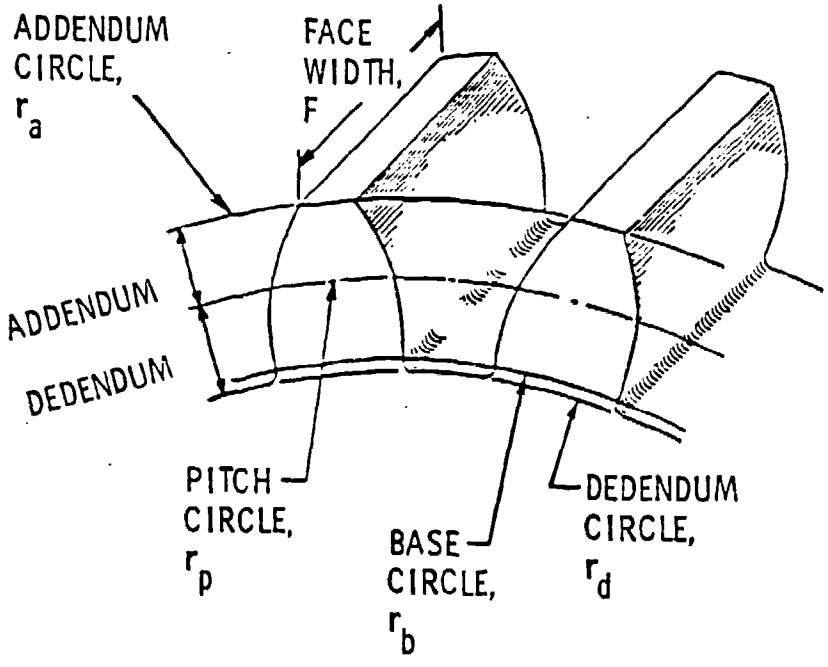

Figure 1.3 Spur Gear Teeth Terminology.

The meshing action (Figure 1.4) is split into two parts; the approach and the recession. The arc of approach begins with the initial contact of the driving gear, T_1 at the tooth tip of the driven, T_2 (solid lines). The contact slides up to the pitch point where the approach ends (dashed lines). The arc of recession begins at the pitch point (solid lines) and ends when the tip of the driving gear loses contact with the driven gear (dashed lines). All of the contact points fall along the pressure line.

Air flow noise results from three sources: monopole, dipole, and quadrupole. A monopole source occurs when air is interrupted at a regular rate. An example is a siren. A dipole source is one in which a moving stream strikes a solid object and a quadrupole source is a result of a gas jet. An example of dipole noise is the aerodynamic noise generated by fan blades moving through air. Quadrupole sources of noise arise from a gas jet [12]. Gas jet noise is distributed downstream from the nozzle with high frequencies near the nozzle and lower frequencies downstream. When the critical pressure for a gas jet is reached, the jet is choked and a shock formation occurs which is an additional source of noise [13]. The motion of high speed gears probably gives rise to dipole and quadrupole sources of noise. The dipole source is a result of the gear teeth acting as blades moving through air and the quadrupole source is due to the jet stream of air exhausted from between meshing teeth. Calculations in this thesis have shown that for particular geometries and pitch line velocities, the jet velocities can reach sonic levels.

Shock waves represent rapid changes in the velocity and pressure of the flow and are modeled as a discontinuity [14]. Shocks are formed when compression waves become steeper and form a discontinuity. In the particular case of meshing gears, when the pressure in the mesh region increases enough for the pressure ratio, pressure inside divided by ambient, to reach the critical ratio the jet

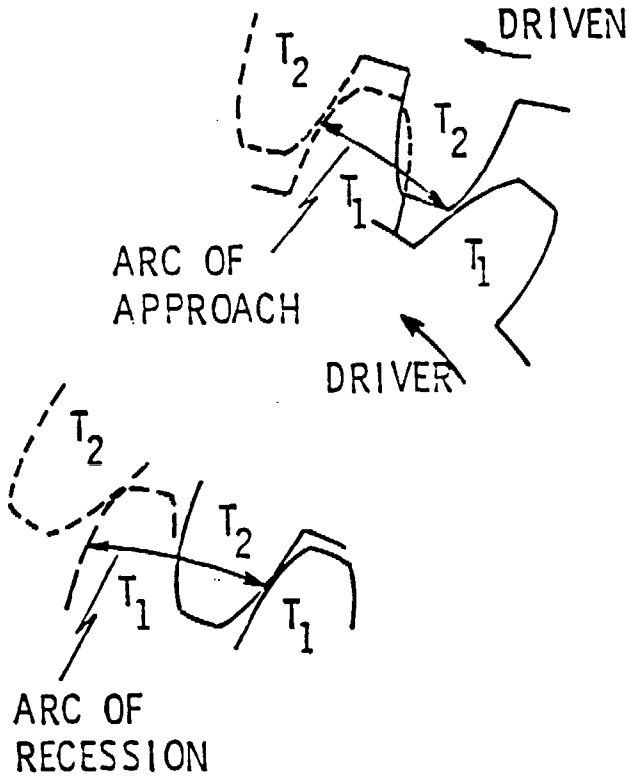

Figure 1.4 Arc of Approach and Recession. The arc of approach and recession are shown for the driving tooth, T_1, and the driven tooth, T_2. The solid lines indicate the beginning of the arc and the dashed lines the end of the arc.

becomes choked. The flow expands downstream from the nozzle at supersonic velocity and a shock is formed outside the nozzle.

Chapter 2 examines incompressible flow for the meshing spur gear teeth in a stationary rack and gear using a one-dimensional flow model. This model is most appropriate for heavily lubricated gears in which the composition of the fluid trapped between the gear teeth is the lubrication oil. The assumption of an ideal fluid allows the fluid to be considered frictionless and incompressible. The equation for incompressible velocity is derived by applying the continuity equation to a control volume. The remainder of the chapter explains the evaluation of the fluid discharge area and the volume.

A representation of the flow problem for air is presented in Chapter 3 which accounts for the changes in density. This model assumes the gears are lightly lubricated with the primary discharged fluid being air. Using this assumption, the velocity was found to be comparable in magnitude with the local speed of sound. The compressible velocity equation was developed using the First Law of Thermodynamics in addition to the continuity equation.

The hydrodynamic action of the meshing gear teeth was simulated by a computer algorithm. These calculations gave information about the following: fluid velocity at the exit plane and the temperature, density, and pressure in the tooth space. The results and discussion are given in Chapter 4. An explanation of the computer algorithm and a block diagram is presented in the appendix.

Chapter 2

INCCMPRESSIBLE FLOW THEORY

2.1. Introduction

The expressions which describe the time dependent velocity were developed based on a one-dimensional model in which the fluid was assumed to be frictionless and incompressible. Thus, only the continuity equation and expressions for the relevant geometric parameters are required. The model is based on a control volume defined by the surfaces of the gear teeth and the flow area at the ends of the gears and the flow area defined by the tip of the engaging tooth and the face of the corresponding tooth on the driven gear. The analysis began at the angle of approach when contact first occurs. This approach assumed no flow occurred before contact. This derivation is appropriate for a stationary rack and gear and also for a stationary ring and gear. However, for two rotating spur gears an additional tangential velocity term for the angular rotation of the control volume should be accounted for by the vector, $r\omega$, where r is the pitch radius and ω is the angular velocity.

2.2. Velocity Equation

The velocity equation was derived by first obtaining expressions for the control volume geometry and then applying the continuity equation to solve for the fluid velocity.

2.2.1. Control Volume

As the driving gear tooth contacts a pinion tooth, a control volume is formed. For the calculations, the driven gear was considered the pinion and the driver the gear. The control surface is described by the boundaries of the involute profiles of two adjacent pinion teeth, their bottom land, and the profile of the meshing

gear tooth and the discharge exit area. See Figure 2.1. Note that the control volume has a variable geometry. The main effort in solving for the velocity was to obtain an expression for the volume and flow area as a function of the relative angular position of the meshing gear and pinion teeth.

2.2.2. Continuity

The integral form of the continuity equation states that the time rate of increase of mass in the control volume is equal to the net rate of mass inflow or outflow to the control volume.

$$\frac{\partial}{\partial t}\int_V \rho\, dV = -\int_S \rho \vec{v}_r \cdot \vec{n}\, dS, \tag{2.1}$$

where ρ is the density, V is the volume, $\vec{v}_r$ is the velocity relative to the exit plane of the control volume, S is the surface area, and $\vec{n}$ is a unit vector normal to the surface. Assuming one-dimensional flow, an incompressible fluid of constant density, ρ, and flow through a discharge area, A, gives

$$\rho\frac{dV}{dt} = \rho v_r \int_A dA. \tag{2.2}$$

Canceling ρ and evaluating the integral gives

$$\frac{dV}{dt} = v_r A. \tag{2.3}$$

Solving for the relative velocity gives

$$v_r = \frac{1}{A}\frac{dV}{dt}. \tag{2.4}$$

Using the chain rule gives

$$v_r = \frac{1}{A}\frac{dV}{d\theta}\frac{d\theta}{dt}, \tag{2.5}$$

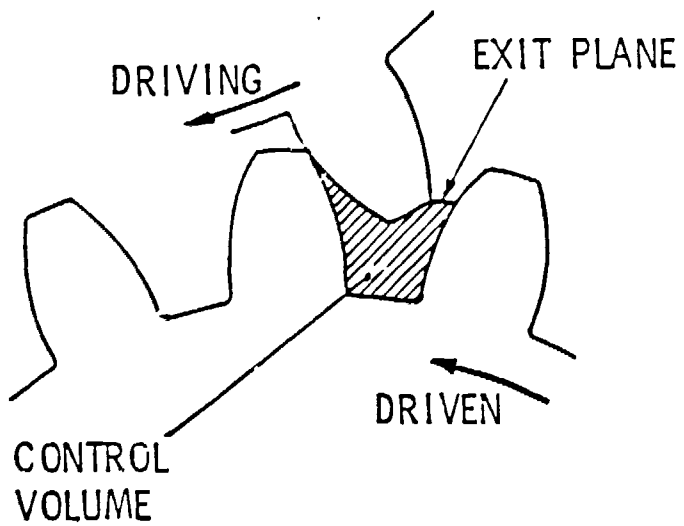

Figure 2.1 Control Volume. A control volume is formed as the driving tooth contacts the driven tooth.

where $dV/d\theta$ is the change in volume with respect to position and $d\theta/dt$ is the time rate of change in position. Defining the angular velocity of the gear, $\omega = d\theta/dt$, and substituting into equation 2.5 results in

$$v_r = \frac{1}{A}\frac{dV}{d\theta}\omega. \tag{2.6}$$

Dividing both sides by the pitch line velocity, $\omega \times r_{pitch}$, gives

$$\tilde{v}_r = \frac{v_r}{\omega \times r_{pitch}} = \frac{1}{A \times r_{pitch}}\frac{dV}{d\theta}. \tag{2.7}$$

This represents the dimensionless velocity escaping through a discharge area, A.

2.3. Geometric Parameters

The two geometric parameters, A and $dV/d\theta$, depend on the geometry of the gears and the position in the mesh cycle. The discharge area, A, was chosen to have three possible values depending on the path of air flow: area between teeth, end flow area, and combined flow area. The rate of volume change, $dV/d\theta$, was calculated using a numerical derivative of equation 2.10. The values for the volume as a function of θ were determined from a 2-D plane area which was then multiplied by the face width to give a volume. Figure 2.2 summarizes the variables of the gear geometry used to calculate the discharge area and volume.

2.3.1. Discharge Area

Air escapes from the meshing region by two paths. One path is the direct discharge between the meshing teeth. The other is flow out the ends of the gear. See Figure 2.3. The amount of flow through either path depends on the tooth height and the face width of the gear. In the case of wide gears, the discharge area between the teeth dominates flow. When the face width is narrow, end flow dominates. A combination flow results for intermediate face width gears.

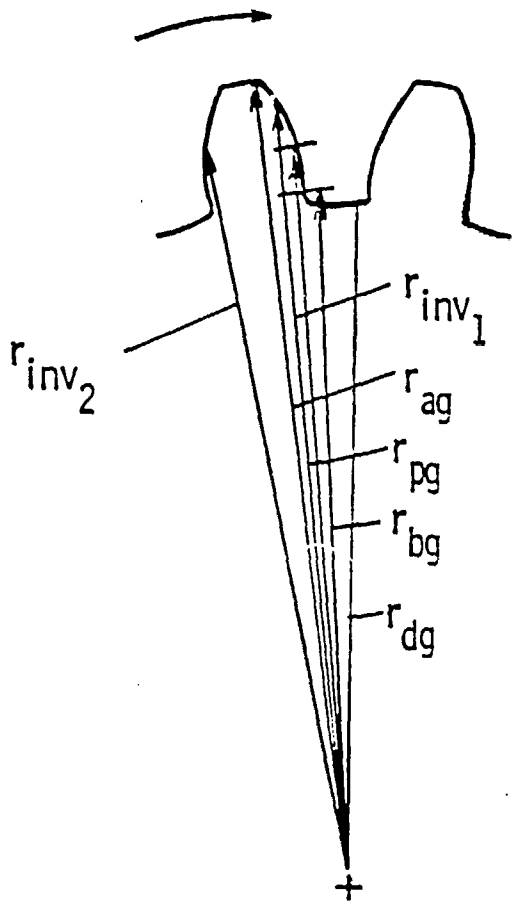

Figure 2.2 Driving Gear Tooth Geometry.

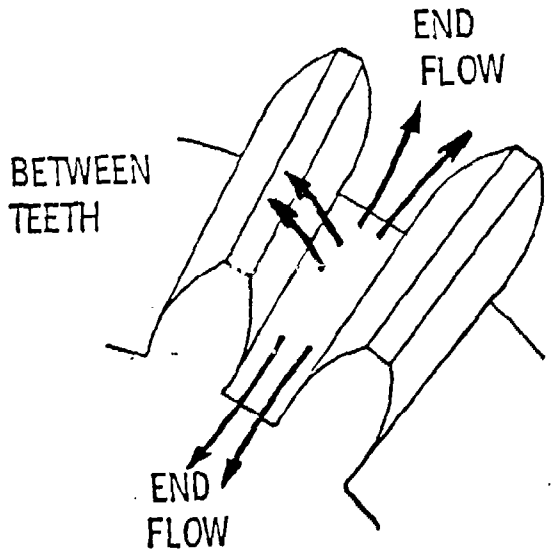

Figure 2.3 Flow Paths for Discharged Fluid. Air escapes either through the ends or between the the teeth.

To determine the area for discharge between the meshing teeth, the shortest chord distance between the meshing teeth is calculated and the backlash amount is added to the chord length. During the approach, $chord2$ is defined as the distance between the involute surface of the upper pinion tooth and the near part of the tip of the engaging gear tooth (trailing edge involute, r_{inv2}). See Figure 2.4. Thus, the area between the teeth for flow is $(backlash + chord2) \times face\ width$. This is not precisely true near the end of the mesh cycle because the involute portion of the tooth is closer to the meshing tooth than the tip, but at that time in the mesh the chord is closed off and the distance is reasonably represented by the backlash amount. The backlash is the amount the teeth are cut thinner than the theoretical dimensions. The backlash accommodates any expansion of the teeth due to temperature effects.

The end flow area for one end equals the control volume divided by the face width. The total end flow area is twice the single end area and is given by

$$total\ end\ area = 2 \times (volume/\ face\ width). \tag{2.8}$$

The combined area was chosen to be the sum of the area between the meshing teeth and the end flow with a factor related to the tooth height and face width. The combined area is given by

$$combined\ area = between\ teeth\ + \left(end\ area \times f\right)\left(\frac{tooth\ height}{face\ width}\right)^2, \tag{2.9}$$

where f is the percentage of end area used. This equation was chosen as a possible representation of the distribution. It is based on the idea that the fluid will tend to seek the shortest path of least resistance. Using the ratio of the tooth height to the face width resembles the length of path the fluid may travel.

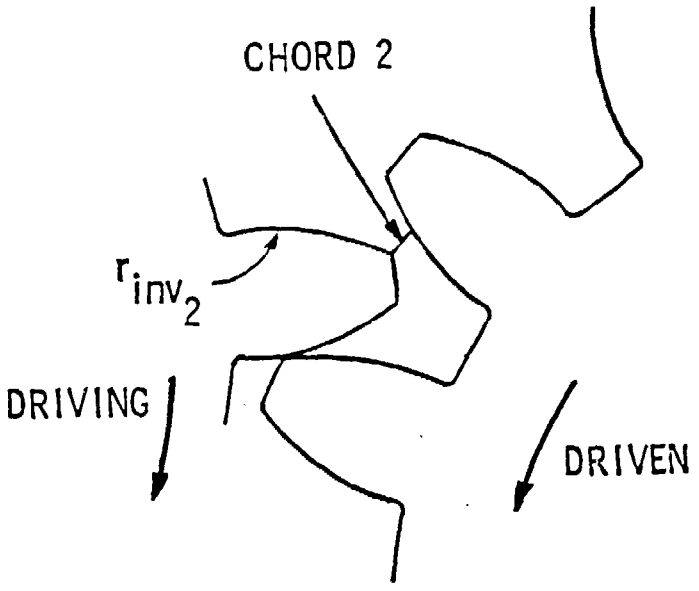

Figure 2.4 Chord Between the Teeth. The shortest chord length between the teeth was used to calculate the discharge area between the teeth.

2.3.2. Volume

The rate of volume change with respect to position, θ, was calculated by taking a numerical derivative of equation 2.10. The volume was described previously as being bounded by two pinion teeth and the meshing gear tooth. The volume was calculated by multiplying the two-dimensional plane area, Figure 2.5, by the constant face width of the gear.

$$volume = (2-D\ plane_{area}) \times face\ width. \tag{2.10}$$

The $2-D\ plane_{area}$ is the sum of the area between two pinion teeth, B_{area}, minus the area overlapped by the meshing gear tooth, $overlap_{area}$, and minus the section no longer part of the control volume, $excluded_{area}$. A description follows for each component of the $2-D\ area$.

$$2-D\ plane_{area} = B_{area} - overlap_{area} - excluded_{area}. \tag{2.11}$$

The area between two pinion teeth is

$$B_{area} = \frac{\pi\,(r_{ap})^2 - \pi\,(r_{dp})^2 - N \times tooth_{area}}{N}, \tag{2.12}$$

where N is the number of teeth and the area of a pinion tooth is given by equation 2.13. Figure 2.6 gives a description of the limits for the tooth area calculation.

$$\begin{aligned} tooth_{area} = & \int_0^{tr_{bp}} \int_{r_{bp}}^{r_{ap}} r\,dr\,d\phi \quad + \int_0^{tr_{bp}} \int_{r_{dp}}^{r_{bp}} r\,dr\,d\phi \\ & - 2\int_0^{E_p} \int_{r_{inv}}^{r_{ap}} r\,dr\,d\phi, \end{aligned} \tag{2.13}$$

where tr_{bg} is the thickness in radians of the tooth at the base circle of the pinion, r_{inv} is an approximation for an involute radius, and E_p represents the

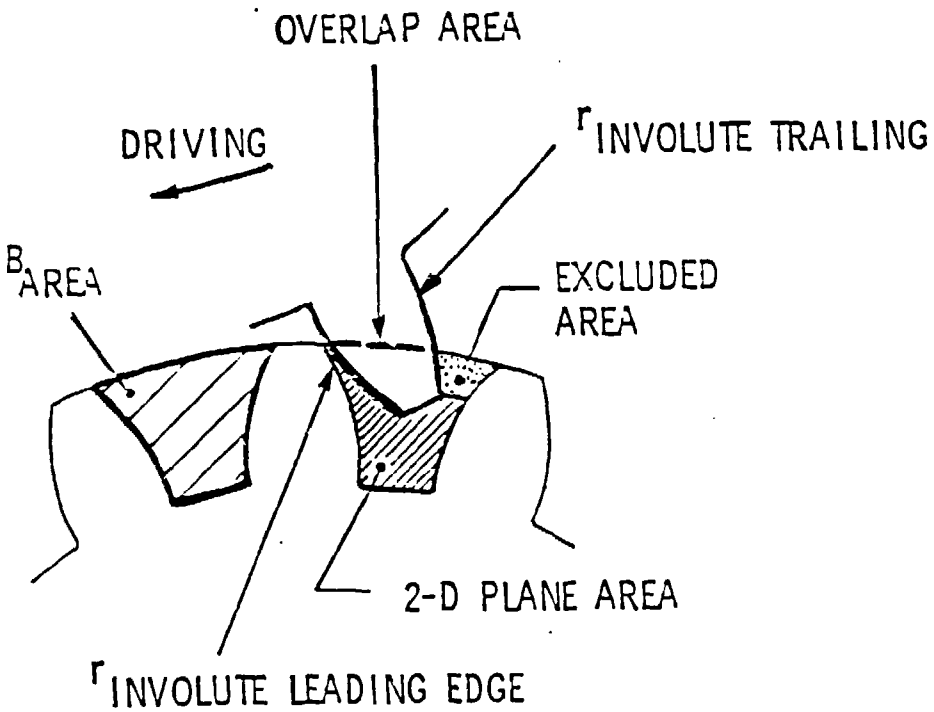

Figure 2.5 2-D Plane area. The volume was determined by multiplying the 2-D plane area by the gear face width.

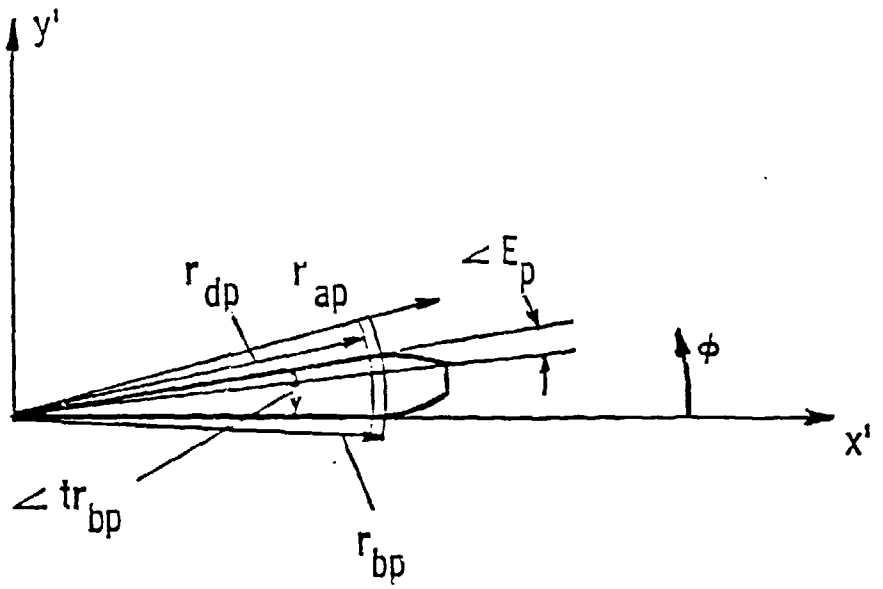

Figure 2.6 Area of a Pinion Tooth. Description of angles and radii used to calculate the area of a pinion tooth.

arc in radians from the beginning of the tooth profile at the base circle to the tooth tip [9].

$$E_p = \frac{\sqrt{r_{ap}^2 - r_{bp}^2}}{r_{bp}} - arctan(\frac{\sqrt{r_{ap}^2 - r_{bp}^2}}{r_{bp}}). \tag{2.14}$$

Evaluating the integrals for $tooth_{area}$ gives

$$\begin{aligned} tooth_{area} = & \frac{1}{2}(r_{ap}^2 - r_{bp}^2)tr_{bp} + \frac{1}{2}(r_{bp}^2 - r_{dp}^2)tr_{bp} \\ & - [r_{ap}^2 E_p - r_{bp}^2(\frac{3}{5} \times E_p + 3^{2/3} \times E_p^{5/3} \\ & + \frac{3}{28} \times 3^{4/3} \times E_p^{7/3})]. \end{aligned} \tag{2.15}$$

The area overlapped by the meshing gear tooth, $overlap_{area}$, is approximated by integrating the area of the gear tooth profile inside the addendum of the pinion. The integrals used depended on the location of the driving gear tooth centerline with respect to the x-axis and whether or not the base circle radius of the gear overlapped the addendum circle of the pinion. See Figure 2.7. If the base circle radius overlapped the pinion addendum during the mesh, four sets of integrals resulted: Sets 1 through 4. In the case of the base circle of the gear not overlapping the addendum circle of the pinion, only two sets of integrals resulted: Sets 5 and 6. For the calculation of $overlap_{area}$, approximations for the involute profile of the gear and the equation of the pinion addendum circle were developed.

The involute profiles for the driving gear tooth are the leading side r_{inv1}, and the trailing side, r_{inv2} see Figure 2.8. The profiles were approximated as

$$r_{inv1} = r_{bg}(1 + \frac{1}{2}(3\phi)^{2/3}) \tag{2.16}$$

and

$$r_{inv2} = r_{bg}(1 + \frac{1}{2}(3(tr_{bg} - \phi))^{2/3}. \tag{2.17}$$

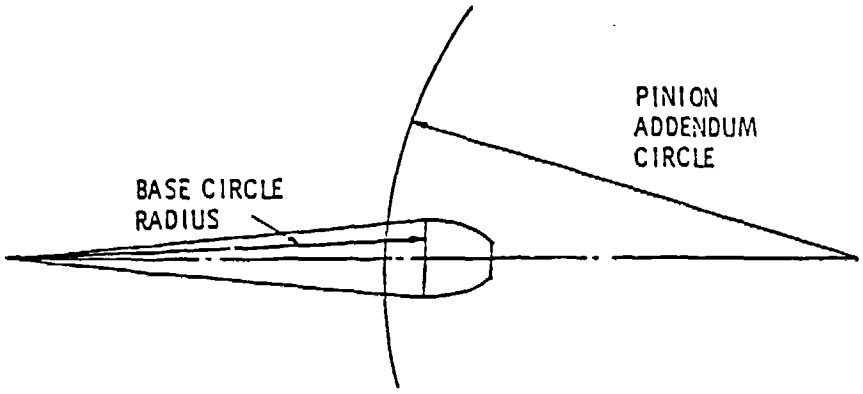

Base circle overlaps addendum. When the base circle of the gear falls inside the addendum of the pinion, four sets of area integrals are required.

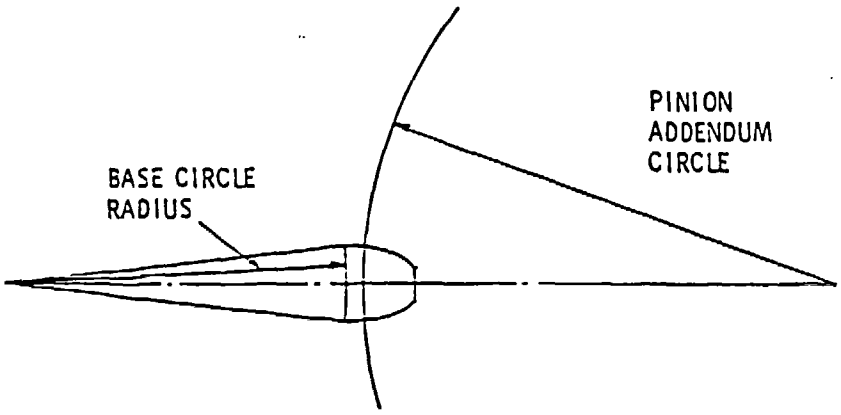

Base circle outside of addendum. When the base circle of the gear remains outside of the pinion addendum, two sets of area integrals are required.

Figure 2.7 Determining Integral Sets.

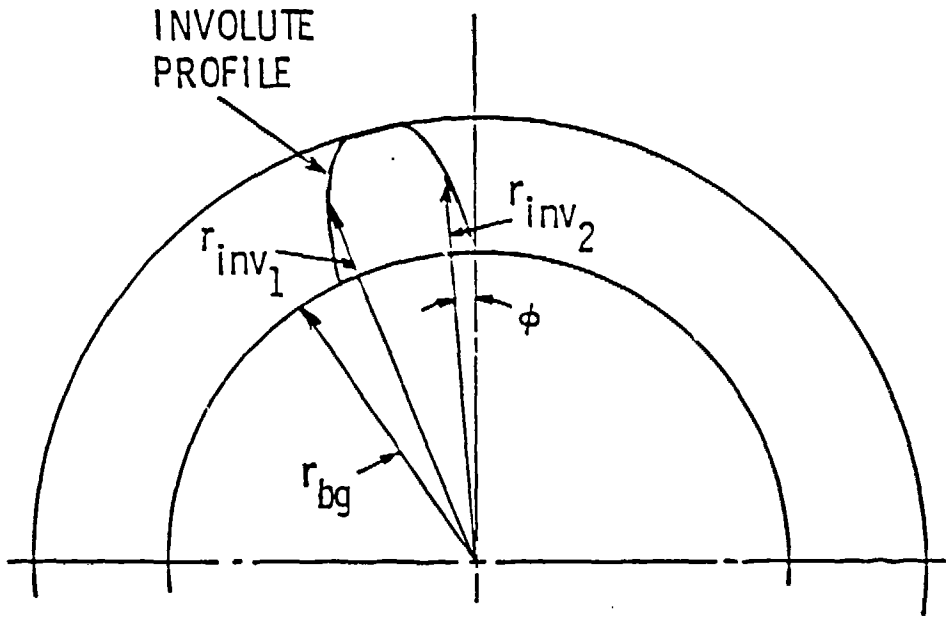

Figure 2.8 Involute Profiles. The involute profile approximations, r_{inv1} and r_{inv2}, and angle ϕ.

The approximations were developed using Buckingham's [9] vector representation of ϕ. See Figure 2.8.

$$\phi = \frac{\sqrt{r_{inv1}^2 - r_{bg}^2}}{r_{bg}} - \arctan \frac{\sqrt{r_{inv1}^2 - r_{bg}^2}}{r_{bg}}. \tag{2.18}$$

Defining $\tilde{r}^2 = r_{inv1}^2 / r_{bg}^2$ gives

$$\phi = \sqrt{\tilde{r}^2 - 1} - \arctan \sqrt{\tilde{r}^2 - 1}. \tag{2.19}$$

Expressing $\arctan \sqrt{\tilde{r}^2 - 1}$ as an infinite series and eliminating higher order terms gives

$$\phi = \frac{1}{3}\left(\sqrt{\tilde{r}^2 - 1}\right)^3 \tag{2.20}$$

and solving for r_{inv1} gives

$$r_{inv1} = r_{bg}(1 + (3\phi)^{2/3})^{1/2}. \tag{2.21}$$

A binomial expansion and elimination of higher order terms allows even a more convenient form for integrations.

$$r_{inv1} = r_{bg}(1 + \frac{1}{2}(3\phi)^{2/3}). \tag{2.22}$$

A comparison of the actual involute to the approximation for one set of gears is given in Figure 2.9. The other limit of integration,r_{pin}, is the addendum of the pinion with respect to the origin of the gear. It is derived in Figure 2.10 by using a coordinate transformation.

$$r_{pin} = (r_{pg} + r_{pp}) \cos \theta - \sqrt{r_{ap}^2 - (r_{pg} + r_{pp})^2 \sin^2 \theta}. \tag{2.23}$$

The positions of the gear tooth centerline where θ is defined from the $x - axis$ for the beginning and end points for each set of integrals were designated respectively as $start_1$ and $stop_1$ for Set 1 and $start_2$ and $stop_2$ for Set 2 etc. When the angle of the centerline of the gear tooth falls between angle $start_1$

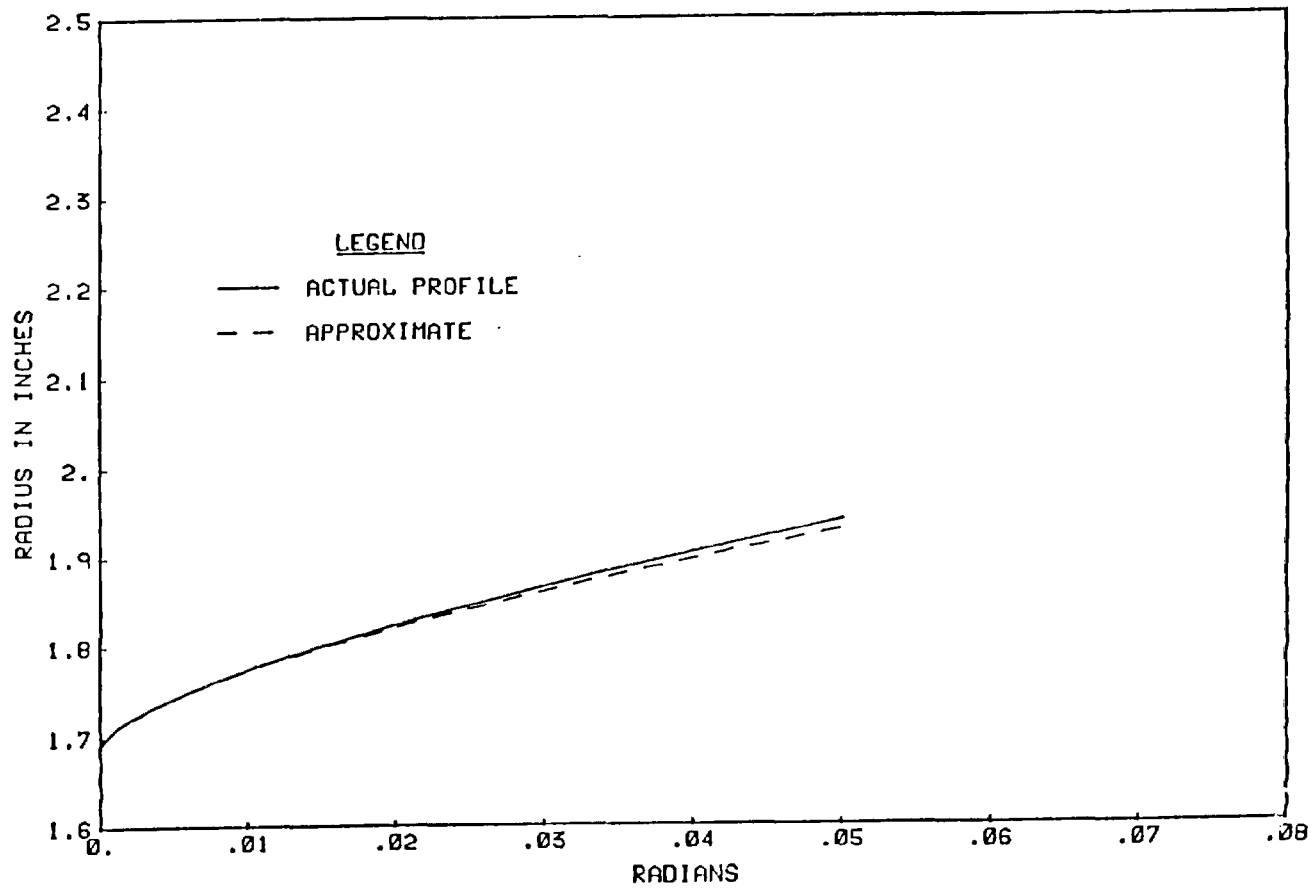

Figure 2.9 Comparison of the actual radius profile to the approximate profile.

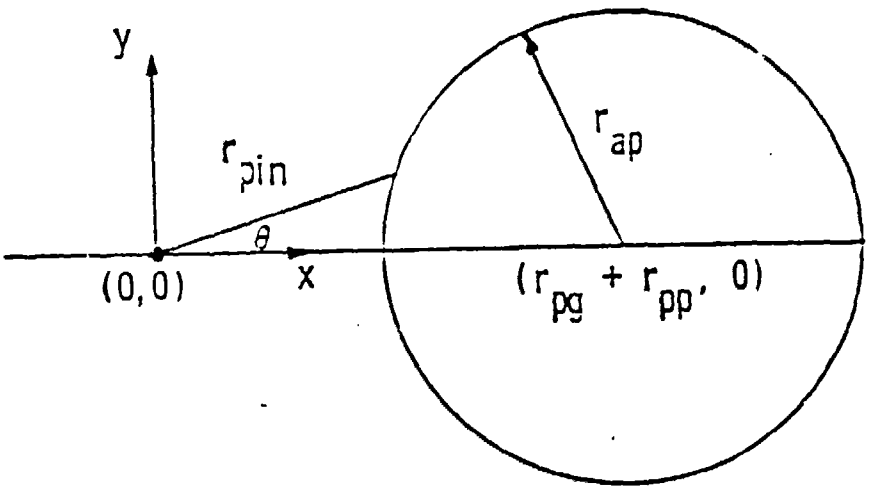

Figure 2.10 Addendum of the Pinion. The addendum of the pinion, r_{pin}, using a coordinate transformation with respect to the center of the driving gear, (0,0).

and $stop_1$ integral Set 1 is used. The overlap was calculated by first integrating the complete area under the tooth profile and then subtracting the area under the pinion addendum curve. The tooth profile uses a local coordinate system for the angle integration $d\phi$ and the pinion addendum uses a global system $d\theta$. See Figure 2.11 for details.

The beginning of Set 1 occurs when the tooth tip of the leading edge contacts the addendum circle of pinion.

$$start_1 = \arccos\left[\frac{r_{ap}^2 - r_{ag}^2 - (r_{pg} + r_{pp})^2}{-2r_{ag}(r_{pg} + r_{pp})}\right] + \frac{1}{2}\frac{t_{ag}}{r_{ag}}, \tag{2.24}$$

where t_{ag} is the thickness of the gear at the addendum circle. $Stop_1$ ends the set when the trailing edge involute enters addendum circle. Figure 2.12 gives details of angles.

$$stop_1 = start_1 - \frac{t_{ag}}{r_{ag}}. \tag{2.25}$$

The integrals for Set 1 are

$$overlap_{area} = \int_{B-X}^{C-X}\int_{0}^{r_{invl}} r\,dr\,d\phi + \int_{C-X}^{D-X}\int_{0}^{r_{ag}} r\,dr\,d\phi - \int_{B}^{D}\int_{0}^{r_{pin}} r\,dr\,d\theta, \tag{2.26}$$

where angle X is from the x_{axis} to the leading edge of the gear, angle B is the point on the involute profile that intersects the addendum of the pinion, angle C is the end of the involute profile and angle D is the point of intersection for the two addendum circles.

Evaluating each integral over its limits gives:

$$\begin{aligned}\int_{B-X}^{C-X}\int_{0}^{r_{invl}} r\,dr\,d\phi = \frac{1}{2}r_{bg}^2\Big[&(C-X)-(B-X)\\ &+\frac{3}{5}\times 3^{2/3}\times\left((C-X)^{5/3}-(B-X)^{5/3}\right)\\ &+\frac{3}{28}\times 3^{4/3}\times\left((C-X)^{7/3}-(B-X)^{7/3}\right)\Big]\end{aligned} \tag{2.27}$$

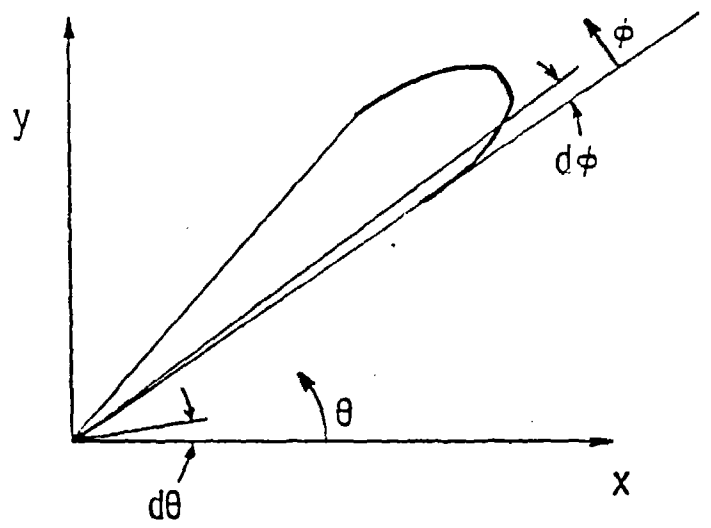

Figure 2.11 Local and Global Angles. The angle θ measures from the x-axis and the angle ϕ begins at the edge of the tooth.

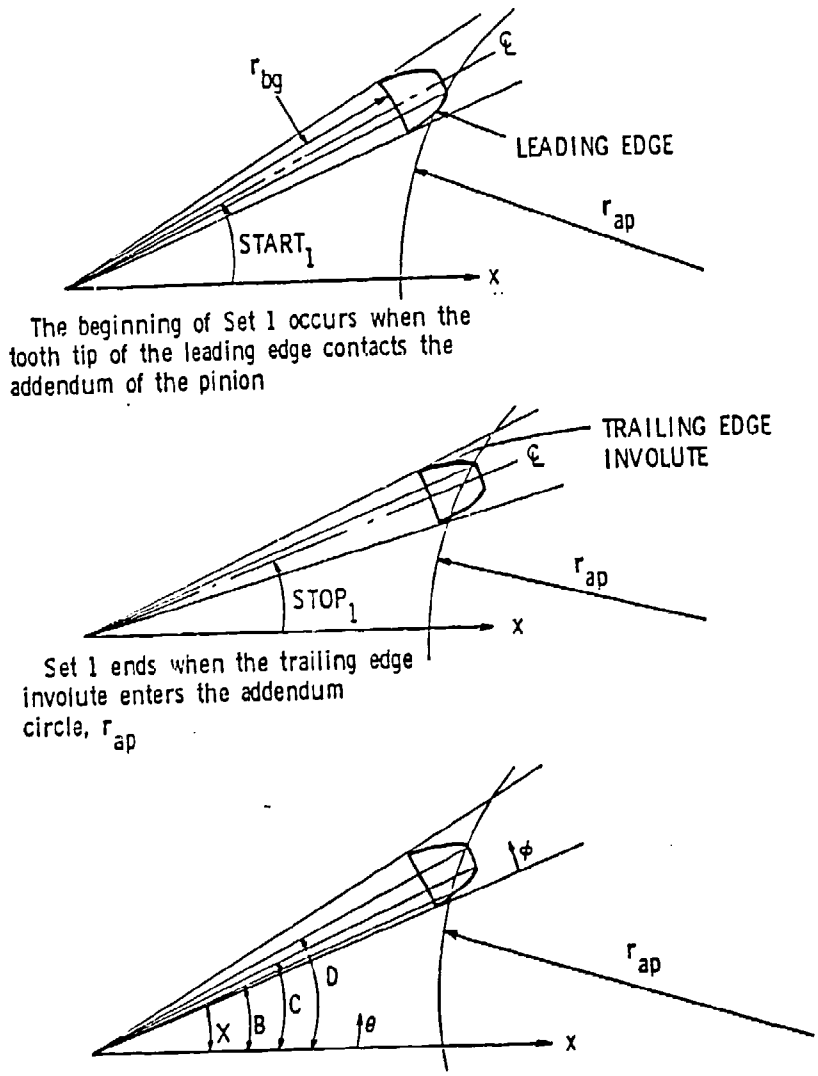

SAMPLE INTEGRAL FOR SET 1

Figure 2.12 Integral Set 1.

and

$$\int_{C-X}^{D-X}\int_{0}^{r_{ag}} r\,dr\,d\phi = \frac{1}{2}r_{ag}^2\left[(D-X)-(C-X)\right] \tag{2.28}$$

and

$$\begin{aligned}\int_{B}^{D}\int_{0}^{r_{pin}} r\,dr\,d\theta = {} & \frac{1}{2}(\sin 2D - \sin 2B)(r_{pg}+r_{pp})^2 + r_{ap}^2(D-B) \\ & - 2(r_{pg}+r_{pp})r_{ap} \\ & \Bigg[\frac{1}{2}\sin D\sqrt{1-(\frac{r_{pg}+r_{pp}}{r_{ap}})^2\sin^2 D} \\ & - \frac{1}{2}\sin B\sqrt{1-(\frac{r_{pg}+r_{pp}}{r_{ap}})^2\sin^2 B} \\ & - \frac{1}{2}\frac{r_{ap}}{r_{pg}+r_{pp}}\Big(\arcsin\Big((\frac{r_{pg}+r_{pp}}{r_{ap}})\sin D\Big) \\ & - \arcsin\Big((\frac{r_{pg}+r_{pp}}{r_{ap}})\sin B\Big)\Big)\Bigg].\end{aligned} \tag{2.29}$$

The beginning of Set 2 is at the end of Set 1.

$$start_2 = stop_1\ . \tag{2.30}$$

$Stop_2$ occurs when the base circle at the leading edge of involute enters the addendum of pinion. See Figure 2.13.

$$stop_2 = \arccos\left[\frac{r_{ap}^2 - r_{bg}^2 - (r_{pg}+r_{pp})^2}{-2r_{bg}(r_{pg}+r_{pp})}\right] + \frac{1}{2}\frac{t_{ag}}{r_{ag}} + E_g. \tag{2.31}$$

The integrals for Set 2

$$\begin{aligned} overlap_{area} = {} & + \int_{B-X}^{C-X}\int_{0}^{r_{inv1}} r\,dr\,d\phi + \int_{C-X}^{F-X}\int_{0}^{r_{ag}} r\,dr\,d\phi \\ & + \int_{F-X}^{G-X}\int_{0}^{r_{inv2}} r\,dr\,d\phi - \int_{B}^{G}\int_{0}^{r_{pin}} r\,dr\,d\theta, \end{aligned} \tag{2.32}$$

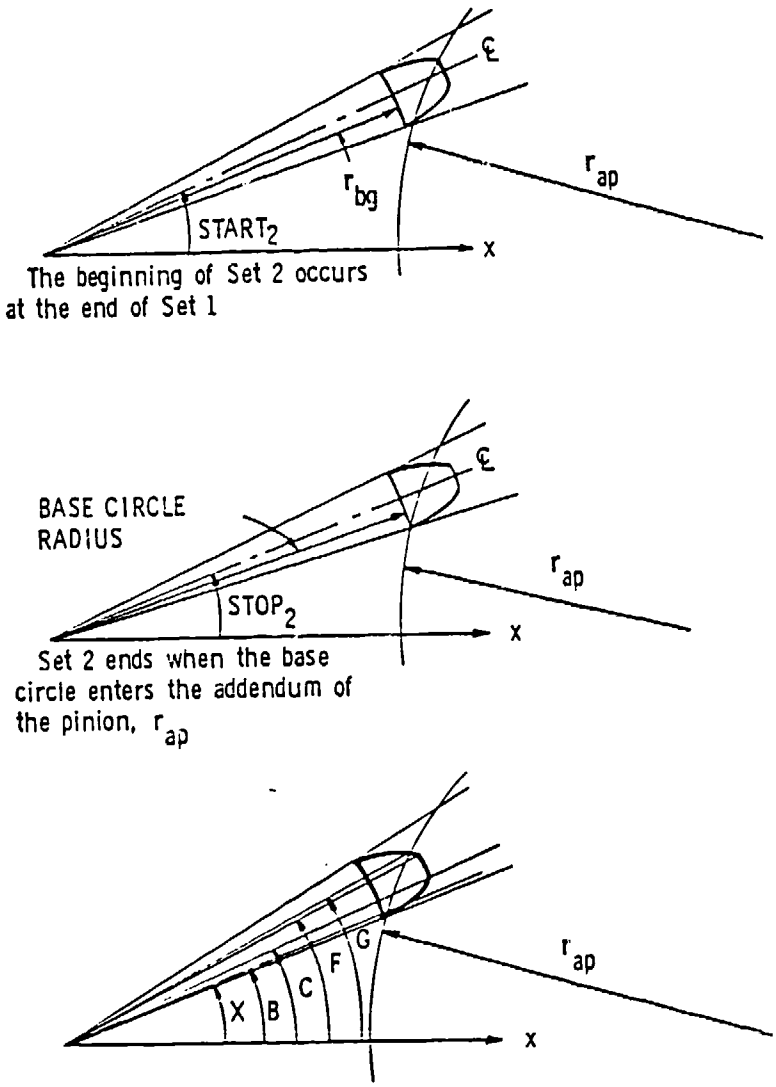

Figure 2.13 Integral Set 2.

where angles $X, B, \& \ C$ are as defined for Set 1 and angle F is from the $x-axis$ to the start of the trailing edge involute and angle G is the intersection point for the trailing edge involute and the addendum circle of the pinion.

Evaluating each integral over its limits gives

$$\int_{B-X}^{C-X} \int_{0}^{r_{inv1}} r\,dr\,d\phi = \frac{1}{2} r_{bg}^2 \Big[(C-X) - (B-X) + \frac{3}{5} \times 3^{2/3} \times \left((C-X)^{5/3} - (B-X)^{5/3} \right) + \frac{3}{28} \times 3^{4/3} \times \left((C-X)^{7/3} - (B-X)^{7/3} \right) \Big] \tag{2.33}$$

and

$$\int_{C-X}^{F-X} \int_{0}^{r_{ag}} r\,dr\,d\phi = \frac{1}{2} r_{ag}^2 \left[(F-X) - (C-X) \right] \tag{2.34}$$

and

$$\int_{F-X}^{G-X} \int_{0}^{r_{inv2}} r\,dr\,d\phi = \frac{1}{2} r_{bg}^2 \Big[(tr_{bg} - (G-X)) - (tr_{bg} - (F-X)) + \frac{3}{5} \times 3^{2/3} \times \left((tr_{bg} - (G-X))^{5/3} - (tr_{bg} - (F-X))^{5/3} \right) + \frac{3}{28} \times 3^{4/3} \times \left((tr_{bg} - (G-X))^{7/3} - (tr_{bg} - (F-X))^{7/3} \right) \Big] \tag{2.35}$$

and

$$\int_B^G \int_0^{r_{pin}} r\,dr\,d\theta = \frac{1}{2}(\sin 2G - \sin 2B)(r_{pg} + r_{pp})^2 + r_{ap}^2(G - B)$$
$$- 2(r_{pg} + r_{pp})r_{ap}$$
$$\left[\frac{1}{2}\sin G\sqrt{1 - (\frac{r_{pg} + r_{pp}}{r_{ap}})^2 \sin^2 G}\right.$$
$$- \frac{1}{2}\sin B\sqrt{1 - (\frac{r_{pg} + r_{pp}}{r_{ap}})^2 \sin^2 B}$$
$$- \frac{1}{2}\frac{r_{ap}}{r_{pg} + r_{pp}}(\arcsin\left((\frac{r_{pg} + r_{pp}}{r_{ap}})\sin G\right)$$
$$\left. - \arcsin\left((\frac{r_{pg} + r_{pp}}{r_{ap}})\sin B\right))\right]. \tag{2.36}$$

Set 3 starts with the end of Set 2.

$$start_3 = stop_2. \tag{2.37}$$

$Stop_3$ occurs when the base circle at the trailing edge of involute enters the addendum of pinion. See Figure 2.14.

$$stop_3 = start_3 - tr_{bg}. \tag{2.38}$$

where tr_{bg} is the thickness of the gear at the base circle in radians. Set 3 has two cases for its integral sets. Case one the leading edge of the gear tooth is above

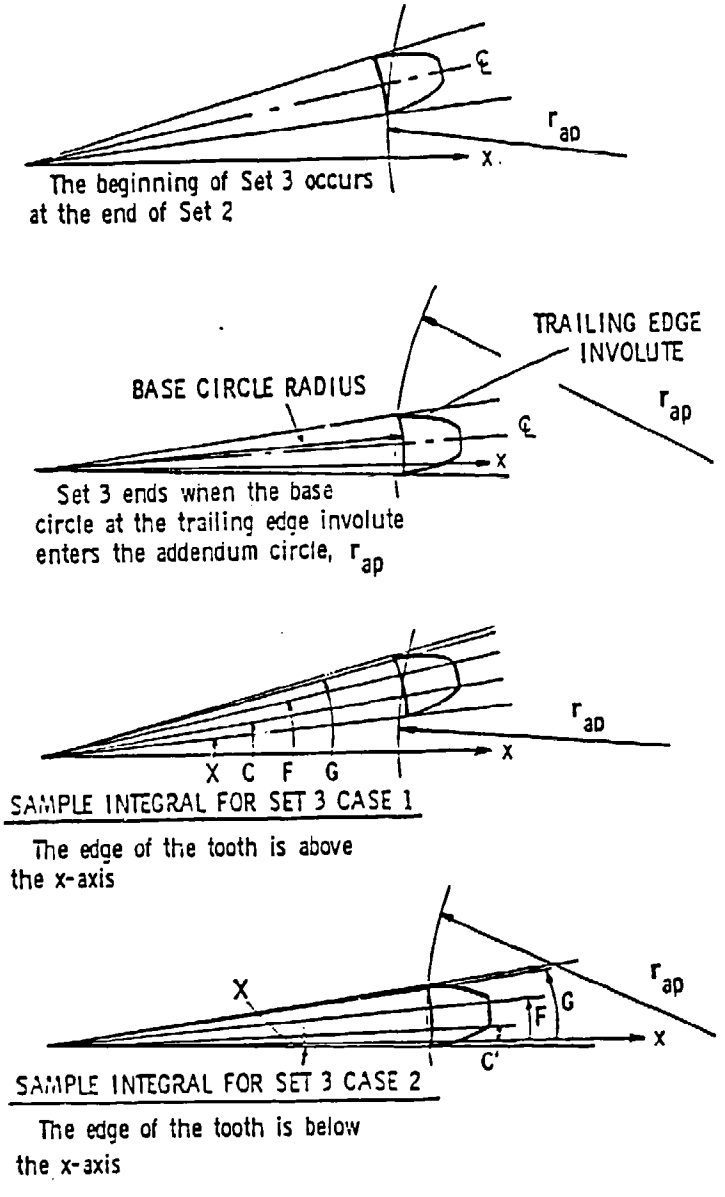

Figure 2.14 Integral Set 3.

the x-axis and Case two it is below the x-axis. The integrals for calculation are

$$overlap_{area} = \int_{0}^{C-X} \int_{0}^{r_{inv1}} r\,dr\,d\phi + \int_{C-X}^{F-X} \int_{0}^{r_{rag}} r\,dr\,d\phi$$
$$+ \int_{F-X}^{G-X} \int_{0}^{r_{inv2}} r\,dr\,d\phi$$

case one

$$- \int_{X}^{G} \int_{0}^{r_{pin}} r\,dr\,d\theta \tag{2.39}$$

case two

$$- \int_{0}^{G} \int_{0}^{r_{pin}} r\,dr\,d\theta - \int_{X}^{0} \int_{0}^{r_{pin}} r\,dr\,d\theta,$$

where angles $X, C, F, \& \ G$ have been defined previously. Evaluating each of the integrals gives

$$\int_{0}^{C-X} \int_{0}^{r_{inv1}} r\,dr\,d\phi = \frac{1}{2} r_{bg}^2 \Big[(C-X) + \frac{3}{5} \times 3^{2/3} \times ((C-X)^{5/3}) + \frac{3}{28} \times 3^{4/3} \times ((C-X)^{7/3}) \Big] \tag{2.40}$$

$$\int_{C-X}^{F-X} \int_{0}^{r_{rag}} r\,dr\,d\phi = \frac{1}{2} r_{ag}^2 [(F-X) - (C-X)] \tag{2.41}$$

$$\int_{F-X}^{G-X}\int_{0}^{r_{inv2}} r\,dr\,d\phi = \frac{1}{2}r_{bg}^2\Big[(tr_{bg}-(G-X))-(tr_{bg}-(F-X))$$
$$+3^{2/3}\times\frac{3}{5}\times((tr_{bg}-(G-X))^{5/3}$$
$$-(tr_{bg}-(F-X))^{5/3})$$
$$+\frac{3}{28}\times 3^{4/3}\times((tr_{bg}-(G-X))^{7/3}-$$
$$(tr_{bg}-(F-X))^{7/3})\Big] \tag{2.42}$$

$$\int_{X}^{G}\int_{0}^{r_{pin}} r\,dr\,d\theta = \frac{1}{2}(\sin 2G-\sin 2X)(r_{pg}+r_{pp})^2+r_{ap}^2(G-X)$$
$$-2(r_{pg}+r_{pp})r_{ap}$$
$$\Big[\frac{1}{2}\sin G\sqrt{1-(\frac{r_{pg}+r_{pp}}{r_{ap}})^2\sin^2 G}$$
$$-\frac{1}{2}\sin X\sqrt{1-(\frac{r_{pg}+r_{pp}}{r_{ap}})^2\sin^2 X} \tag{2.43}$$
$$-\frac{1}{2}\frac{r_{ap}}{r_{pg}+r_{pp}}(\arcsin\Big((\frac{r_{pg}+r_{pp}}{r_{ap}})\sin G\Big)$$
$$-\arcsin\Big((\frac{r_{pg}+r_{pp}}{r_{ap}})\sin X\Big))\Big]$$

$$\int_{0}^{G}\int_{0}^{r_{pin}} r\,dr\,d\theta = \frac{1}{2}(\sin 2G)(r_{pg}+r_{pp})^2+r_{ap}^2(G)$$
$$-2(r_{pg}+r_{pp})r_{ap}$$
$$\Big[\frac{1}{2}\sin G\sqrt{1-(\frac{r_{pg}+r_{pp}}{r_{ap}})^2\sin^2 G} \tag{2.44}$$
$$+\frac{1}{2}\frac{r_{ap}}{r_{pg}+r_{pp}}(\arcsin\Big((\frac{r_{pg}+r_{pp}}{r_{ap}})\sin G\Big))\Big]$$

$$\int_{X}^{0}\int_{0}^{r_{pin}} r\,dr\,d\theta = -\frac{1}{2}(\sin 2X)(r_{pg}+r_{pp})^2 - r_{ap}^2(X)$$
$$+ 2(r_{pg}+r_{pp})r_{ap}$$
$$\left[\frac{1}{2}\sin X\sqrt{1-(\frac{r_{pg}+r_{pp}}{r_{ap}})^2\sin^2 X}\right.$$
$$\left.+\frac{1}{2}\frac{r_{ap}}{r_{pg}+r_{pp}}(\arcsin\left((\frac{r_{pg}+r_{pp}}{r_{ap}})\sin X\right))\right]. \tag{2.45}$$

Set 4 starts at the end of Set 3.

$$start_4 = stop_3. \tag{2.46}$$

Set 4 stops when the centerline of the gear tooth reaches the x-axis. See Figure 2.15.

$$stop_4 = 0.0. \tag{2.47}$$

The integrals are

$$overlap_{area} = \int_{0}^{C-X}\int_{0}^{r_{inv1}} r\,dr\,d\phi + \int_{C-X}^{F-X}\int_{0}^{r_{ag}} r\,dr\,d\phi$$
$$+\int_{F-X}^{H-X}\int_{0}^{r_{inv2}} r\,dr\,d\phi - \int_{0}^{H}\int_{0}^{r_{pin}} r\,dr\,d\theta \tag{2.48}$$
$$-\int_{X}^{0}\int_{0}^{r_{pin}} r\,dr\,d\theta,$$

where angles $X, C, \& F$ have been defined previously and angle H is the angles from the $x-axis$ to the trailing edge of the driving tooth. Evaluating each integral over its limits gives

$$\int_{0}^{C-X}\int_{0}^{r_{inv1}} r\,dr\,d\phi = \frac{1}{2}r_{bg}^2\left[(C-X)+3^{2/3}\times\frac{3}{5}\times((C-X)^{5/3})\right.$$
$$\left.+\frac{3}{28}\times 3^{4/3}\times((C-X)^{7/3})\right] \tag{2.49}$$

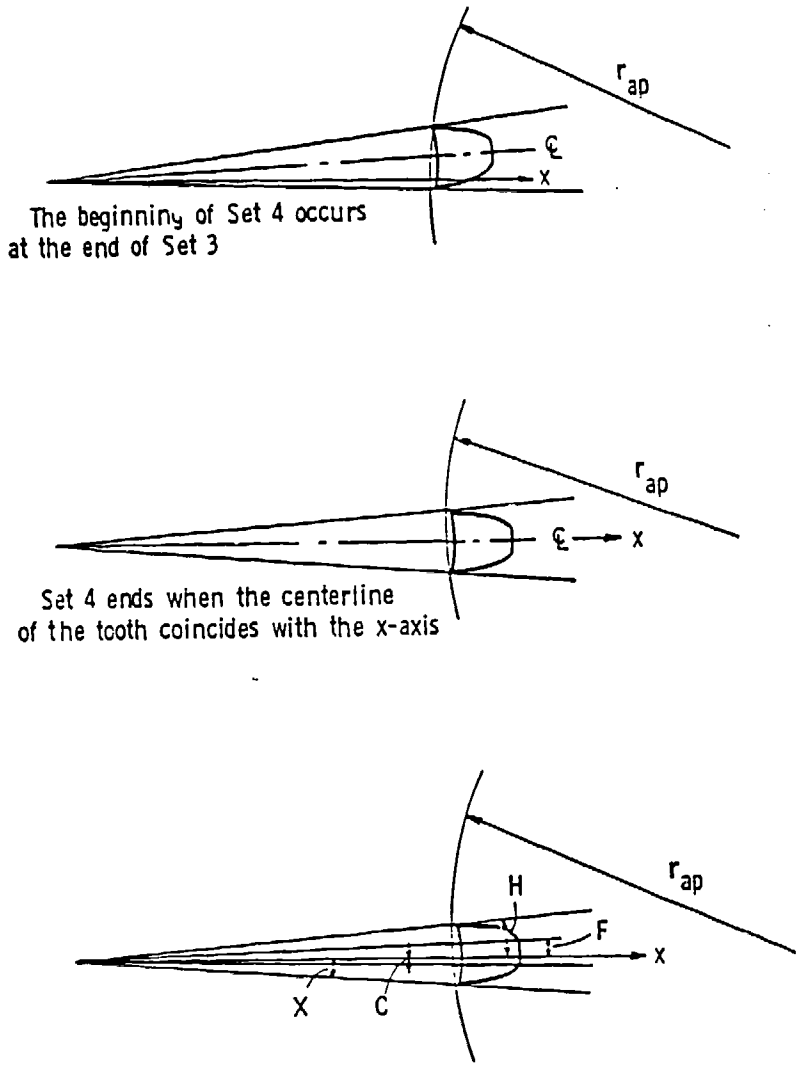

Figure 2.15 Integral Set 4.

$$\int_{C-X}^{F-X}\int_{0}^{r_{ag}} r\,dr\,d\phi = \frac{1}{2}r_{ag}^2[(F-X)-(C-X)] \tag{2.50}$$

$$\begin{aligned}\int_{F-X}^{H-X}\int_{0}^{r_{inv2}} r\,dr\,d\phi = \frac{1}{2}r_{bg}^2\Big[&(tr_{tg}-(H-X))-(tr_{bg}-(F-X))\\ &+3^{2/3}\times\frac{3}{5}\times((tr_{bg}-(H-X))^{5/3}\\ &-(tr_{bg}-(F-X))^{5/3})\\ &+\frac{3}{28}\times 3^{4/3}\times((tr_{bg}-(H-X))^{7/3}\\ &-(tr_{bg}-(F-X))^{7/3})\Big]\end{aligned} \tag{2.51}$$

$$\begin{aligned}\int_{0}^{H}\int_{0}^{r_{pin}} r\,dr\,d\theta = &\frac{1}{2}(\sin 2H)(r_{pg}+r_{pp})^2 + r_{ap}^2(H)\\ &-2(r_{pg}+r_{pp})r_{ap}\\ &\Big[\frac{1}{2}\sin H\sqrt{1-(\frac{r_{pg}+r_{pp}}{r_{ap}})^2\sin^2 H}\\ &+\frac{1}{2}\frac{r_{ap}}{r_{pg}B+r_{pp}}(\arcsin\Big((\frac{r_{pg}+r_{pp}}{r_{ap}})\sin H\Big))\Big]\end{aligned} \tag{2.52}$$

$$\begin{aligned}\int_{X}^{0}\int_{0}^{r_{pin}} r\,dr\,d\theta = &-\frac{1}{2}(\sin 2X)(r_{pg}+r_{pp})^2 - r_{ap}^2(X)\\ &+2(r_{pg}+r_{pp})r_{ap}\\ &\Big[\frac{1}{2}\sin X\sqrt{1-(\frac{r_{pg}+r_{pp}}{r_{ap}})^2\sin^2 X}\\ &+\frac{1}{2}\frac{r_{ap}}{r_{pg}+r_{pp}}(\arcsin\Big((\frac{r_{pg}+r_{pp}}{r_{ap}})\sin X\Big))\Big].\end{aligned} \tag{2.53}$$

When the base circle of the gear does not overlap the pinion addendum only two sets of integrals result: Sets 5 and 6. Set 5 begins when the leading edge of

the tooth tip enters the addendum circle of the pinion. See Figure 2.16.

$$start_5 = \arccos\left[\frac{r_{ap}^2 - r_{ag}^2 - (r_{pg} + r_{pp})^2}{-2r_{ag}(r_{pg} + r_{pp})}\right] + \frac{1}{2}\frac{t_{ag}}{r_{ag}}. \tag{2.54}$$

Set 5 ends when the trailing edge involute enters the addendum of the pinion.

$$stop_5 = start_5 - \frac{t_{ag}}{r_{ag}}. \tag{2.55}$$

$$\begin{aligned} overlap_{area} = & \int_{S-R}^{T-R} \int_0^{r_{invl}} r\,dr\,d\phi + \int_{T-R}^{U-R} \int_0^{r_{ag}} r\,dr\,d\phi \\ & - \int_S^U \int_0^{r_{pin}} r\,dr\,d\theta, \end{aligned} \tag{2.56}$$

where angle R is from the x-axis to the leading edge of the driving tooth, angle S to the intersection of the leading involute profile and the addendum of the pinion, angle T to the end of leading profile, angle V to the beginning of the trailing edge profile, and angle W to the intersection of the trailing edge profile and the addendum circle of the pinion. Evaluating each integral gives

$$\begin{aligned} \int_{S-R}^{T-R} \int_0^{r_{invl}} r\,dr\,d\phi = & \frac{1}{2}r_{bg}^2\Big[(T-R) - (S-R) \\ & + 3^{2/3} \times \frac{3}{5} \times ((T-R)^{5/3} - (S-R)^{5/3}) \\ & + \frac{3}{28} \times 3^{4/3} \times ((T-R)^{7/3} - (S-R)^{7/3})\Big] \end{aligned} \tag{2.57}$$

$$\int_{T-R}^{U-R} \int_0^{r_{ag}} r\,dr\,d\phi = \frac{1}{2}r_{ag}^2[(U-R) - (T-R)] \tag{2.58}$$

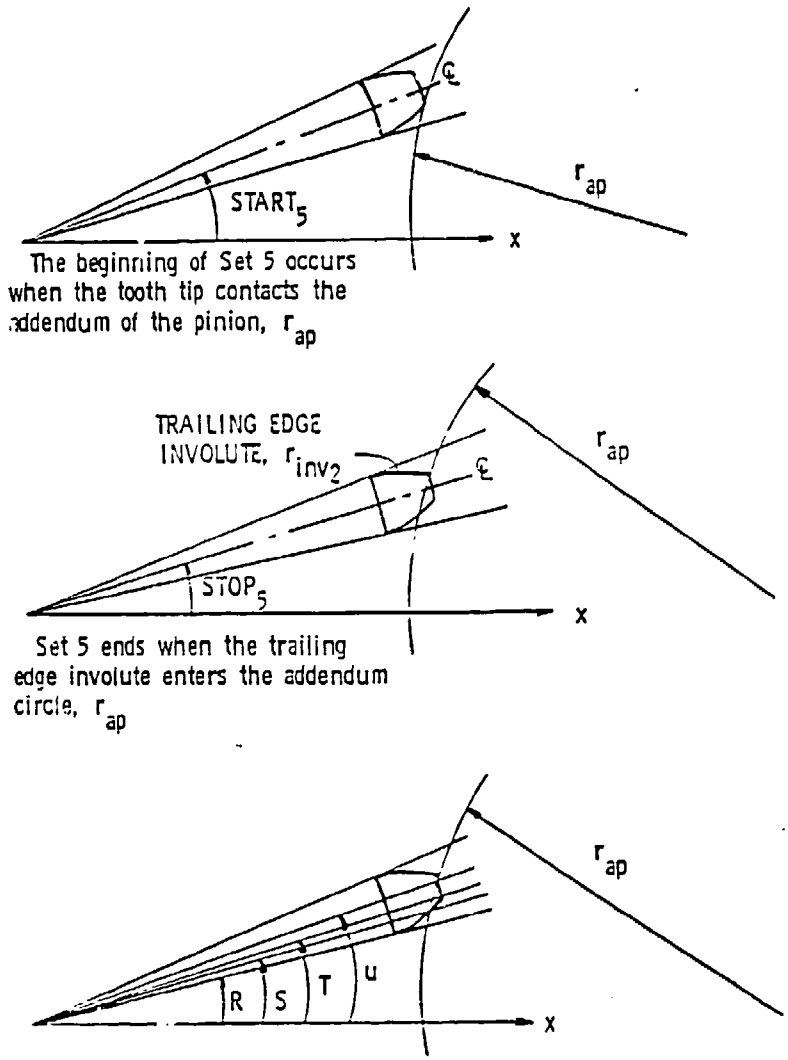

Figure 2.16 Integral Set 5.

$$\int_S^U \int_0^{r_{pin}} r\,dr\,d\theta = \frac{1}{2}(\sin 2U - \sin 2S)(r_{pg} + r_{pp})^2 + r_{ap}^2(U - S)$$
$$- 2(r_{pg} + r_{pp})r_{ap}$$
$$\left[\frac{1}{2}\sin U\sqrt{1 - (\frac{r_{pg} + r_{pp}}{r_{ap}})^2 \sin^2 U}\right.$$
$$- \frac{1}{2}\sin S\sqrt{1 - (\frac{r_{pg} + r_{pp}}{r_{ap}})^2 \sin^2 S}$$
$$- \frac{1}{2}\frac{r_{ap}}{r_{pg} + r_{pp}}\left(\arcsin\left((\frac{r_{pg} + r_{pp}}{r_{ap}})\sin U\right)\right.$$
$$\left.\left. - \arcsin\left((\frac{r_{pg} + r_{pp}}{r_{ap}})\sin S\right)\right)\right]. \tag{2.59}$$

The beginning of Set 6 starts at the end of Set 5.

$$start_6 = stop_5. \tag{2.60}$$

Set 6 ends when the centerline of the gear coincides with the x-axis. See Figure 2.17.

$$stop_6 = 0.0\ . \tag{2.61}$$

$$overlap_{area} = \int_{S-R}^{T-R} \int_0^{r_{inv1}} r\,dr\,d\phi + \int_{T-R}^{V-R} \int_0^{r_{ag}} r\,dr\,d\phi$$
$$+ \int_{V-R}^{W-R} \int_0^{r_{inv2}} r\,dr\,d\phi$$

for case one

$$- \int_R^W \int_0^{r_{pin}} r\,dr\,d\theta \tag{2.62}$$

for case two

$$- \int_0^W \int_0^{r_{pin}} r\,dr\,d\theta - \int_R^0 \int_0^{r_{pin}} r\,dr\,d\theta.$$

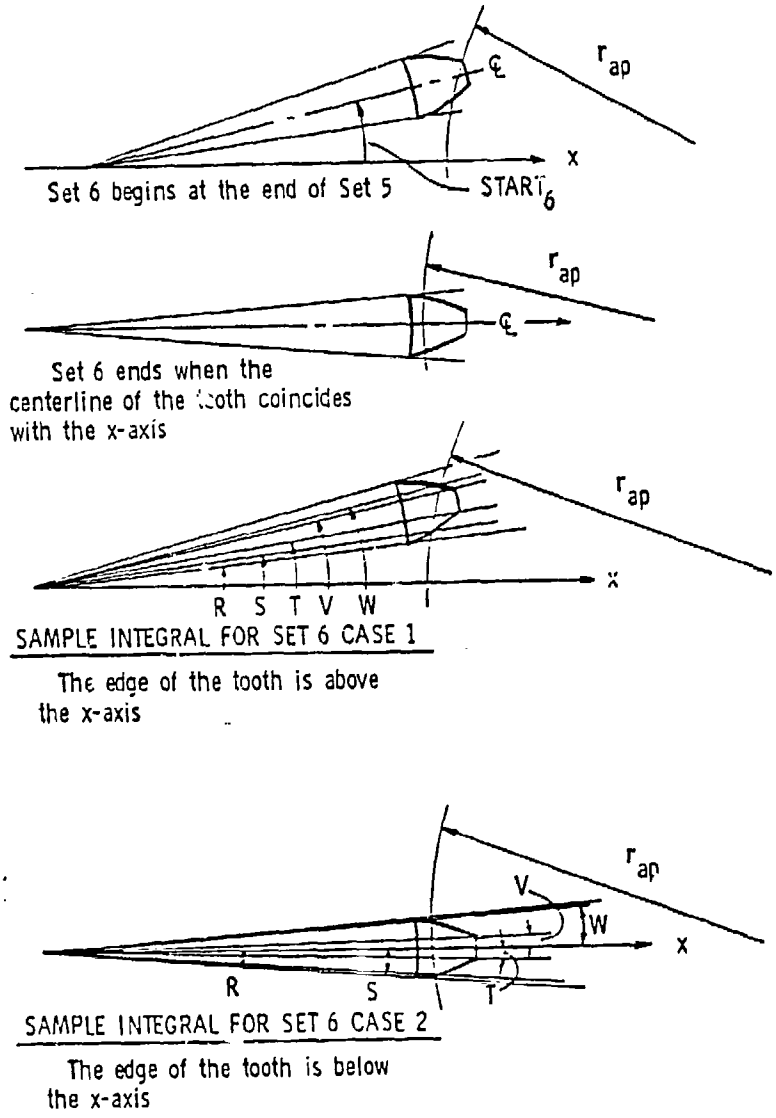

Figure 2.17 Integral Set 6.

Evaluating each integral gives

$$\int_{S-R}^{T-R}\int_{0}^{r_{inv1}} r\,dr\,d\phi = \frac{1}{2}r_{bg}^2\Big[(T-R)-(S-R) + \frac{3}{5}\times 3^{2/3}\times((T-R)^{5/3}-(S-R)^{5/3}) + \frac{3}{28}\times 3^{4/3}\times((T-R)^{7/3}-(S-R)^{7/3})\Big] \tag{2.63}$$

$$\int_{T-R}^{V-R}\int_{0}^{r_{ag}} r\,dr\,d\phi = \frac{1}{2}r_{ag}^2[(V-R)-(T-R)] \tag{2.64}$$

$$\begin{aligned}\int_{V-R}^{W-R}\int_{0}^{r_{inv2}} r\,dr\,d\phi = \frac{1}{2}r_{bg}^2\Big[&(tr_{bg}-(W-R))-(tr_{bg}-(V-R)) \\ &+\frac{3}{5}\times 3^{2/3}\times((tr_{bg}-(W-R))^{5/3} \\ &-(tr_{bg}-(V-R))^{5/3}) \\ &+\frac{3}{28}\times 3^{4/3}\times((tr_{bg}-(W-R))^{7/3} \\ &-(tr_{bg}-(V-R))^{7/3})\Big]\end{aligned} \tag{2.65}$$

$$\begin{aligned}\int_{R}^{W}\int_{0}^{r_{pin}} r\,dr\,d\theta = &\frac{1}{2}(\sin 2W-\sin 2R)(r_{pg}+r_{pp})^2+r_{ap}^2(W-R) \\ &-2(r_{pg}+r_{pp})r_{ap} \\ &\Big[\frac{1}{2}\sin W\sqrt{1-(\frac{r_{pg}+r_{pp}}{r_{ap}})^2\sin^2 W} \\ &-\frac{1}{2}\sin R\sqrt{1-(\frac{r_{pg}+r_{pp}}{r_{ap}})^2\sin^2 R} \\ &-\frac{1}{2}\frac{r_{ap}}{r_{pg}+r_{pp}}\Big(\arcsin\Big((\frac{r_{pg}+r_{pp}}{r_{ap}})\sin W\Big) \\ &-\arcsin\Big((\frac{r_{pg}+r_{pp}}{r_{ap}})\sin R\Big)\Big)\Big]\end{aligned} \tag{2.66}$$

$$\int_0^W \int_0^{r_{pin}} r\,dr\,d\theta = \frac{1}{2}(\sin 2W)(r_{pg}+r_{pp})^2 + r_{ap}^2(W) - 2(r_{pg}+r_{pp})r_{ap} \left[\frac{1}{2}\sin W\sqrt{1-(\frac{r_{pg}+r_{pp}}{r_{ap}})^2\sin^2 W} + \frac{1}{2}\frac{r_{ap}}{r_{pg}+r_{pp}}(\arcsin\Big((\frac{r_{pg}+r_{pp}}{r_{ap}})\sin W\Big))\right] \tag{2.67}$$

$$\int_R^0 \int_0^{r_{pin}} r\,dr\,d\theta = -\frac{1}{2}(\sin 2R)(r_{pg}+r_{pp})^2 - r_{ap}^2(R) + 2(r_{pg}+r_{pp})r_{ap} \left[\frac{1}{2}\sin R\sqrt{1-(\frac{r_{pg}+r_{pp}}{r_{ap}})^2\sin^2 R} + \frac{1}{2}\frac{r_{ap}}{r_{pg}+r_{pp}}(\arcsin\Big((\frac{r_{pg}+r_{pp}}{r_{ap}})\sin R\Big))\right]. \tag{2.68}$$

The area subtracted from the space between two pinion teeth is derived from the discharge area and is designated as the $excluded_{area}$. When the chord length along the disharge area is known, the area from the exit plane out to the addendum of the pinion can be calculated. The area above the pinion involute profile can also be calculated. See Figure 2.18. At the point in the meshing cycle when the tooth tip of the driving gear is no longer the closest point to the driven tooth (see chord 2 description), another approximation is used to compute the excluded area. A cubic equation is fit using the last area calculated and an estimation of the final value. The integrals are

$$excluded_{area} = \int_0^{P_o}\int_{P_L}^{r_{ap}} r\,dr\,d\phi + \int_{P_7}^{E_p}\int_0^{r_{ap}} r\,dr\,d\phi - \int_{P_7}^{E_p}\int_0^{r_{invl}} r\,dr\,d\phi. \tag{2.69}$$

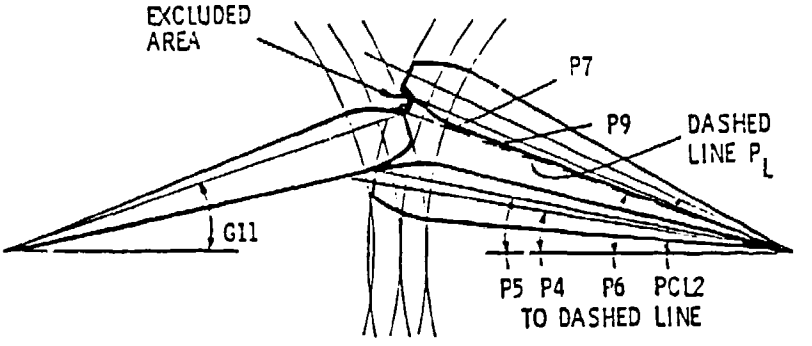

Figure 2.18 Excluded Area. Calculation of the area excluded from the control volume.

Evaluating each integral gives

$$\int_{0}^{P_9}\int_{P_L}^{r_{ap}} r\,dr\,d\phi = \frac{1}{2}P_9(r_{ap}^2 - P_L^2) \tag{2.70}$$

$$\int_{P_7}^{E_p}\int_{0}^{r_{ap}} r\,dr\,d\phi = \frac{1}{2}r_{ap}^2(E_p - P_7) \tag{2.71}$$

$$\begin{aligned}\int_{P_7}^{E_p}\int_{0}^{r_{invl}} r\,dr\,d\phi = \frac{1}{2}[(E_p - P_7) + \frac{3}{5}\times 3^{2/3}\times(E_p^{5/3} - P_7^{5/3}) \\ + \frac{3}{28}\times 3^{4/3}\times(E_p^{7/3} - P_7^{7/3})].\end{aligned} \tag{2.72}$$

The total plane area subtracted equals

$$\begin{aligned}exluded_{area} = &\frac{1}{2}P_9(r_{ap}^2 - P_L^2) \\ &\frac{1}{2}r_{ap}^2(E_p - P_7) \\ &\frac{1}{2}[(E_p - P_7) \\ &+ \frac{3}{5}\times 3^{2/3}\times(E_p^{5/3} - P_7^{5/3}) \\ &+ \frac{3}{28}\times 3^{4/3}\times(E_p^{7/3} - P_7^{7/3})].\end{aligned} \tag{2.73}$$

This chapter has presented a method of solution of incompressible flow of air between spur gear teeth. Through the use of assumptions, a numerical representation of the change in discharge area and change in volume were given.

Chapter 3

COMPRESSIBLE FLOW THEORY

3.1. Introduction

By taking into account density changes, an approximation of the velocity for a perfect gas resulting from the meshing of a gear and stationary rack was developed. To develop the velocity equation, the First Law of Thermodynamics was applied to relate the fluid properties along a streamline from inside the control volume, where the velocity is assumed to be low, to the exit plane. To determine the pressure relationship, the continuity equation was applied to the control volume.

An ideal gas and one-dimensional flow model with constant entropy and adiabatic flow was assumed. This gives constant properties for the velocity, pressure, density, and temperature across the flow area. The assumption of constant entropy, $ds = 0$, allows any thermodynamic variable to be found in terms of any other thermodynamic variable. Isentropic flow can be assumed because friction effects are small over the short distance of accelerating flow and heat transfer is small because of the short time intervals. The analysis began at the angle of approach when contact first occurs between the driving and driven teeth. Before contact occurred, it was assumed that the pressure inside the control volume was the same as the ambient and no flow occurred. The discharge area evaluation and the volume are the same as the incompressible case and were described in Chapter 2.

3.2. Velocity Equation

Applying the First Law of Thermodynamics along a streamline gives the velocity equation. The pressure relationship of the velocity equation is derived

by applying continuity to the control volume.

3.2.1. Energy Equation

Applying the First Law of Thermodynamics along a streamline for adiabatic conditions gives

$$h_i + \frac{v_i^2}{2g_c} = h_e + \frac{v_e^2}{2g_c}, \tag{3.1}$$

where v_i is the velocity inside the control volume, v_e is the velocity at the exit plane, h_i and h_e are the enthalpy inside the control volume and at the exit plane, g_c is a dimensional constant, and c_p is the specific heat at constant pressure. Rewriting the first law with $v_i = 0$ and $h = c_pT$ gives

$$c_pT_i = c_pT_e + \frac{v_e^2}{2g_c}. \tag{3.2}$$

Solving for the velocity squared at the exit plane gives

$$v_e^2 = 2g_cc_p(T_i - T_e) \tag{3.3}$$

$$v_e^2 = 2g_cc_pT_i(1 - \frac{T_e}{T_i}). \tag{3.4}$$

Dividing both sides of the equation by the pitch line velocity, $\omega \times r_{pg}$, and defining $\tilde{v}_e = v_e/(\omega \times r_{pg})$ and $\tilde{T} = T_i/T_\infty$ results in

$$\tilde{v}_e^2 = \frac{2g_cc_pT_\infty}{(\omega \times r_{pg})^2}\tilde{T}(1 - \frac{T_e}{T_i}). \tag{3.5}$$

Substituting for T_e/T_i with the isentropic relationship $\tilde{P}^{\frac{1-k}{k}}$ where $\tilde{P} = P_i/P_e$ and taking the square root of both sides gives

$$\tilde{v}_e = \frac{\sqrt{2g_cc_pT_\infty}}{\omega \times r_{pg}}\tilde{T}(1 - \tilde{P}^{\frac{1-k}{k}})^{1/2}. \tag{3.6}$$

The pressure variable, $\tilde{P}$, is evaluated in section 3.2.2. by applying the continuity equation to the control volume. The temperature, T, is evaluated by using the isentropic relationship

$$\frac{T_i}{T_e} = (\frac{P_i}{P_e})^{\frac{k-1}{k}}. \tag{3.7}$$

The other relationship can be written as

$$\frac{P_i}{P_e} = (\frac{\rho_i}{\rho_e})^k. \tag{3.8}$$

3.2.2. Pressure Equation

Writing the continuity equation for the control volume

$$\frac{\partial}{\partial t}\int_V \rho_i dV + \int_S \rho_e \vec{v}_r \cdot \vec{n} dS = 0. \tag{3.9}$$

where $\vec{v}_r$ is the relative velocity to the exit plane, ρ_i is the density, V is the volume, and S is the surface of the control volume . For the 1-D case

$$\frac{d}{dt}(\rho_i V) + \rho_e A v_r = 0. \tag{3.10}$$

Expanding the equation gives

$$V\frac{d\rho_i}{dt} + \rho_i \frac{dV}{dt} + \rho_e A v_r = 0. \tag{3.11}$$

Multiplying by $\frac{1}{\rho_i V}$ gives

$$\frac{1}{\rho_i}\frac{d\rho_i}{dt} + \frac{1}{V}\frac{dV}{dt} + \frac{\rho_e}{\rho_i}\frac{A}{V}v_r = 0. \tag{3.12}$$

Using the isentropic case and making substitutions gives

$$\frac{1}{k}\frac{1}{P_i}\frac{dP}{dt} + \frac{1}{V}\frac{dV}{dt} + \left(\frac{P_e}{P_i}\right)^{1/k}\frac{A}{V}v = 0. \tag{3.13}$$

Defining $\tilde{P} = P_i/P_e$ and substituting gives

$$\frac{1}{k}\frac{1}{\tilde{P}}\frac{d\tilde{P}}{dt} + \frac{1}{V}\frac{dV}{dt} + \tilde{P}^{-1/k}\frac{A}{V}v_r = 0. \tag{3.14}$$

Using the chain rule for $d\tilde{P}/dt$ and dV/dt gives

$$\frac{1}{k}\frac{1}{\tilde{P}}\frac{d\tilde{P}}{d\theta}\frac{d\theta}{dt} + \frac{1}{V}\frac{dV}{d\theta}\frac{d\theta}{dt} + \tilde{P}^{-1/k}\frac{A}{V}v_r = 0. \tag{3.15}$$

Solving for $d\tilde{P}/d\theta$ gives

$$\frac{d\tilde{P}}{d\theta} = k\left[+\frac{\tilde{P}}{V}\frac{dV}{d\theta} - \tilde{P}^{(k-1)/k}\frac{A}{V}\frac{v_r}{\omega}\right]. \tag{3.16}$$

The pressure, $\tilde{P}$ in equation 3.16, was solved using the Runge-Kutta fourth order formula. The step size, $\Delta\theta$, was chosen by running the program with a small step size and then cutting the value in half and running the program again to compare it to the previous trial step size. When the difference in the results was small, less than 1%, the step size was set.

Until critical conditions are reached, the conditions at the exit plane must be equal to the ambient pressure $\rho_e = \rho_\infty$ and $P_e = P_\infty$. The meshing teeth can be seen to form a converging nozzle. See Figure 3.1. If P_e were larger than P_∞, the stream would expand laterally upon leaving the nozzle; however, an increase in area at subsonic speeds would cause the pressure to rise further. Since P_∞ is the ultimate pressure reached, P_e cannot be larger than P_∞ [14]. Once the pressure in the cavity divided by the ambient has reached the critical ratio, the flow becomes choked and remains at Mach 1.

The compressible velocity, equation 3.6, approximates the condition of lightly lubricated gears where it can be assumed that the fluid is only air. By using this equation, it can be determined whether the velocity reaches levels capable of producing shocks and causing noise. The true velocity should include the effects of the exit plane moving inward and be accounted for in the energy equation. By neglecting it, a difference on the order of 5% is introduced. Also, for two rotating gears the effect of the rotating control volume should be included in the energy equation.

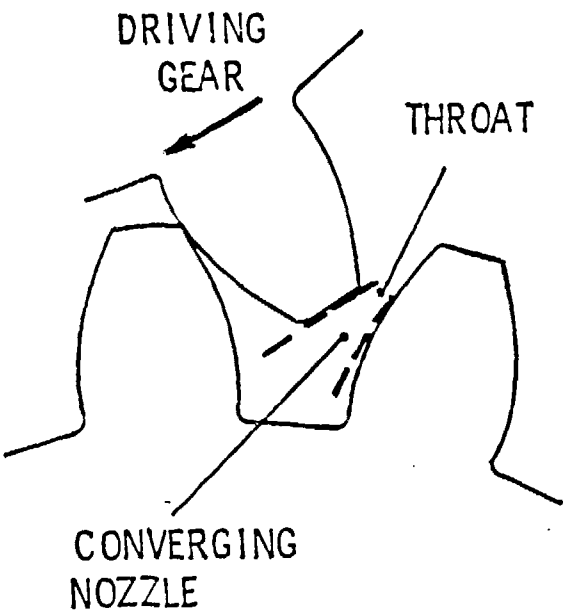

Figure 3.1 Converging Nozzle. The meshing gear teeth forming a converging nozzle.

Chapter 4

RESULTS AND DISCUSSION

4.1. Introduction

When the driving gear contacts the driven pinion tooth, fluid begins to flow out from the volume between the meshing teeth. An estimation of the fluid velocity relative to the exit plane was obtained by using incompressible and compressible flow theories. Figures 4.1 thru 4.7 contain incompressible flow results and Figures 4.8 thru 4.24 have the compressible flow results. Figures 4.25 through 4.27 contain comparisons of incompressible and compressible flow for each of the assumed discharge areas. The geometric parameters for the incompressible flow figures are given in Table 1. Table 2 contains the compressible geometry parameters and Table 3 has the comparison geometries.

It was assumed no flow occurred before the driving tooth contacted the driven tooth and no thermal expansion of the teeth due to temperature rises. The percent of mesh axis on the plots indicates the position of the driving tooth as a percentage of the arc from the initial contact, zero percent mesh, to full mesh position, 100 percent mesh. The velocity is given as a ratio of the computed fluid velocity to the pitch line velocity. The three discharge areas for analysis were end flow area, teeth flow area, and combined flow area. The endflow was chosen to represent the meshing of narrow face width gears. For this case, the fluid is expected to flow primarily out the end openings of teeth. The other extreme is wide face gears. A wide face width should tend to force the discharged air out between the teeth and was designated teeth flow. The combined flow uses equation 2.9 to account for a combination of the two flow areas by using the height of a tooth and the face width. The influence of the geometric parameters including backlash, diametral pitch, drive ratio, and pressure angle

Table 1. Incompressible Parameter Variations to Assess the Effects on Velocity

Figure Number		Number of Teeth	Diametral Pitch teeth/inch	Pitch-line Velocity ft/s	Pressure Angle Degrees	Backlash inches
4.1	driver	31	8.5	150	22	.002
	driven	31	8.5	-	22	.002
4.2	driver	31	8.5	150	22	variable
	driven	31	8.5	-	22	variable
4.3	driver	31	8.5	variable	22	.002
	driven	63	8.5	-	22	.002
4.4	driver	31	variable	150	22	.002
	driven	31	variable	-	22	.002
4.5	driver	31	8.5	150	22	.002
	driven	variable	8.5	-	22	.002
4.6	driver	31	8.5	150	variable	.002
	driven	63	8.5	-	variable	.002
4.7	driver	31	8.5	150	22	.002
	driven	63	8.5	-	22	.002

Table 2. Compressible Parameter Variations to Assess the Effects on Velocity

Figure Number(s)		Number of Teeth	Diametral Pitch teeth/inch	Pitch-line Velocity ft/s	Pressure Angle Degrees	Backlash inches
4.8	driver	31	8.5	150	22	.002
	driven	31	8.5	-	22	.002
4.9 and 4.10	driver	31	8.5	150	22	variable
	driven	31	8.5	-	22	variable
4.11	driver	31	8.5	150	22	variable
	driven	63	8.5	-	22	variable
4.12, 4.13 4.14, & 4.15	driver	31	8.5	variable	22	.002
	driven	63	8.5	-	22	.002
4.16 and 4.17	driver	31	8.5	150	22	.002
	driven	variable	8.5	-	22	.002
4.18 and 4.19	driver	31	variable	150	22	.002
	driven	31	variable	-	22	.002
4.20	driver	31	variable	150	22	.002
	driven	63	variable	-	22	.002

continued

Table 2. (continued)

Figure Number(s)		Number of Teeth	Diametral Pitch teeth/inch	Pitch-line Velocity ft/s	Pressure Angle Degrees	Backlash inches
4.21	driver	31	8.5	150	variable	.002
	driven	63	8.5	-	variable	.002
4.22	driver	31	8.5	150	22	.002
	driven	31	8.5	-	22	.002
4.23	driver	31	8.5	150	22	.002
	driven	63	8.5	-	22	.002
4.24	driver	31	8.5	150	22	.002
	driven	31	8.5	-	22	.002

Table 3. Geometry Variations for Comparison of Incompressible and Compressible Flow Velocity

Figure Number(s)		Number of Teeth	Diametral Pitch teeth/inch	Pitch-line Velocity ft/s	Pressure Angle Degrees	Backlash inches
4.25	driver	31	8.5	150	22	.002
	driven	31	8.5	-	22	.002
4.26	driver	31	8.5	150	22	.002
	driven	31	8.5	-	22	.002
4.27	driver	31	8.5	150	22	.002
	driven	31	8.5	-	22	.002

were analyzed. Changes were made to these parameters and the corresponding peak velocities were plotted. When examining the effect of the parameters only flow between the teeth was plotted because it represents the most significant flow of fluid and the highest rates. In the compressible flow results, the position at which the flow reached Mach 1 was noted with respect to changes in the design parameters. Also, for compressible flow, examination of the temperature and pressure rises with percentage of mesh angle are shown to give insight to the thermal conditions in the mesh region.

4.2. Incompressible Flow

An example of the fluid velocities attainable for the lubricant using incompressible flow are shown in Figure 4.1. The mesh simulation was done with an identical gear and pinion with 31 teeth and a diametral pitch of 8.5 teeth per inch, a pitch line speed of 150 ft/s, a pressure angle of 22 degrees, and a backlash of .002 inches. The three curves represent flow out the ends, between the teeth, and combined flow. The highest rate occurs for the teeth flow, $\tilde{v} = 30$ corresponding to a velocity of 4500 ft/s, followed by combined, $\tilde{v} = 13$ corresponding to 1950 ft/s, and end flow, $\tilde{v} = 5$ corresponding to 750 ft/s. The peak in velocity is reached at 48% of the total mesh cycle for all three flows. The flow slows to almost zero at 70% of the mesh. The velocity is represented by equation 2.7, $v/r\omega = 1/A \times dV/d\theta$, where A is the discharge area and $dV/d\theta$, is the change in volume with respect to position. From the equation, it is possible to see that smaller discharge areas and higher volume changes give larger velocities. Teeth flow gives the highest velocity rates because it presents the smallest discharge area. The combined area, equation 2.9, is the next smallest area, then finally the end area, equation 2.8, is the largest area of the three. The likely cause of the peak occurring at 48% mesh is the area of discharge has reached its minimum

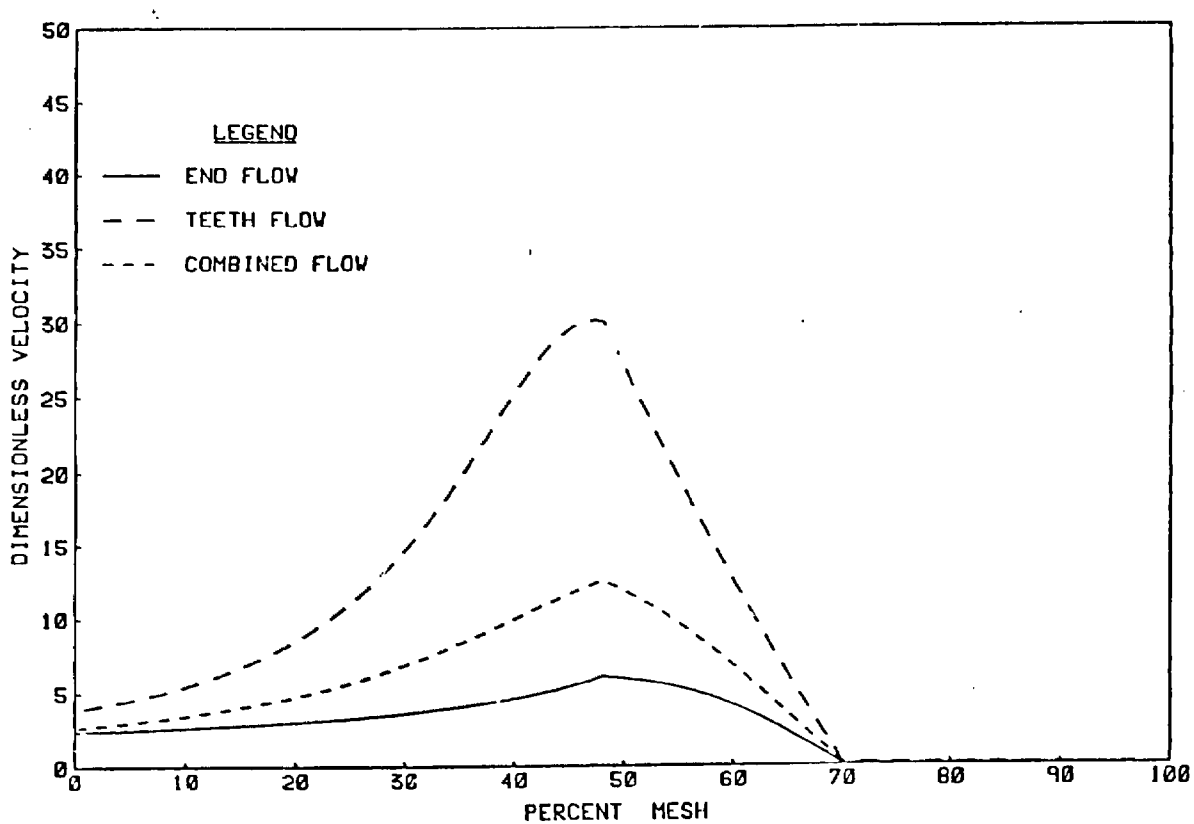

Figure 4.1 Dimensionless velocity for the three flow areas.

value while the rate of volume change continues to decrease. The flow slows to zero near 70% mesh because the change in volume, $dV/d\theta$, has become almost negligible.

The influence of varying the backlash on peak velocity between the teeth values is shown in Figure 4.2. The backlash was varied from .0005 inches to .004 inches using the same gear and pinion at a pitch line speed of 150 ft/s. The backlash value was added to the chord length calculated between the two meshing teeth. The velocity increases with a decrease in backlash. Similar results are obtained for other gear geometries. By assuming no expansion of the gear teeth due to local temperature rises, the flow discharge area between the teeth can be controlled by varying the backlash. Referring to the velocity equation, equation 2.7, it can be seen that as the discharge area decreases, the inverse of the area increases the velocity. If no backlash existed, the discharge area would become very small as the teeth approach contact giving infinitely large velocity before it finally closed and stopped the flow.

A linear curve results for changes in pitch line velocity. A curve of peak velocity values for pitch line speeds ranging from 100 ft/s to 400 ft/s is shown in Figure 4.3. Even at low pitch line speeds of 100 ft/s, incompressible theory predicts high velocities for this geometry. The curve is linear because in the dimensionless velocity equation, equation 2.7, the velocity is only dependant on current geometry values therefore changes in pitch line speed do not affect the dimensionless velocity. Similar results are predicted for other geometries.

The diametral pitch is the number of teeth per inch along the pitch circle. Pitches less than 16 teeth/inch are designated coarse pitch and those greater than 20 teeth/inch are fine pitch. The effect of varying diametral pitch from 8.5 teeth/inch to 24 teeth/inch on the peak velocity of discharged air is shown in Figure 4.4. As the diametral pitch changes from coarse pitch to fine pitch, the

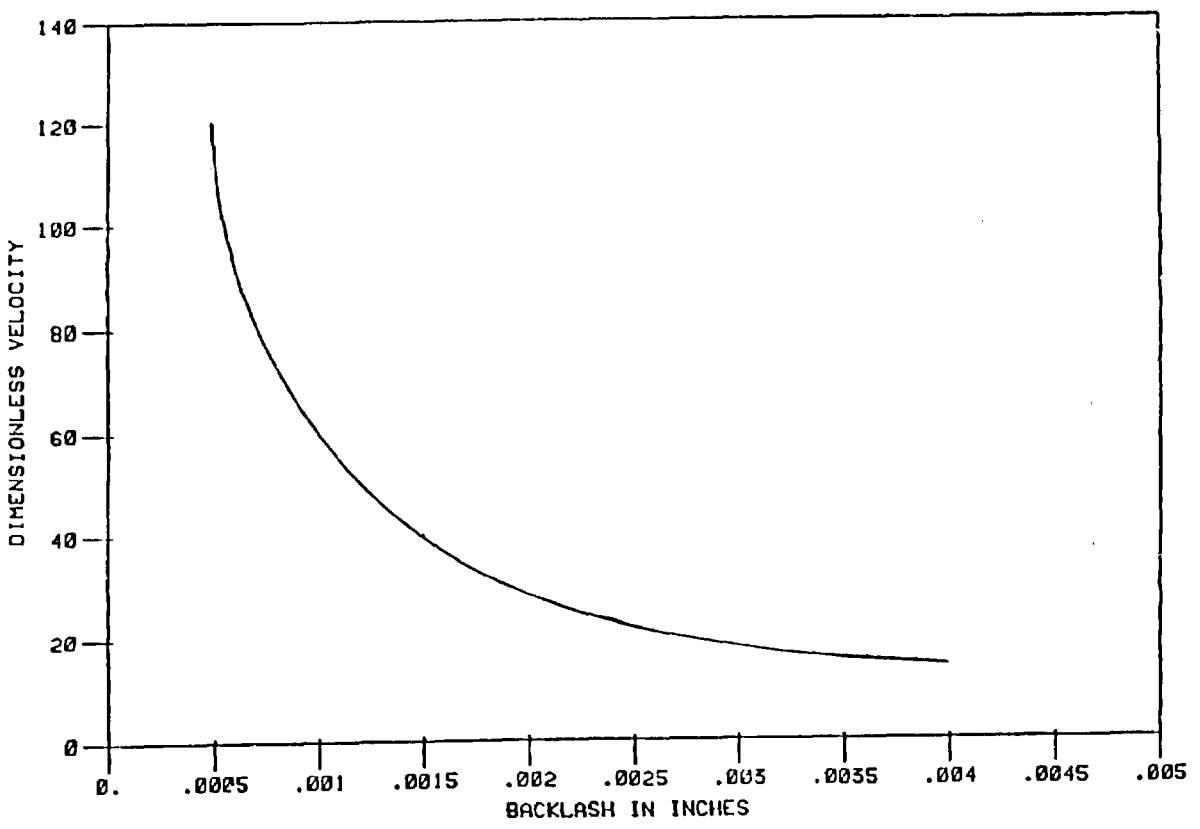

Figure 4.2 Dimensionless velocity as a function of backlash changes.

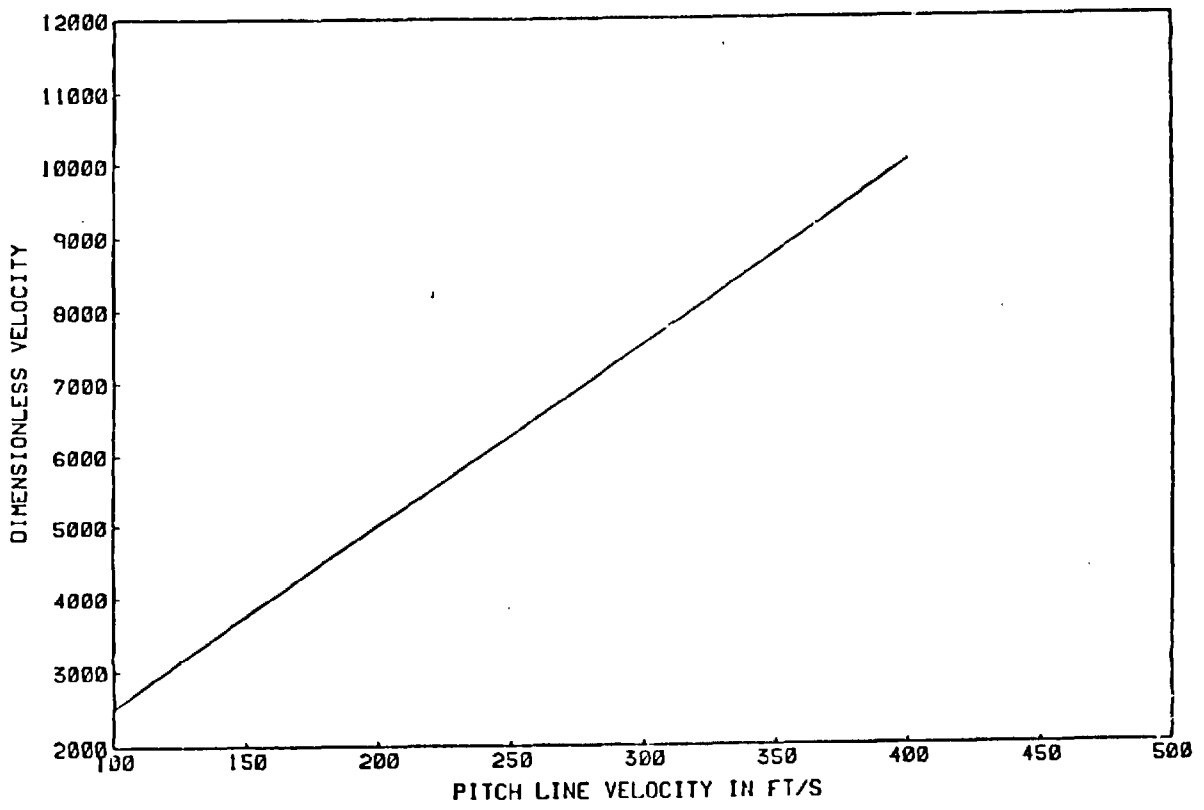

Figure 4.3 Incompressible velocity vs. pitch line velocity.

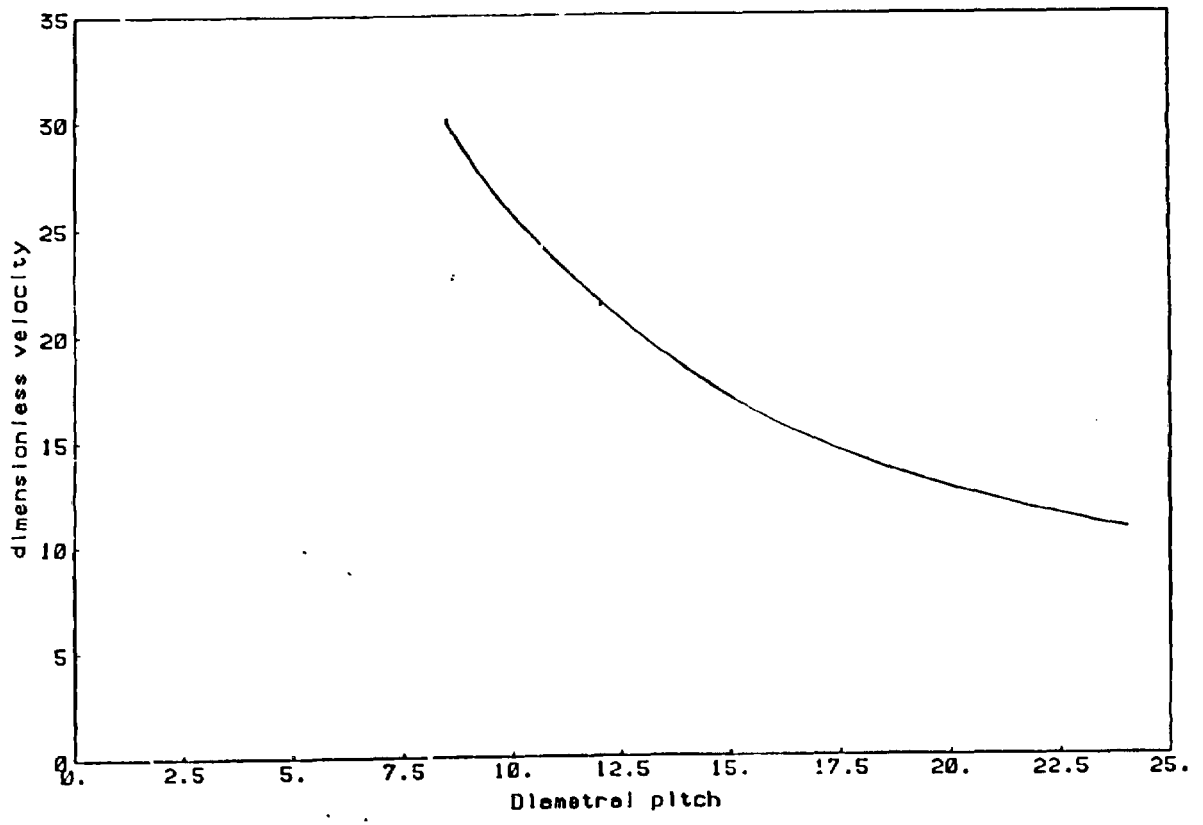

Figure 4.4 The effect of diametral pitch changes on velocity.

velocity decreases. This is a result of the volume change, $dV/d\theta$, being greater for coarse pitch gears. The volume change depends on the size of the meshing tooth entering the space between the teeth. The size of the teeth depends on the inverse of the diametral pitch. The addendum is 1/P and the dedendum is 1.25/P so that a smaller diametral pitch results in larger teeth. Changing the diametral pitch and holding the number of teeth the same does not change the total mesh angle but does change the diameter of the gears. Therefore over the same range of motion a larger tooth causes greater changes in the volume between the teeth for each increment of motion.

By changing the drive ratio between the gear and pinion the effect that the mating gear size has on the fluid velocity can be seen in Figure 4.5. The driving gear had 31 teeth with a diametral pitch of 8.5 teeth/inch, a backlash of .002 inches at a pitch line speed of 150 ft/s. The smaller the drive ratio the higher the air velocity. As the drive ratio increases,(increase the number of mating gear teeth), the total angle of mesh increases. Since the size of the teeth remain constant, for a larger drive ratio the meshing tooth causes smaller changes in volume as it passes through the longer cycle.

The peak velocities for pressure angles 20, 22, and 25 degrees are given in Figure 4.6. Little variation in peak velocity occurs for the three values. This is primarily due to the small change in tooth size. Changing the pressure angle makes the base circle smaller for larger pressure angles. The base circle is given as $r_{base} = r_{pitch} \times cos\phi$ where ϕ is the pressure angle.

Changing the percentage of flow distributed between the teeth and ends is given in Figure 4.7. This change increased the discharge area which slowed the velocity.

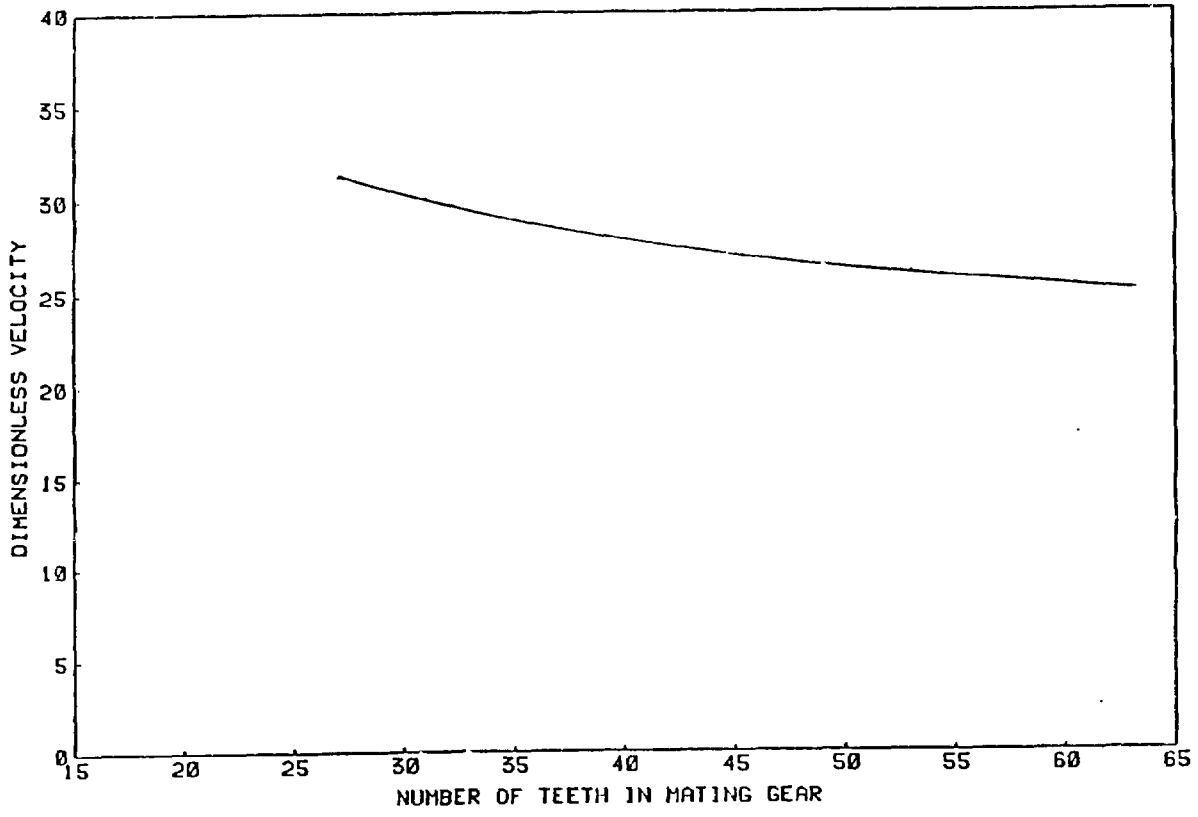

Figure 4.5 The effect of drive ratio changes (number of teeth in the mating gear) on the velocity.

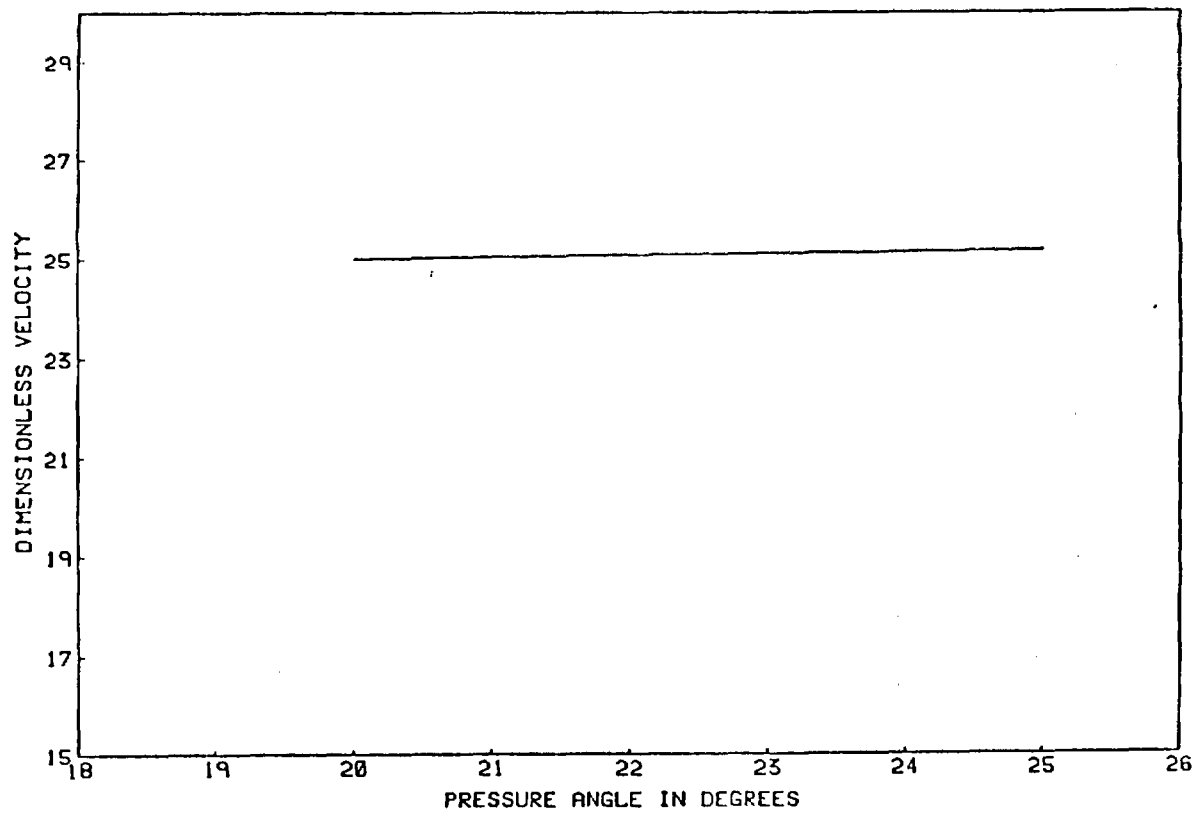

Figure 4.6 Velocity changes due to pressure angle variation.

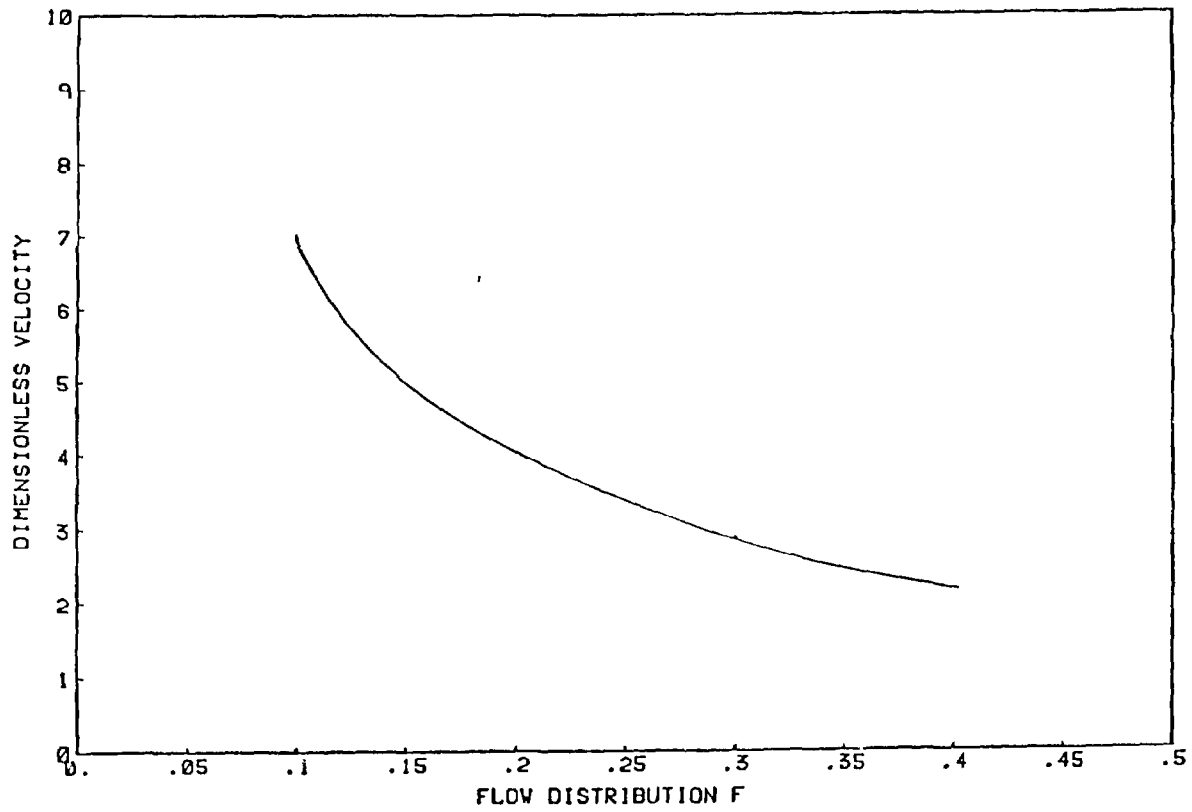

Figure 4.7 Velocity as a function of flow distribution factor, f.

4.3. Compressible Flow

Taking into account the compressibility of air, the meshing action of the gears compressed and pumped out the air trapped between the meshing teeth. An example of the velocities for the three flow areas is given in Figure 4.8. An identical gear and pinion with 31 teeth, 8.5 teeth/inch a backlash of .002 inches were meshed at a pitch line velocity of 150 ft/s. The rate of the three flows gradually increased from zero velocity. The position at which sonic velocities are reached can be seen by the abrupt change in the velocity curve. The flow between the teeth was the first to reach Mach 1 at 35% of the mesh cycle. The combined flow eventually reached Mach 1 at 47% of the mesh cycle and the endflow did not reach Mach 1. The flow between the teeth gives the highest velocity, $\tilde{v} = 8.3$ which corresponds to 1245 ft/s, followed by combined flow, $\tilde{v} = 8$ which corresponds to 1200 ft/s, and end flow, $\tilde{v} = 6$ which corresponds to 900 ft/s. As the mesh begins, the pressure change inside the tooth space increases. Once Mach 1 is reached, the flow is choked and remains at Mach 1. Any changes in velocity are due to a local temperature rise. The difference in flow velocity between the three assumed areas can be attributed to the difference in discharge areas. A wide set of gears would have the highest velocities because the flow tends to move out between the teeth instead of the ends.

For the same set of gears and a pitch line speed of 150 ft/s, the effect of changing the backlash from .0005 inches to .004 inches is shown in Figure 4.9. Figure 4.10 gives the percent of mesh when the air velocity reaches sonic levels. As expected, the smaller backlash allows the velocity to reach sonic levels sooner. Changing the driven gear to 63 teeth and keeping the pitch line velocity at 150 ft/s results in subsonic flow throughout the mesh cycle. Figure 4.11 gives subsonic results for changing backlash. The effects for compressible flow are not

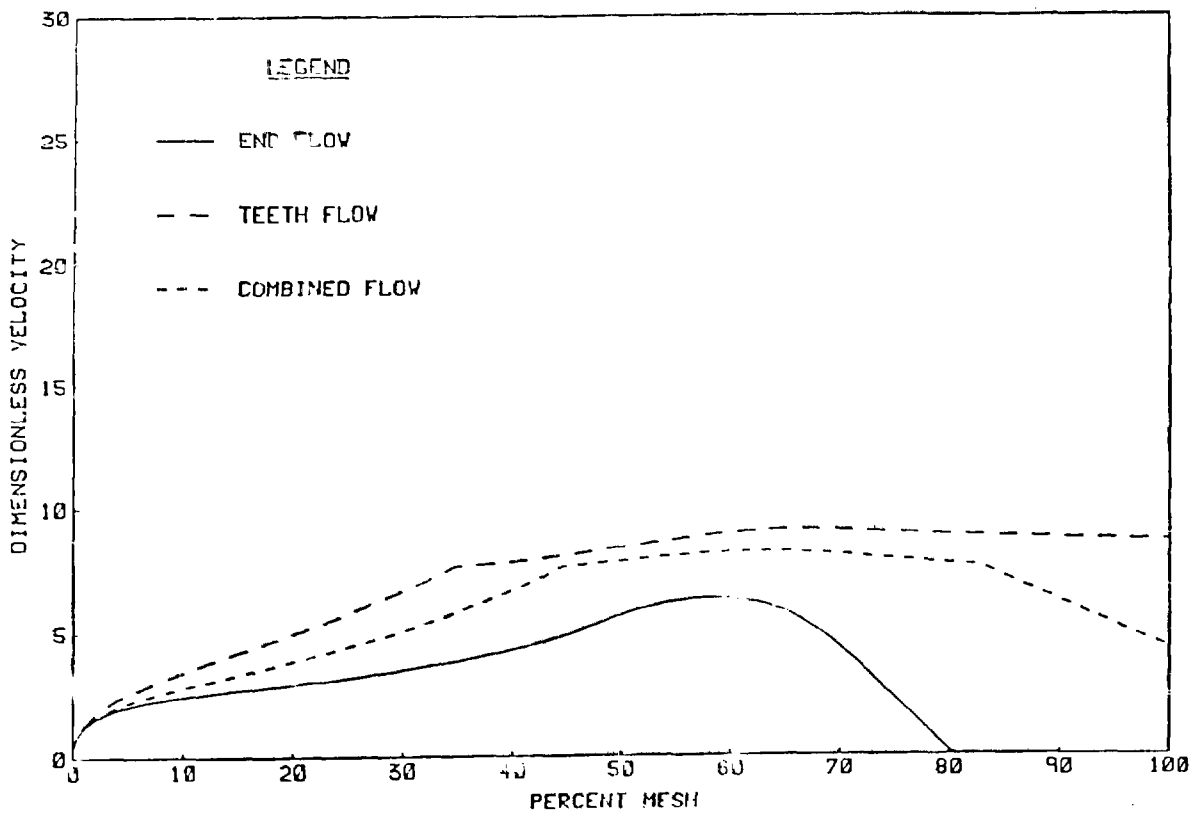

Figure 4.8 Dimensionless velocity for the three flow areas.

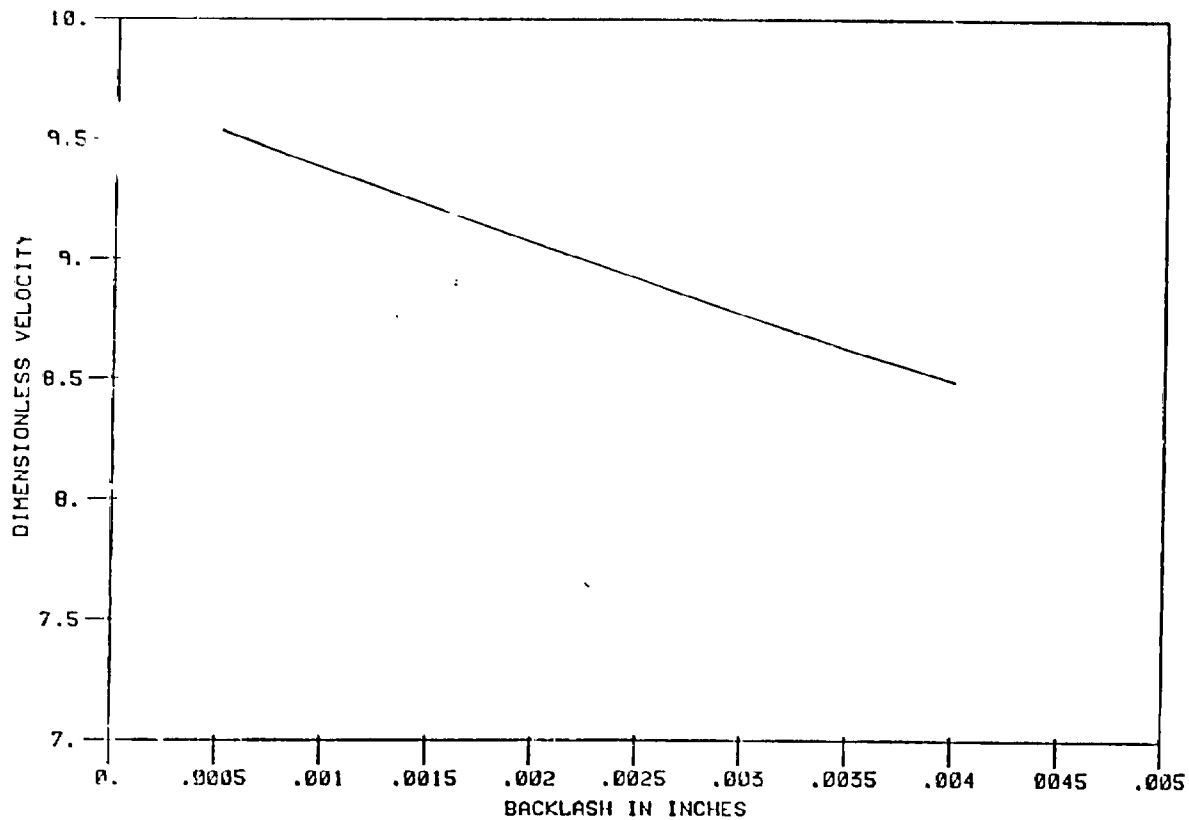

Figure 4.9 Peak velocity for backlash variation.

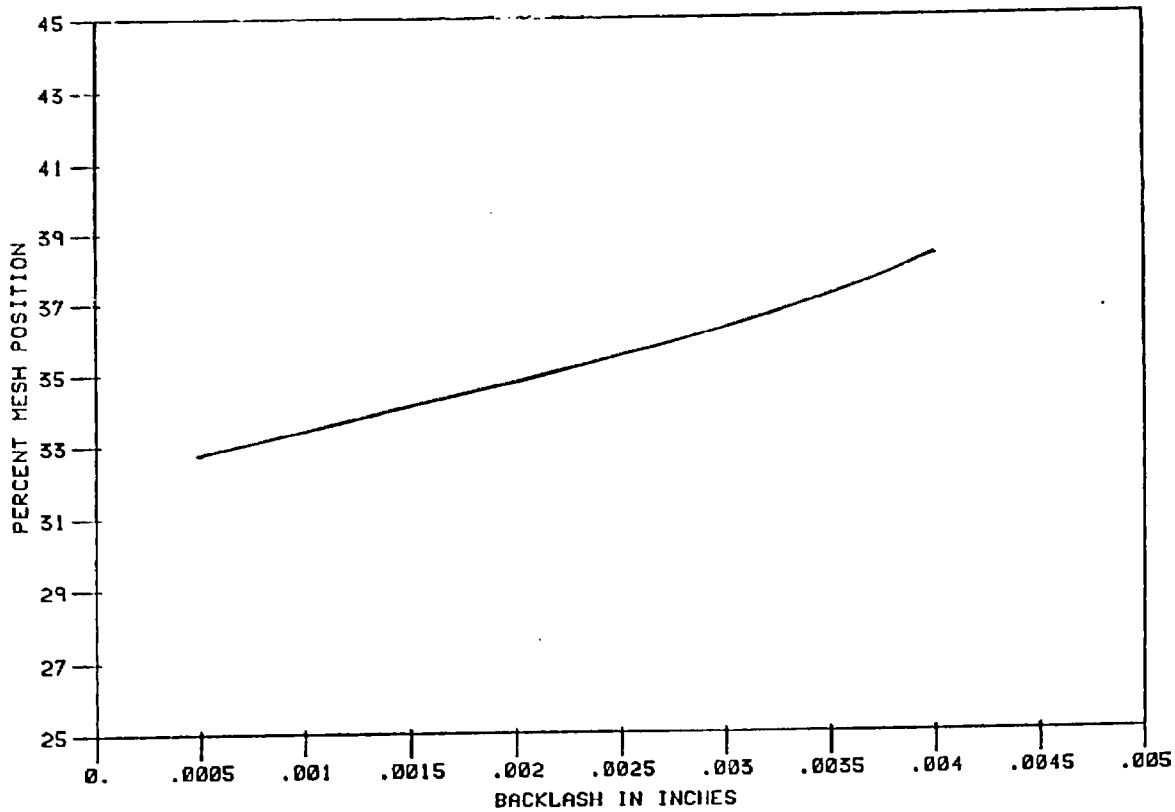

Figure 4.10 Position Mach 1 is reached for backlash changes.

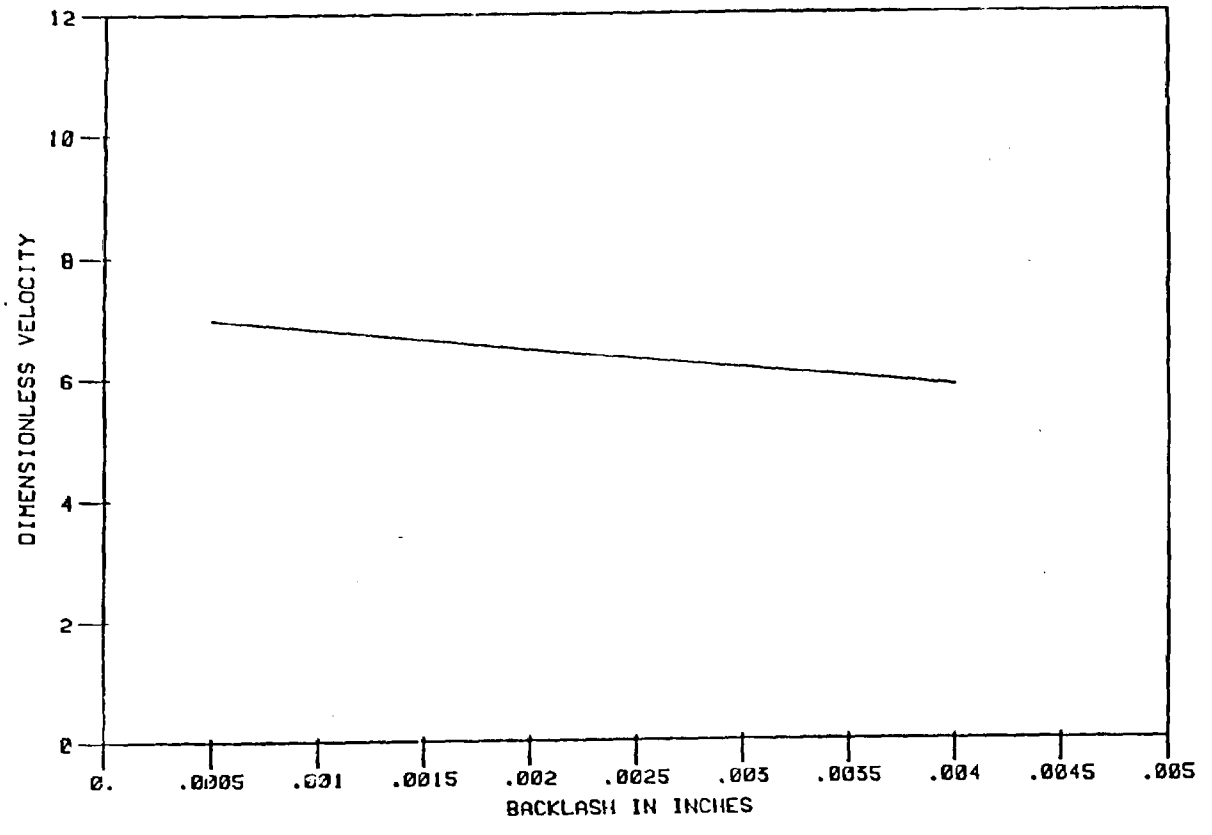

Figure 4.11 Subsonic velocity due to backlash variation.

as dramatic as the incompressible results, Figure 4.2, this is due to one part of the pressure term, $P/V\ dV/d\theta$, being more dominant in equation 3.16.

For a 31 teeth driver and a 63 teeth driven gear with a diametral pitch of 8.5 teeth/inch, the geometry does not produce sonic velocity levels for changes in pitch line velocity. The effect is seen in Figure 4.12. As the pitch line velocity increases, the resulting velocity and begins to level off near 1100 ft/s for pitch line velocities greater than 350 ft/s. The non linear response of the peak velocity is due to the non-linear pressure rise and the $\frac{1}{2}$ power in the velocity equation. A sonic case is given in Figure 4.13, the corresponding position at which sonic was reached is in Figure 4.14. The pressure rise is seen in Figure 4.15. From the pressure curve, it can be seen that the velocity follows the same form.

The effect of varying the drive ratio by changing the number of teeth in the driven gear is shown in Figure 4.16. For large drive ratios, the air velocity is slower. The effect of drive ratio on the position (% mesh) when the air reaches sonic is given in Figure 4.17. The effect is primarily due to the longer approach associated with a larger drive ratio. The longer approach reduces the volume changes with respect to position.

Fixing the number of teeth at 31 and changing the diametral pitch from 8.5 teeth/inch to 24 teeth/inch gave the velocities shown in Figure 4.18. The effect of changing the diametral pitch on position sonic is given in Figure 4.19. The smaller the diametral pitch the sooner it reaches sonic. Subsonic geometry results for changing diametral pitch are shown in Figure 4.20. When keeping the number of teeth constant, the diametral pitch does not change the total angle of approach, but does change the diameter of the gear. This means that for the same angle of approach the difference in velocities is primarily due to the change in the volume with respect to position, $dV/d\theta$. The major factor affecting the change in volume is the size of the meshing tooth. The tooth size varies inversely

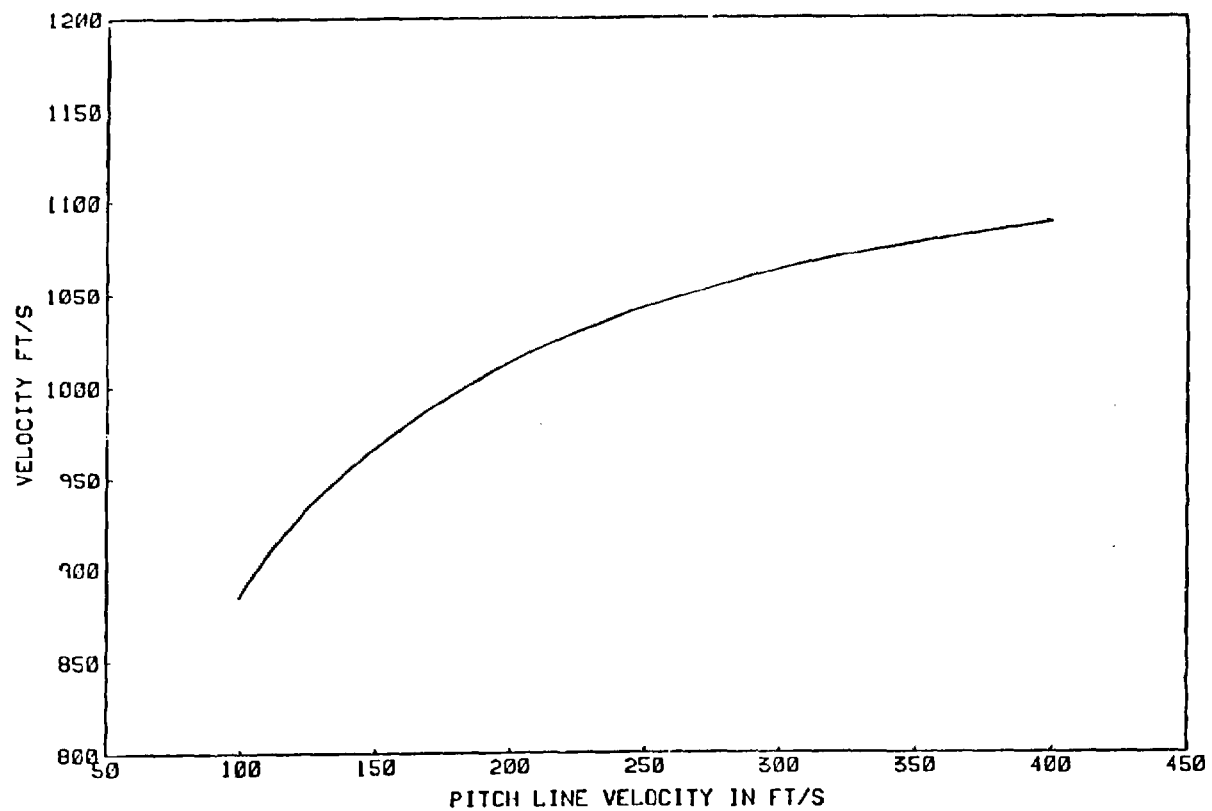

Figure 4.12 Subsonic velocity for pitch line changes.

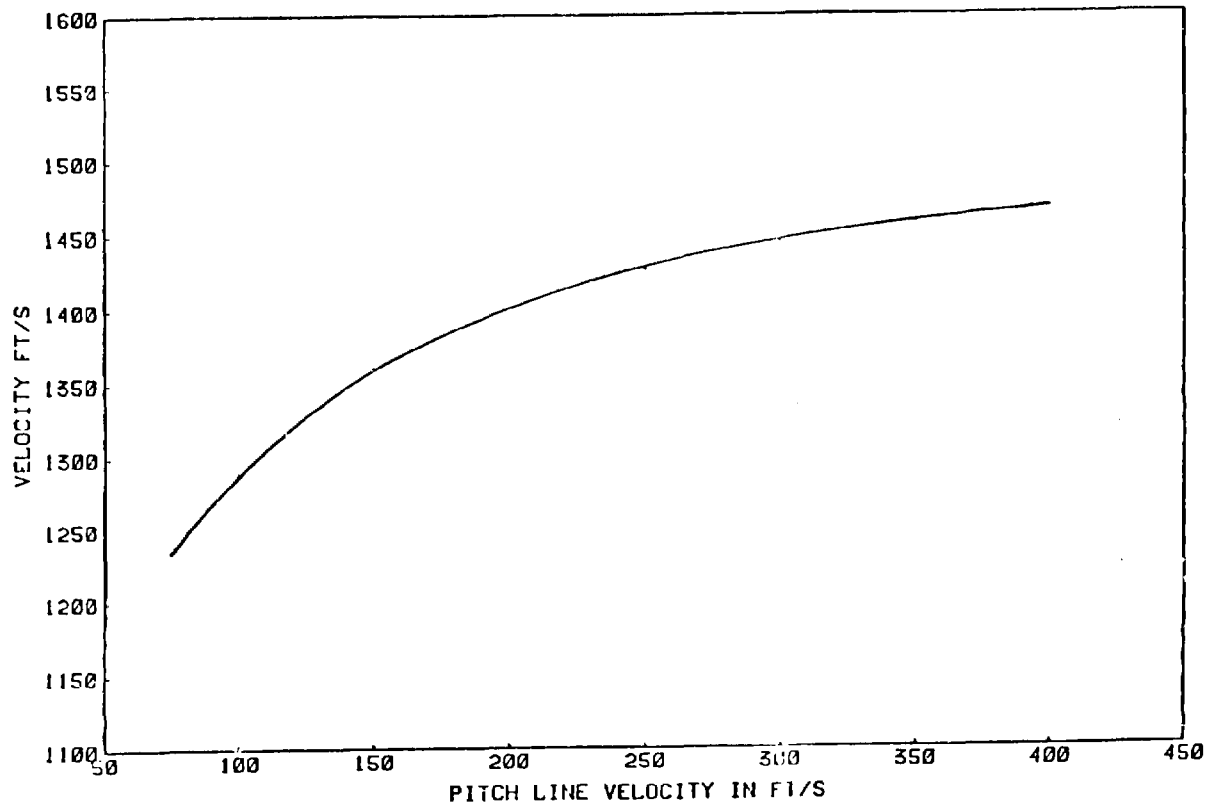

Figure 4.13 Sonic velocity for pitch line changes.

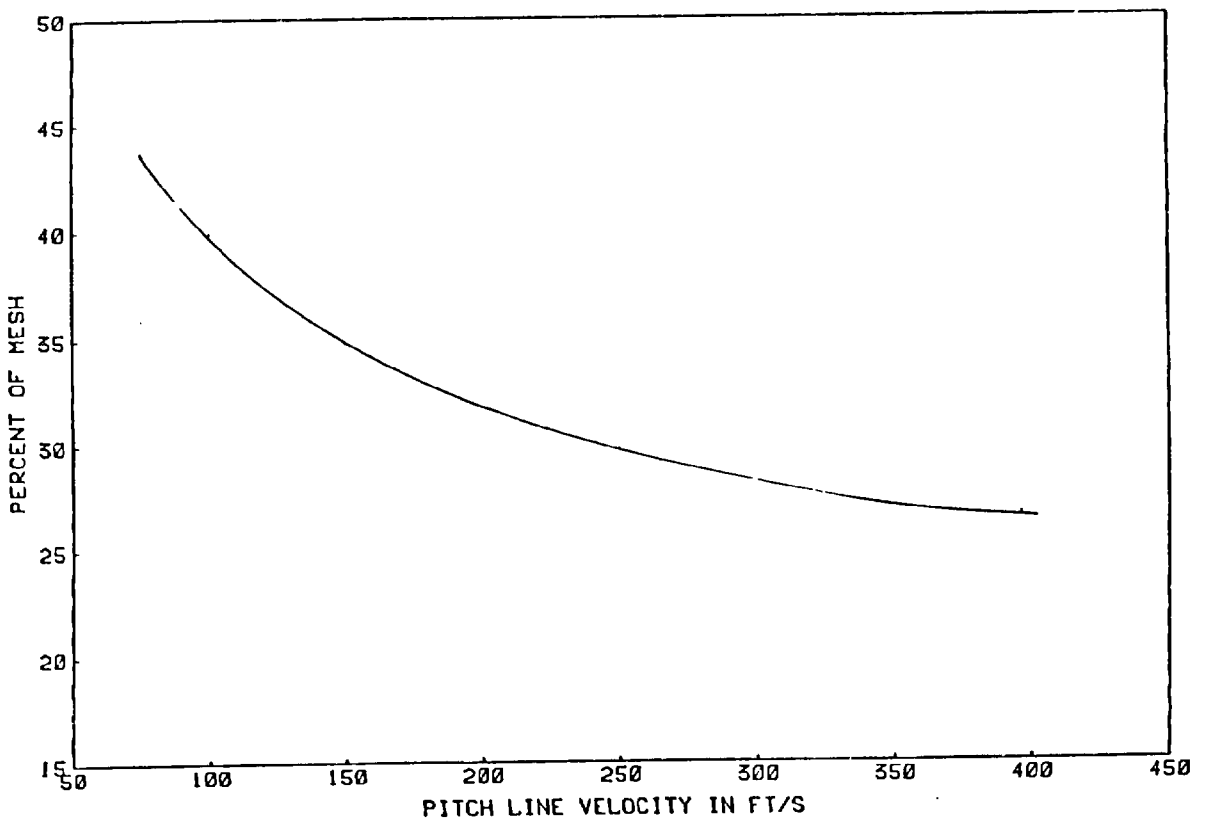

Figure 4.14 Mesh position at which Mach 1 is reached for pitch line changes.

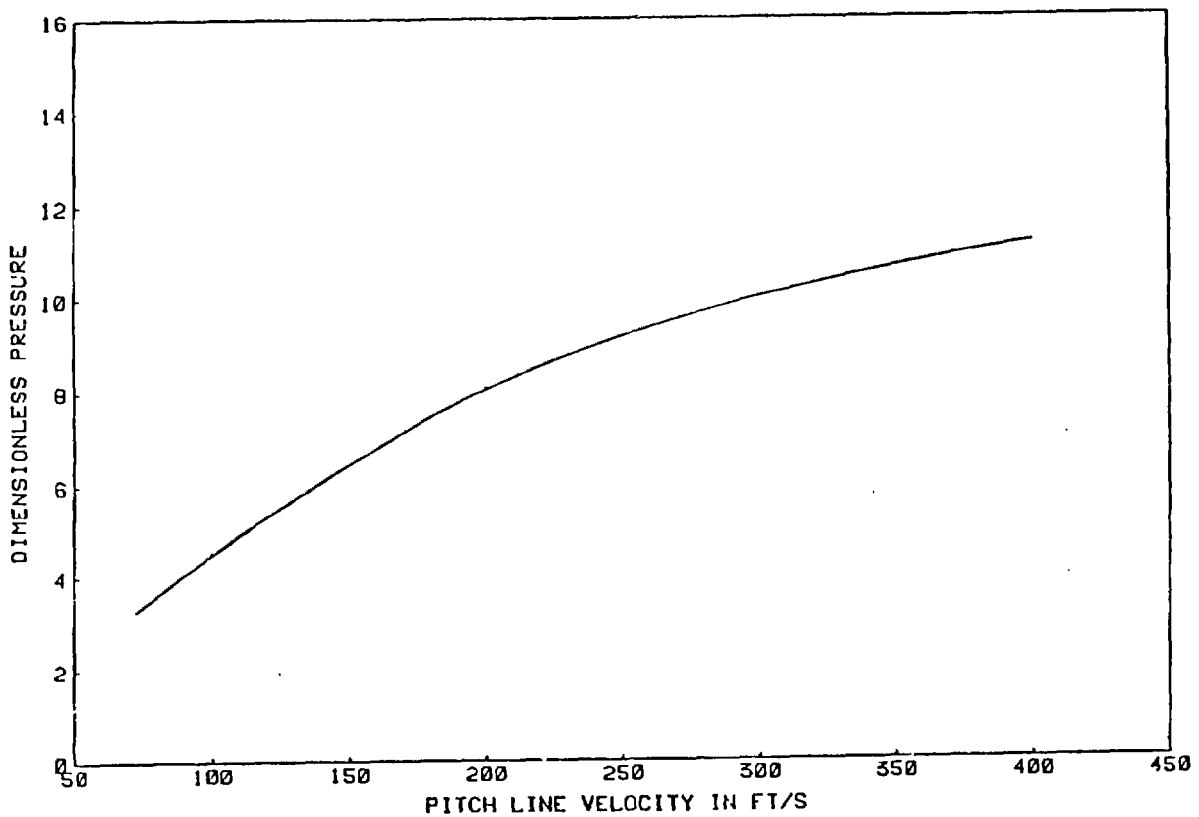

Figure 4.15 Dimensionless pressure for pitch line changes.

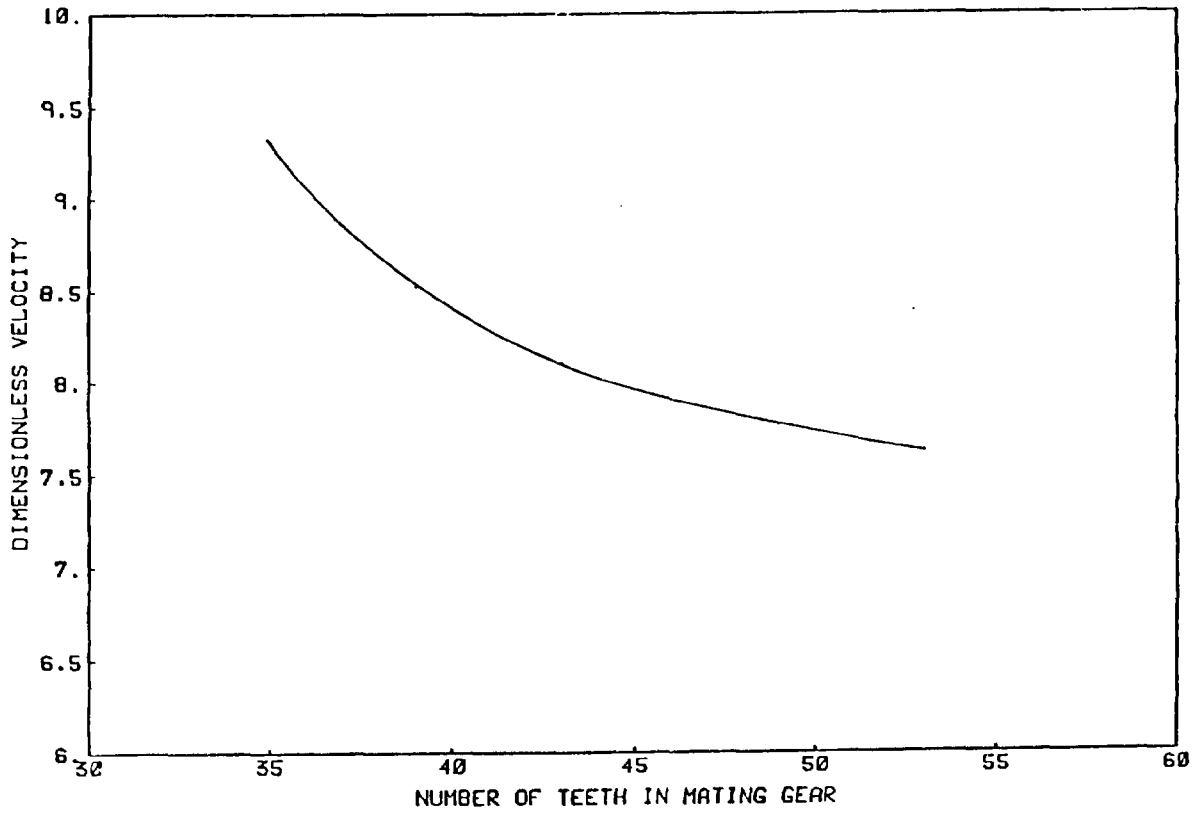

Figure 4.16 Peak velocity due to drive ratio changes (changes in the number of driven pinion teeth).

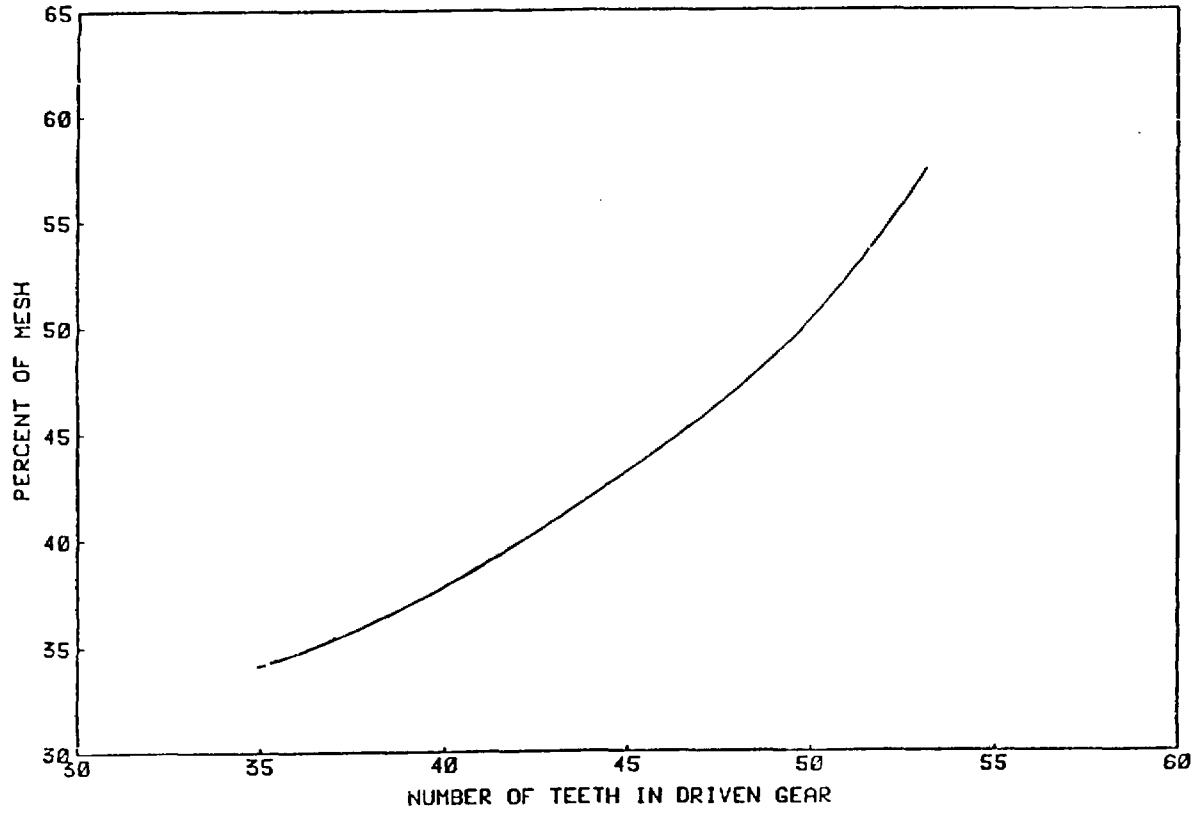

Figure 4.17 Position at which Mach 1 is reached for drive ratio changes (changes in the number of driven pinion teeth).

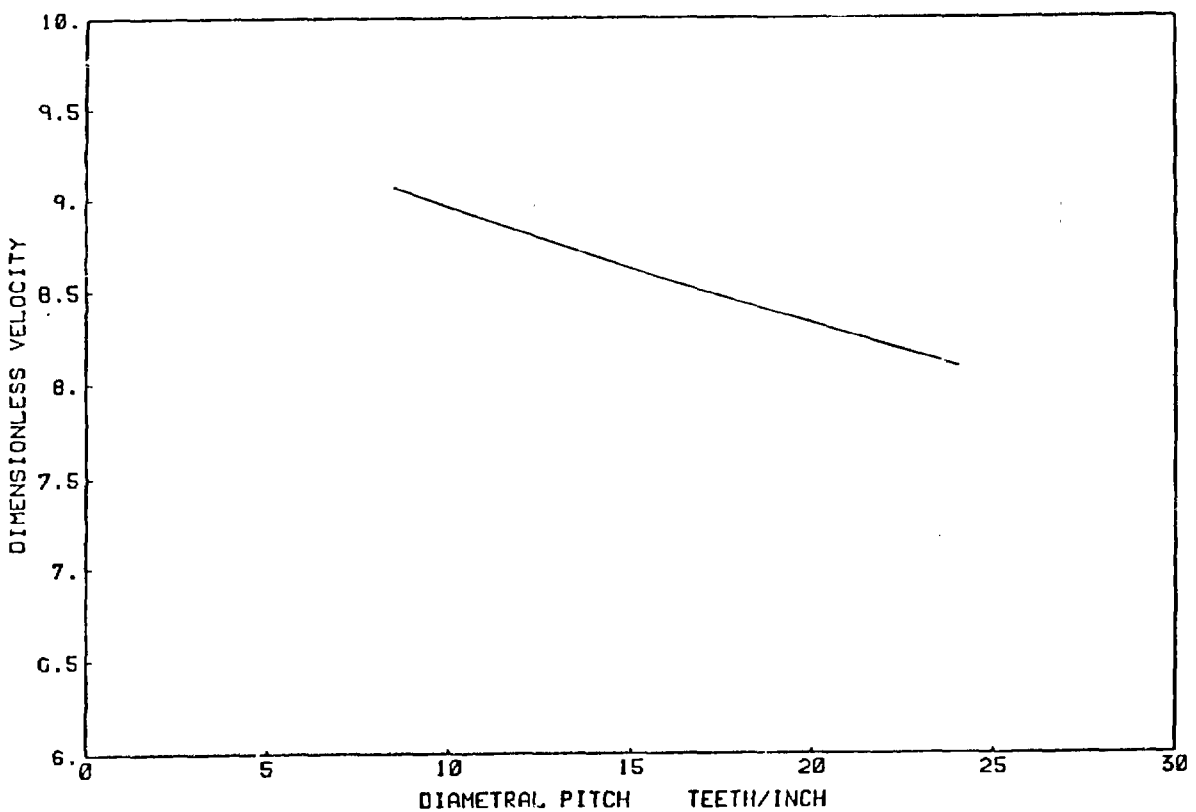

Figure 4.18 The effect diametral pitch has on peak velocity.

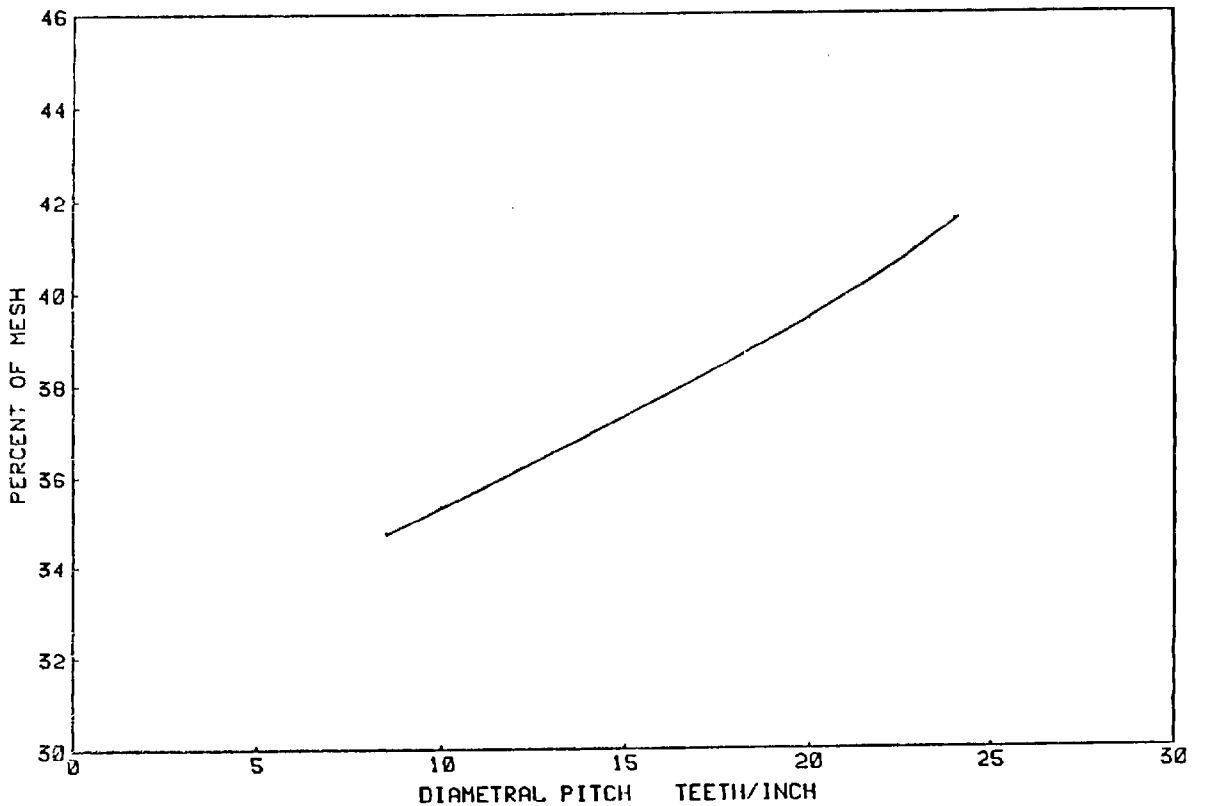

Figure 4.19 The position at which Mach 1 is reached for diametral pitch changes.

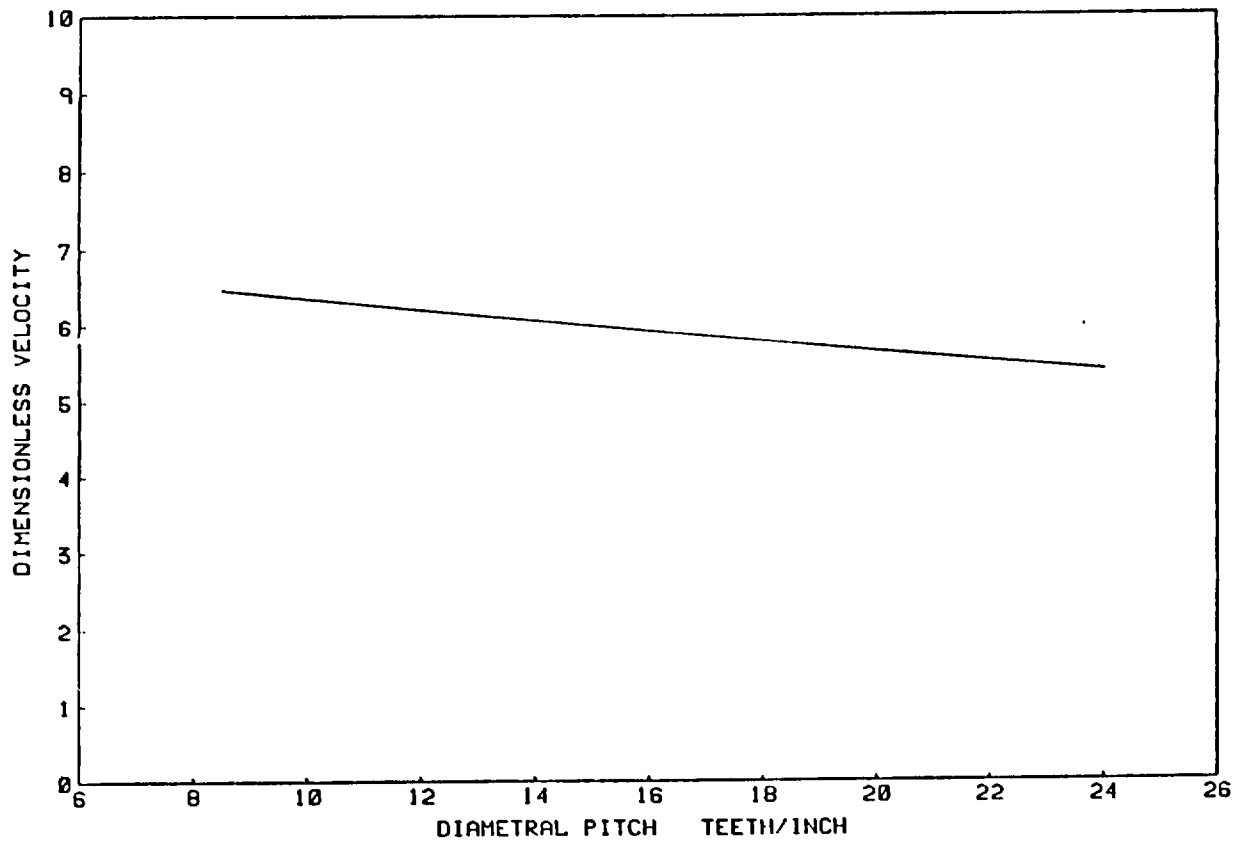

Figure 4.20 Subsonic velocity for diametral pitch changes.

with the diametral pitch. Smaller diametral pitches result in larger teeth which cause greater changes in volume for each incremental step.

The effect of changing the pressure angle from 20 to 22 and then 25 degrees gives the result in Figure 4.21. A slight variation occurs due to the small change in tooth size for changing pressure angle.

A typical pressure variation for the three flows, end, teeth and combined, is given in Figure 4.22. The pressure peaks correspond to the peak velocity position.

Changing the flow distribution by making the endflow area account for a larger percentage of the total discharge area is given in Figure 4.23. As expected, as greater percentages of the end area are added the discharge area increases and results in a decrease in peak velocity.

The temperature changes inside the meshing region of the teeth for the three flow areas is seen in Figure 4.24. Starting at the ambient temperature, 80 F, the end flow temperature problem rises to 150 F, the teeth flow to 350 F, and the combined flow problem to 220 F. The energy generated must be dissipated. A portion of the energy is dissipated in the air-oil mix and the other portion is absorbed by the gear teeth. If too much energy is absorbed by the teeth thermal distortion results.

4.4. Comparison of Incompressible and Compressible Flow

Using identical gear and pinion of 31 teeth and 8.5 teeth/inch diametral pitch, the velocities for incompressible and compressible flow were compared for each of the assumed discharge flow areas at a pitch line speed of 150 ft/s.

Comparing the end flow in Figure 4.25, the incompressible reaches its peak at 48% of the mesh cycle. The compressible flow case reaches a peak at approximately 60 % of the mesh cycle while both have approximately the same

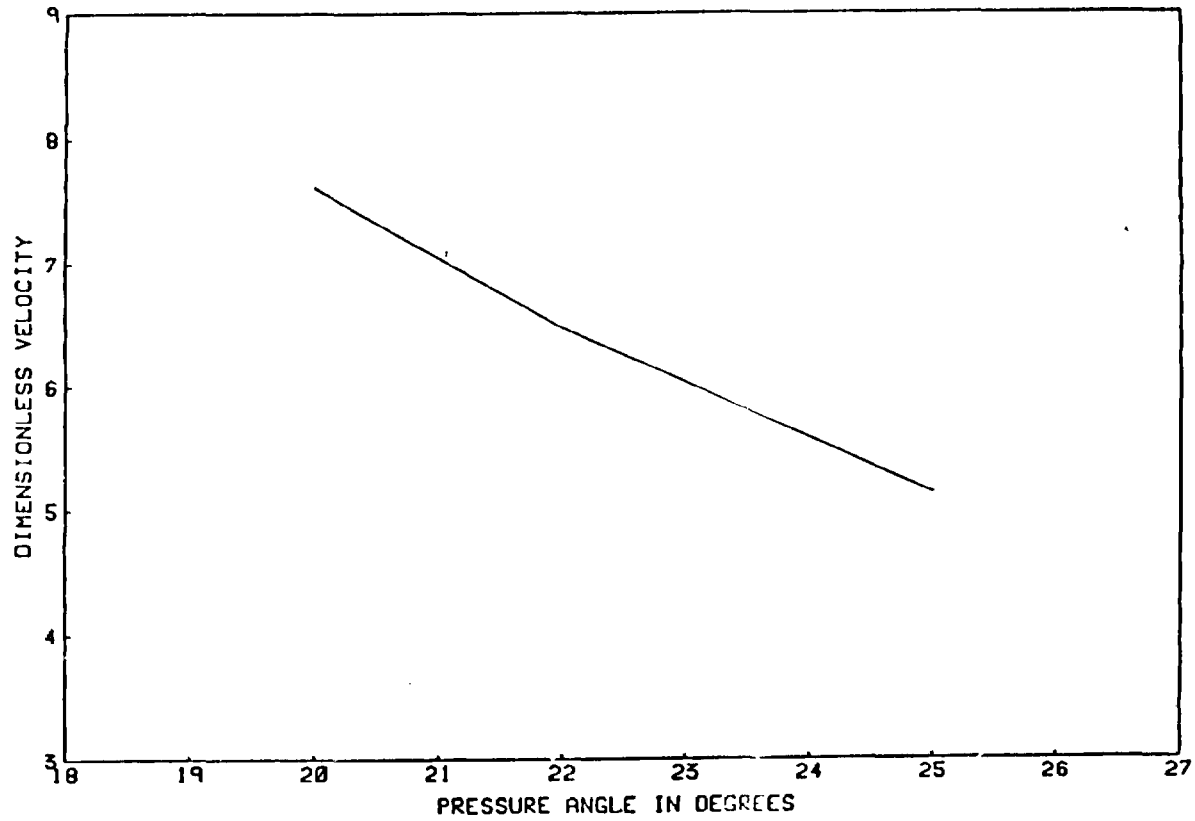

Figure 4.21 Velocity for pressure angle variation.

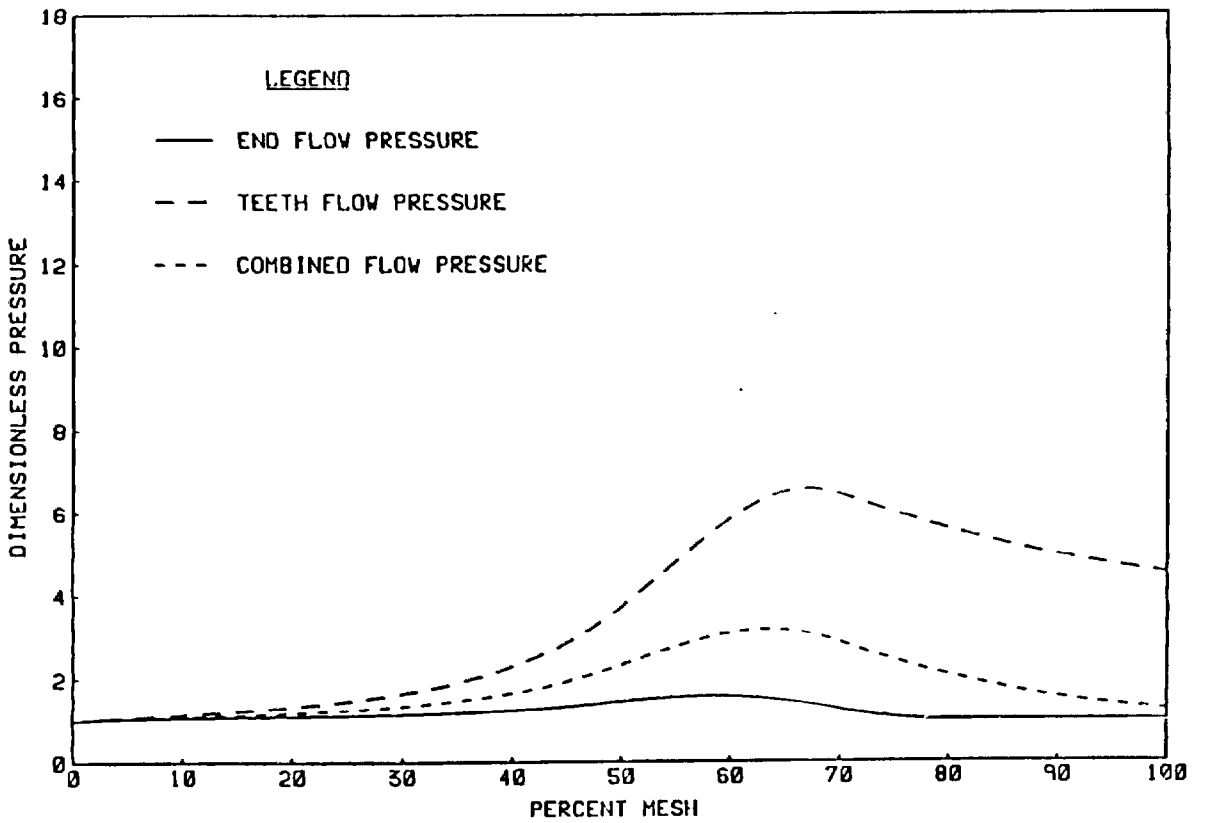

Figure 4.22 Dimensionless pressure in the mesh region for the three flow areas.

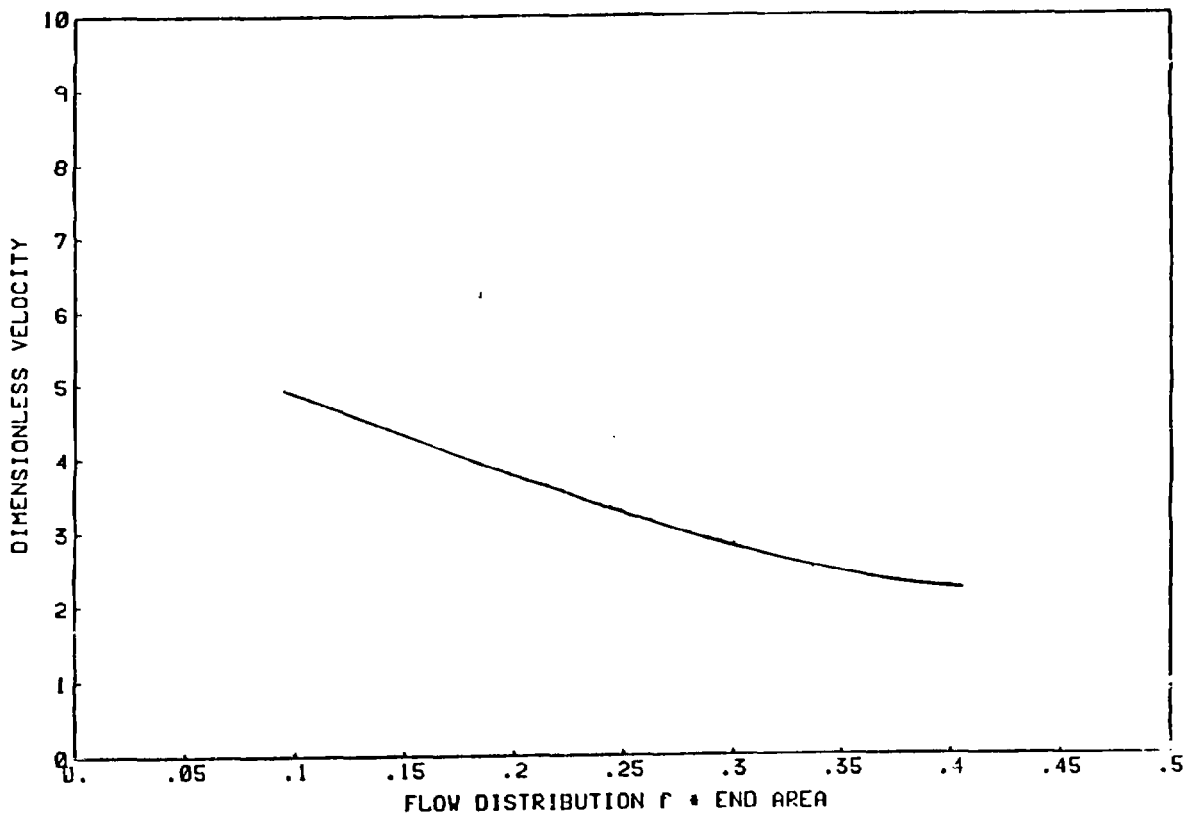

Figure 4.23 The effect of flow distribution variation on peak velocity.

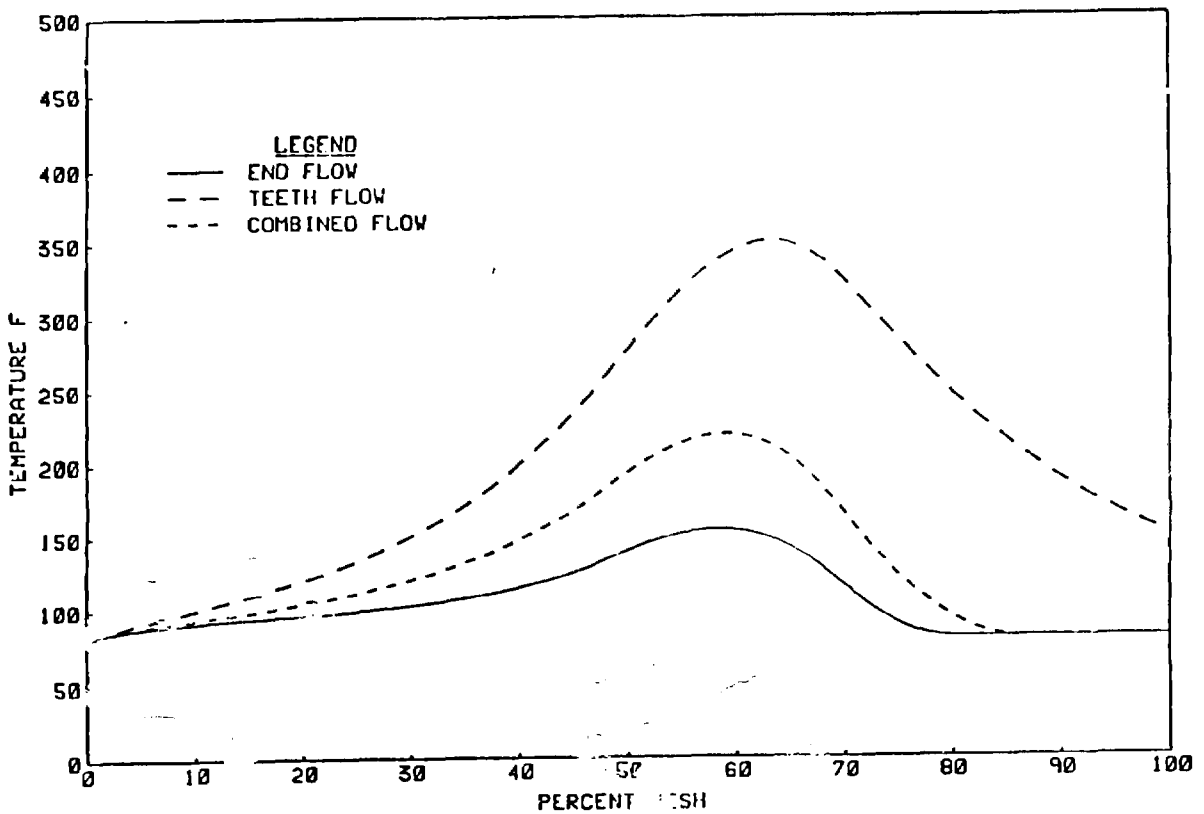

Figure 4.24 Temperature in Fahrenheit in the mesh region for the three flow areas.

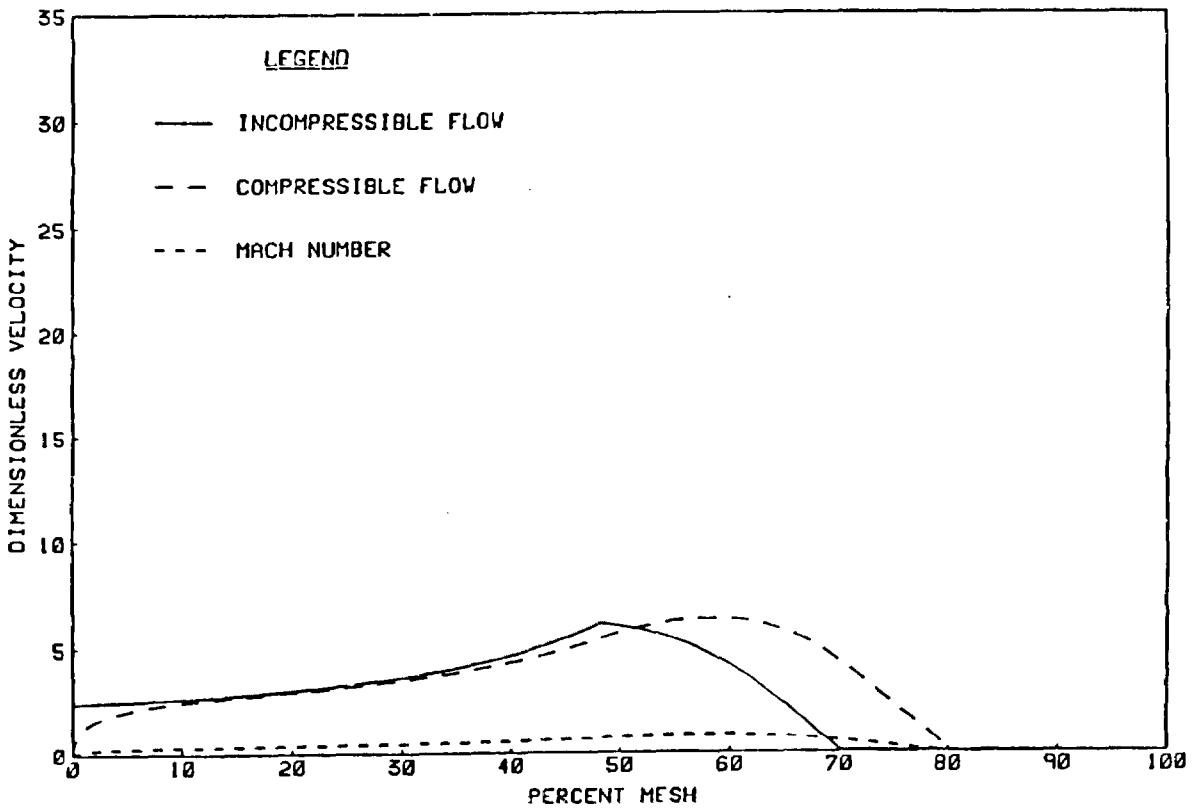

Figure 4.25 Comparison of incompressible and compressible end flow.

peak value. The delay in the compressible peak occurs because of the compressing of the air and the gradual rise in pressure. Comparing the flow between the teeth, Figure 4.26, the incompressible peaks at $\tilde{v} = 30$ and the compressible reaches Mach 1 at 35 % of the mesh cycle. A direct comparison of peak velocities for incompressible and compressible flow is not meaningful because once the compressible velocity reaches Mach 1 it is choked and remains at Mach 1.

Comparing the combined flow in Figure 4.27 the incompressible is again higher and the compressible reaches sonic levels at 43 degrees.

4.5. Conclusions

A one-dimensional approximation of the air oil flow resulting from the meshing of spur gear teeth indicates the velocity reaches high rates. Incompressible theory predicts oil velocities as high as 4500 ft/s depending on the pitch line speed. Using compressible flow theory, some geometries produce air velocities high enough to approach and reach the speed of sound, Mach 1, at the exit plane. If the velocity reaches Mach 1, the conditions may lead to the formation of a shock wave downstream of the exit plane. Should a shock wave form, noise is emanated which contributes to the overall noise of the gear mesh.

Since the velocities were shown to depend on a number of different design parameters—diametral pitch, backlash, pitch line velocity, pressure angle, drive ratio, and face width—further analysis should be conducted to quantify their exact effect. This thesis has shown the parameters most significantly affecting the air velocity appear to be the drive ratio and the face width.

Further considerations of this problem should include an experimental analysis of the fluid flow. Also, an expansion of the analytical portion of the problem should include two and three dimensions to determine the flow pattern for different width gears. The inclusion of the effects two rotating teeth have on

the velocity, the effect of the moving exit plane, and a mixture of air-oil mist velocity would make the problem closer to the actual system.

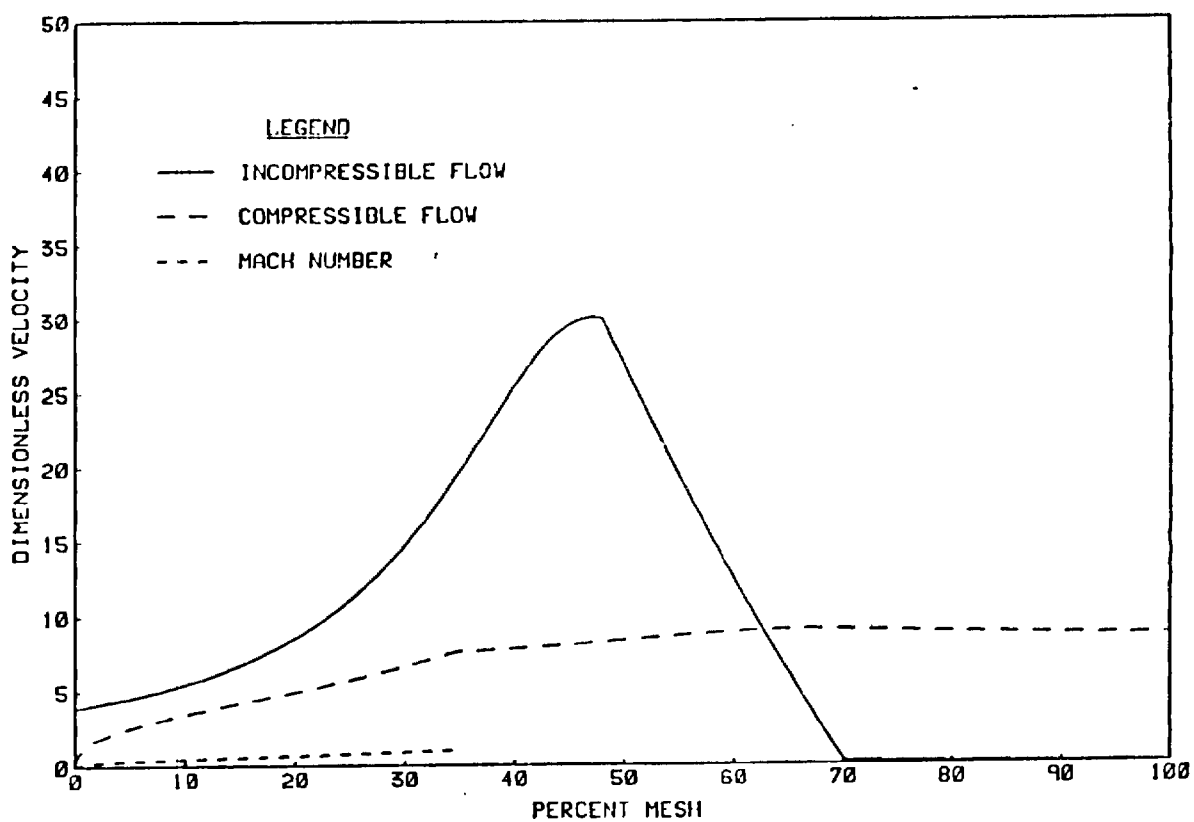

Figure 4.26 Comparison of incompressible and compressible teeth flow.

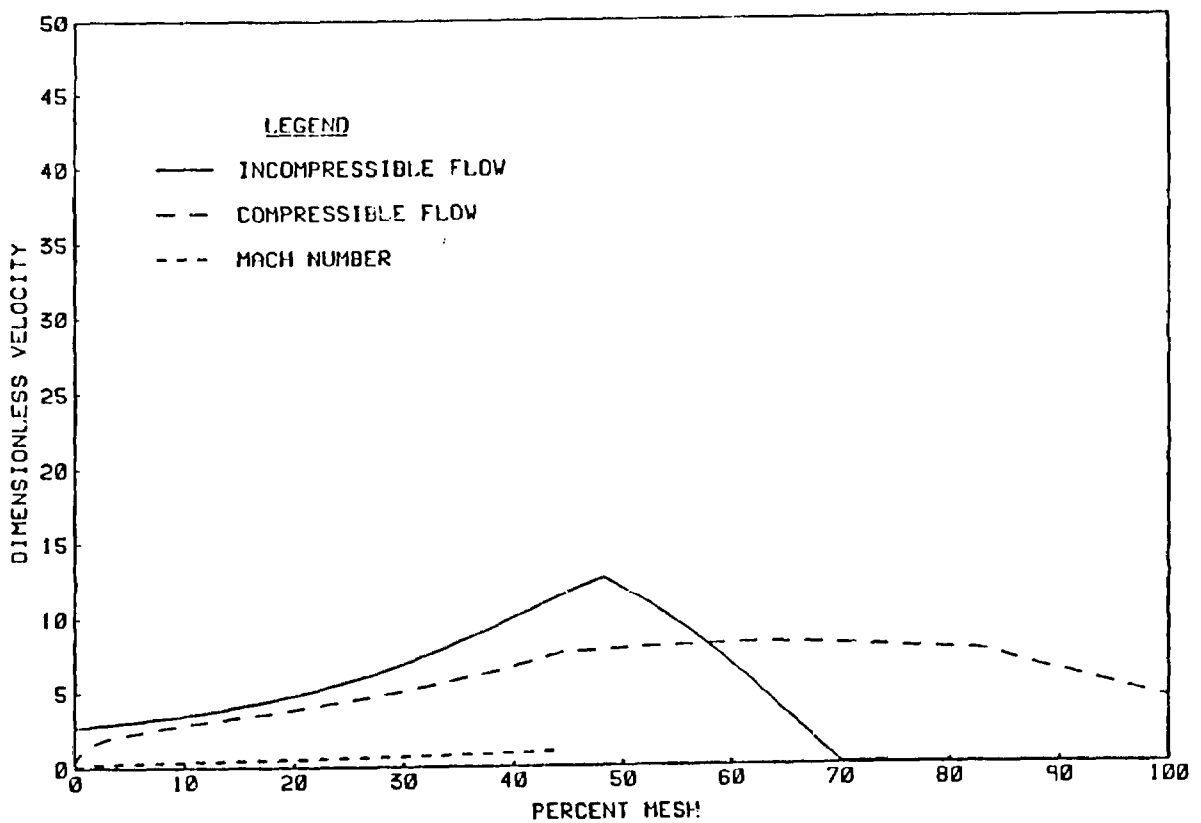

Figure 4.27 Comparison of incompressible and compressible combined flow.

BIBLIOGRAPHY

References

[1] Raymond J. Drago, "Gear System Design for Minimum Noise," unpublished notes.

[2] Kenjiro Ishida and Takashi Matsuda, "Study on Pitch Circle Impulse Noise of Gear by Simulated Gear Tooth Contact", ASME Paper No. 80-C2/DET-69 (1980).

[3] Kenjiro Ishida and Takashi Matsuda, "Effect of Tooth Surface Roughness on Gear Noise and Gear Noise Transmitting Path", ASME Paper No. 80-C2/DET-69 (1980).

[4] Hiroki Fukama, Toyoaki Furukawa, and Toshio Aida, "Fundamental Research on Gear Noise and Vibration" Bulletin of the JSME, Vol. 16, No. 97, Jul., 1973.

[5] Robert H. Badgley, "Mechanical Aspects of Gear-Induced Noise in Complete Power Train Systems," ASME 70-WA/DGP-1 (1970).

[6] Irving Laskin, "Prediction of Gear Noise from Design Data", AGMA 299.03 October, 1968.

[7] M. Wm. Rosen, "The Noises of Two Spur-Gear Transmissions" NOTS TP 2293 NAVORD REPORT 6569 July 27, 1959.

[8] Darle W. Dudley, Handbook of Practical Gear Design. McGraw-Hill Book Company, New York, New York (1984).

[9] Earle Buckingham, Manual of Gear Design Section Two, Machinery, New York, New York (1935).

[10] J. Derek Smith, Gears and Their Vibration, The MacMillan Press LTD, New York, New York (1983).

[11] Joseph Edward Shigley, Kinematic Analysis of Mechanisms (Second Ed.). McGraw-Hill Book Company, New York, New York (1969).

[12] Thomas D. Rossing, The Science of Sound, Addison-Wesley Publishing Company (1982).

[13] Peter A. Franken, "Jet Noise" In: Noise Reduction, edited by Leo L. Beranek, McGraw-Hill Book Company, New York, New York, (1960) pp. 644-666.

[14] Ascher H. Shapiro, Compressible Fluid Flow Parts I and II from Volume I The Ronald Press Company, New York, New York (1958).

[15] Robert W. Hornbeck, Numerical Methods, New York, New York. Quantum Publishers (1975).

BIBLIOGRAPHY (continued)

Other Works Consulted

Benjamin W. Dambly and Edward D. Lawler, "Investigation of Centrifugal Compressor Gear Noise as Influenced by Gear Geometry", ASME Paper No. 69-WA/FE-15 (1969).

Michael J. Katz, Elements of the Scientific Paper, Yale University Press, New Haven, CT (1985) .

Teruo Masuda, Toru Abe, and Kanji Hattori, "Prediction Method of Gear Noise Considering the Influence of the Tooth Flank Finishing Method" ASME Paper No. 85-DET-40 (1985).

"The Involute Curve and Involute Gearing," The Fellows Corporation Springfield, Vermont (1978).

APPENDIX

COMPUTER ALGORITHM GUIDE AND A FLOW CHART

1. PROGRAM EXPLANATION

The computer algorithm approximates the velocity for flow between meshing gear teeth by assuming incompressible and compressible flow theories. For each case, three flow areas were used: end flow, teeth flow, and combined flow. The program was written in Fortran 77 on the Data General Eclipse system. It is run interactively by specifying the data file and the output listfile.

2. MAIN PROGRAM

The main program reads and echoes the input information. The driven teeth were considered the pinion and the gear was the driver. The first subroutine called is SUBROUTINE GEOCAL, which computes the gear and pinion geometry. For the chosen set of gear geometries, the intial contact (starting position gear tooth centerline) is computed. The centerline position is incremented in a DO LOOP by the chosen step size. The program stops when full mesh position is reached.

The subroutine to compute the incompressible velocity is SUBROUTINE INCOMPRESSIBLE. The value for the gear centerline position, its absolute value, and the step size is transferred to the subroutine. Values for the three flow area velocities are returned.

For compressible flow computations, SUBROUTINE COMPRESSIBLE is called to compute the pressure, velocity, temperature, and Mach # for each of the three flow areas. The position of the gear centerline and the size of the step are sent into the subroutine.

The computed values are written to the listfile (default unit=12) at the desired frequency controlled through the input file. The position at which Mach 1 is reached is also written onto the listfile.

3. SUBROUTINE AREA

This subroutine is called by SUBROUTINES INCOMPRESSIBLE and COMPRESSIBLE, it computes the area between the meshing teeth, AIR2, by first determining the chord length between the teeth, CHORD2, and then multiplying by the constant face width. The chord is computed by locating the trailing tip of the driving tooth and computing the arc to the driven tooth. The backlash amount is added in the incompressible and compressible subroutines.

4. SUBROUTINE GEOCAL

This subroutine uses the standard AGMA and USASI tooth systems for spur gears. The computed radii and tooth widths are written to the output listfile.

5. SUBROUTINE DERIVATIVE

This subroutine computes the change in volume with respect to position, $dV/d\theta$. It uses the forward difference method for the derivative at the starting position and the remaining derivatives are computed by the central difference method. It calls the SUBROUTINE VOLUME.

6. SUBROUTINE COMPRESSIBLE

This subroutine computes the pressure, temperature, velocity, and mach number for the three flow areas by assuming compressible flow. It is appropriate for lightly lubricated gears where the primary discharged fluid is air. It uses the Runge-Kutta fourth order formula to solve the change in pressure with respect

to position, $dP/d\theta$. The subroutine calls SUBROUTINE RHS to compute the intermediate values of the function for the Runge-Kutta method. The formula is

$$y_{j+1} = y_j + \Delta t[\frac{1}{6}f(y_j, t_j) + \frac{1}{3}f(y^*_{j+\frac{1}{2}}, t_{j+\frac{1}{2}}) + \frac{1}{3}f(y^{**}_{j+\frac{1}{2}}, t_{j+\frac{1}{2}}) + \frac{1}{6}f(y^*_{j+1}, t_{j+1})]$$

where

$$y^*_{j+\frac{1}{2}} = y_j + \frac{\Delta t}{2}f(y_j, t_j)$$
$$y^{**}_{j+\frac{1}{2}} = y_j + \frac{\Delta t}{2}f(y^*_{j+\frac{1}{2}}, t_{j+\frac{1}{2}})$$
$$y^*_{j+1} = y_j + \Delta t f(y^{**}_{j+\frac{1}{2}}, t_{j+\frac{1}{2}})$$

The intermediate values $y^*_{j+\frac{1}{2}}$, $y^{**}_{j+\frac{1}{2}}$, $and\ y^*_{j+1}$ must be computed in the order given since they are interdependent [15].

7. SUBROUTINE RHS

This subroutine computes the right hand side of the pressure equation for the three flow areas. It calls SUBROUTINES AREA, VOLUME, AND DERIVATIVE.

8. SUBROUTINE INCOMPRESSIBLE

This subroutine computes the velocity for the three flow areas by assuming an incompressible fluid. This case is appropriate for heavily lubricated gears. SUBROUTINES AREA and VOLUME are called.

9. SUBROUTINE BISEC

This subroutine determines the root of an equation that falls within the given limits. It is called by the SUBROUTINE VOLUME to determine the point where the involute portion of the driving gear intersects the addendum circle of the pinion.

10. SUBROUTINE VOLUME

This subroutine computes the volume of space between the driver and the driven teeth. The subroutine is broken up into various integral sets to compute the area of the driving gear that overlaps into the meshing region. This area is used to determine the two-dimensional plane area which is multiplied by the constant face width to give a volume. SUBROUTINES BISEC and SUBTRACT are called.

11. SUBROUTINE APPROX

This subroutine determines the end and beginning points for the cubic fit to the approximation for the area to subtract when the SUBROUTINE SUBTRACT method is no longer valid. The cubic fit used was $f(x) = a_0 + a_1 x + a_2 x^2 + a_3 x^3$.

12. SUBROUTINE SUBTRACT

This subroutine computes the amount of area to be excluded from the 2-D plane area when determining the volume.

13. LISTFILE

The input data is echoed first followed by the computed gear and pinion geometry. The remainder of the output consists of the computed velocities. The first column is the percent mesh position. The incompressible flow columns are designated INC E, INC T, INC C and the compressible flow columns are COMP E, COMP T, COMP C and MACH E, MACH T, MACH C where E corresponds to end flow, T for teeth flow, and C for combined flow.

14. INPUT FILE

The following variables are read free format one per line into the program:

number of gear teeth

pitch of the gear

pressure angle of the gear in degrees

pressure angle of the pinion in degrees

pitch of the pinion

number of pinion teeth

coarse or fine pitch gear (coarse=1,fine=2)

coarse or fine pitch pinion (coarse=1,fine=2)

the maximum iterations in the bisec routine

the convergence criterion for bisection

face width of gear in inches

face width of pinion in inches

convergence criterion for derivative calculations

density of air in lb_m/ft^3

pressure of the ambient lb_f/in^2

dimensional gravitational constant in $lb_m in/lb_f sec^2$

pitch line velocity ft/s

ratio of specific heats

increment of change $\Delta\theta$ in degrees

total number of loops executed

counter for printing results

the number of iterations between write statements

backlash in inches

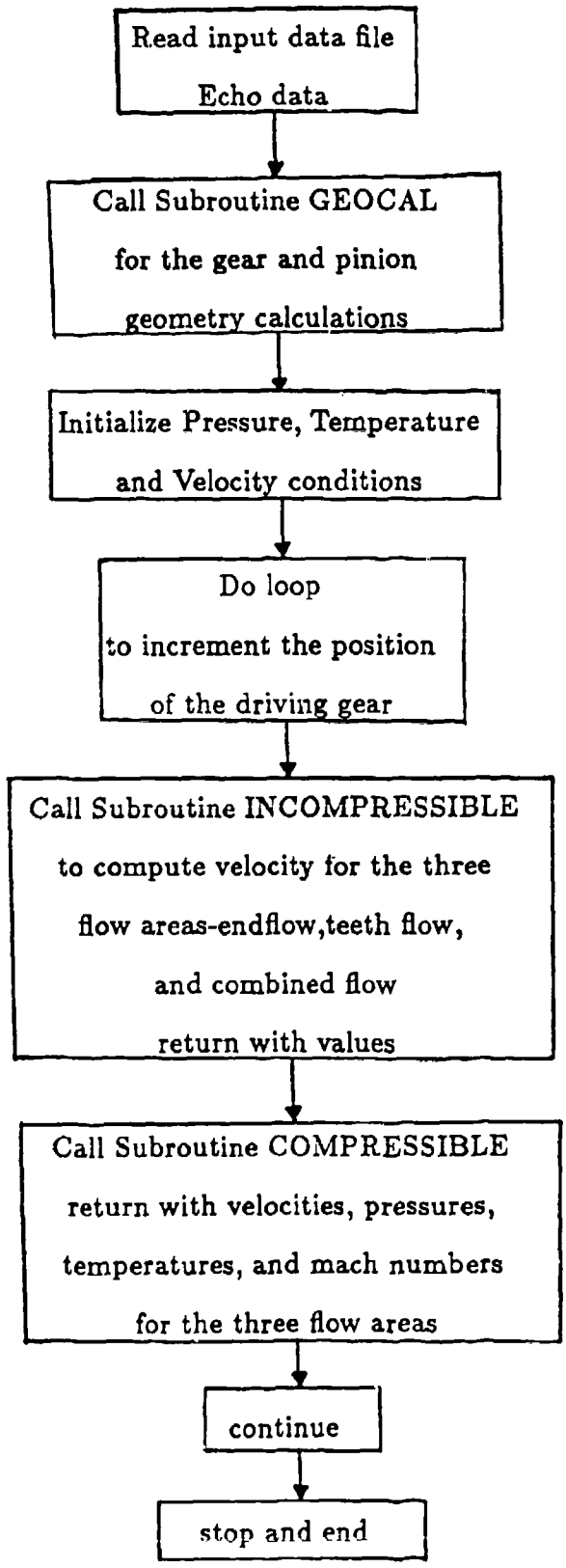
Read input data file
Echo data
Call Subroutine GEOCAL
for the gear and pinion
geometry calculations
Initialize Pressure, Temperature
and Velocity conditions
Do loop
to increment the position
of the driving gear
Call Subroutine INCOMPRESSIBLE
to compute velocity for the three
flow areas-endflow,teeth flow,
and combined flow
return with values
Call Subroutine COMPRESSIBLE
return with velocities, pressures,
temperatures, and mach numbers
for the three flow areas
continue
stop and end

VITA

The author was born on December 13, 1960, in Flint, Michigan. In April 1984, he graduated from The University of Michigan - Ann Arbor with a B.S.E. in Mechanical Engineering. While at The University of Michigan, he was an active member of Lambda Chi Alpha Fraternity holding the offices of Treasurer and Secretary.

During summer breaks from 1980 through 1985, he was employed as a Student Engineer Trainee by divisions of The General Motors Corporation. While at The Pennsylvania State University, he was a Graduate Research Assistant at the Applied Research Laboratory and a Graduate Teaching Assistant with the Department of Engineering Science and Mechanics.

His current interests in mechanics include vibrations, modal analysis, and dynamics. The author is active in sailing (Laser), alpine skiing, running, and weight training.